

Aerosol Jet and Ultra Precise Dispensing Printed Millimeter Wave Interconnects

Zur Erlangung des akademischen Grades eines

**DOKTORS DER INGENIEURWISSENSCHAFTEN
(Dr.-Ing.)**

von der KIT-Fakultät für
Elektrotechnik und Informationstechnik
des Karlsruher Instituts für Technologie (KIT)

angenommene

DISSERTATION

von

M.Sc. Georg Philipp Gramlich

Tag der mündlichen Prüfung:

24.06.2025

Hauptreferent:

Prof. Dr.-Ing. Thomas Zwick

Korreferent:

Prof. Dr. rer. nat. Uli Lemmer

Abstract

Recent years have seen significant advancements in semiconductor technologies operating up to the millimeter wave (mmW) and THz frequency ranges. However, the available bandwidth at these frequencies often remains underutilized due to a lack of suitable packaging technologies. Printed interconnects are a promising solution to this bottleneck, as they can maintain a constant line impedance over the entire interconnect length and hence avoid reflection losses. Additionally, they are well-suited for prototyping, heterointegration, and offer good scalability.

This work presents the development of a manufacturing process for printed mmW interconnects in D-Band (110-170 GHz) and above. First, two topographies—ramp-based and planar—are introduced. Both require distinct manufacturing processes to create the ramp or fill remaining gaps, which are carefully developed and optimized. Subsequently, the required minimum feature size is estimated as a function of the target frequency. With the topographies and minimum feature size determined, two printing processes are selected: Aerosol Jet (AJ) and Ultra Precise Dispensing (UPD) printing. Both offer high printing accuracy, conformal printing capability, and low ink-substrate interaction. Next, both printing processes are analyzed, optimized, and extended.

AJ printing offers simple conformal printing but requires special attention to achieve the required high precision feature sizes down to 10-20 μm . For those structures, we find that a high printing speed can lead to deformations whereas a low printing speed yields a thick layer prone to crack formation. Therefore, we determine the maximum permissible speed depending on the feature size. We choose two sintering methods preventing cracks in thick layers by analyzing the mechanism behind crack formation. Additionally, we greatly improve homogeneity by developing a new shutter on the fly (SOTF) printing routine. These developments expand the limits of the AJ printer providing the required precision and feature size for mmW applications.

The UPD printer intrinsically reaches the required precision but previously suffered from a labor-intensive workflow for conformal printing. To address this issue, a program capable of projecting 2D print paths onto a measured surface is developed. This advancement enables semi-automatic conformal printing, significantly reducing manual labor. It also allows for printing onto more complex surface topographies than before. The importance of alignment for conformal printing is mathematically demonstrated, and methods to enhance line uniformity are introduced. Additionally, the phenomenon of nozzle drift in long-duration print jobs is systematically analyzed.

Leveraging the optimized printing processes we fabricate multiple isolated component demonstrators. These include an AJ printed transmission line, as well as AJ and UPD printed ramp-based interconnects for PCB-to-PCB and PCB-to-MMIC connections. Furthermore, AJ and UPD printed planar interconnects are manufactured using identical assemblies for direct comparability.

Finally, a UPD printed interconnect enables an active beam-steering antenna for 6G communication applications, operating in the 220-325 GHz range. The system integrates a power amplifier based on gallium arsenide (GaAs) technology and an indium phosphide (InP) leaky wave antenna (LWA). It achieves a measured peak gain of 26 dBi, demonstrating a gain enhancement of up to 15 dB compared to the standalone LWA.

This work demonstrates that printed interconnects enable mmW systems with a very large bandwidth and excellent performance. Additionally, printed interconnects facilitate rapid prototyping and heterointegration of multiple semiconductor technologies.

Zusammenfassung

In den letzten Jahren konnte der Millimeterwellen- (mmW) und THz-Frequenzbereich erschlossen werden, was durch erhebliche Fortschritte in der Halbleitertechnologie möglich wurde. Allerdings kann die verfügbare Bandbreite bei diesen Frequenzen mangels geeigneter Aufbautechnik oft nicht ausgeschöpft werden. Gedruckte Verbindungen sind eine vielversprechende Lösung für diesen Engpass, da sie eine konstante Leitungsimpedanz über die gesamte Verbindung aufrechterhalten und somit Reflexionsverluste vermeiden. Außerdem vereinfachen sie Prototypenfertigung und Heterointegration und bieten zusätzlich eine gute Skalierbarkeit.

In dieser Arbeit wird ein Herstellungsprozess für gedruckte mmW-Verbindungen im D-Band (110 - 170 GHz) und darüber entwickelt. Als erstes werden zwei Topografien analysiert - rampenbasiert und planar. Für beide werden die benötigten Prozesse entwickelt und optimiert, um die Rampe zu fertigen bzw. um verbleibende Lücken zwischen MMICs zu füllen. Anschließend wird die erforderliche kleinste Strukturgröße in Abhängigkeit der Betriebsfrequenz geschätzt. Aus diesen beiden Betrachtungen ergeben sich schließlich die Anforderungen an die Drucktechnologie, sodass zwei Druckverfahren ausgewählt werden können. Das sind *Aerosol Jet* (AJ) Druck und *Ultra Precise Dispensing* (UPD) Druck. Beide Technologien bieten eine hohe Genauigkeit, kleine Strukturgrößen, oberflächenfolgendes Druck sowie eine niedrige Tinte-Substrat-Interaktion. Beide Druckverfahren werden charakterisiert und in ihrem Funktionsumfang für Anwendungen in der Hochfrequenztechnik erweitert.

AJ-Druck ermöglicht einfaches oberflächenfolgendes Drucken, erfordert aber Optimierung, um die erforderlichen Strukturgrößen bis 10 μm zu erreichen. Bei derart kleinen Strukturen kann eine hohe Druckgeschwindigkeit zu Verformungen führen, während eine niedrige Geschwindigkeit eine hohe Schichtdicke zur Folge hat, die zur Rissbildung neigt. Daher wird die maximal zulässige Geschwindigkeit in Abhängigkeit von der kleinsten Strukturgröße bestimmt. Zusätzlich wird der Mechanismus, der zur Rissbildung führt, vorgestellt und

basierend darauf zwei Sinterverfahren vorgeschlagen, die Risse vermeiden. Des Weiteren wird die Homogenität des Druckbilds signifikant verbessert, indem eine neue *Shutter on the Fly* (SOTF) Routine programmiert wird. Diese Entwicklungen erweitern den Funktionsumfang des AJ-Druckers und ermöglichen die erforderliche Präzision für mmW-Anwendungen.

Der UPD-Drucker erreicht intrinsisch die erforderliche Präzision, litt aber bisher unter einem arbeitsintensiven Prozess für den oberflächenfolgenden Druck. Um dieses Problem zu lösen, wurde ein Programm entwickelt, das 2D-Druckpfade auf eine gemessene Oberfläche projiziert und daraus 3D-Verfahrensbefehle generiert. Diese Entwicklung ermöglicht halb automatisches oberflächenfolgendes Drucken, was den manuellen Arbeitsaufwand erheblich reduziert. Außerdem lassen sich damit komplexere Oberflächentopografien als bisher bedrucken. Beim oberflächenfolgenden UPD-Druck ist die korrekte Ausrichtung des Substrats von großer Bedeutung, was mathematisch begründet wird. Auch werden Methoden zur Verbesserung der Homogenität gedruckter Linien vorgestellt. Darüber hinaus wird das Phänomen der wandernden Druckdüse bei langen Druckaufträgen systematisch analysiert.

Mit den derart optimierten Druckprozessen werden mehrere Demonstratoren einzelner Komponenten hergestellt. Dazu gehören eine AJ gedruckte Mikrostreifenleitung sowie AJ und UPD gedruckte rampenbasierte Verbindungen für PCB-zu-PCB und PCB-zu-MMIC Verbindungen. Darüber hinaus werden planare AJ und UPD gedruckte Verbindungen mit dem gleichen Aufbau hergestellt, die untereinander vergleichbar sind.

Als finaler Systemdemonstrator wird eine aktive Leckwellenantenne bei 220 bis 325 GHz für die 6G-Kommunikation aufgebaut. Dafür verbindet eine UPD gedruckte Verbindung einen GaAs-Verstärker und eine InP-Leckwellenantenne. Der maximal gemessene Antennengewinn ist 26 dBi, was einer Verbesserung um bis zu 15 dB gegenüber der der Leckwellenantenne alleine entspricht.

Diese Arbeit zeigt, dass gedruckte Verbindungen mmW-Systeme mit einer enormen Bandbreite und ausgezeichneter Performanz ermöglichen. Des Weiteren erleichtern sie die Prototypenfertigung und Heterointegration mehrerer Halbleitertechnologien, was auf lange Sicht zu kürzeren Entwicklungszyklen und reduzierten Kosten führen kann.

Acknowledgments

I would like to express my sincere gratitude to my thesis supervisor, Thomas Zwick, for the trust and freedom he granted me. I deeply appreciate being allowed to structure my work independently, choose my own focus, and receive great advice and scientific feedback whenever needed.

I thank Andreas Gallego, Mirko Nonnenmacher, Jasmin Rösner, and Julian Jochum from the IHE and IPQ workshop team for their excellent and rapid manufacturing of complex submounts, split blocks, and all other designs I created. I am also grateful for the valuable lessons they provided in CAD design for 3D printing.

I thank Andreas Lipp, Thorsten Fux, Steffen Pfeifer, and Lisa Nolte for their support in microelectronic assembly, dicing, and lapping.

I am grateful to Akanksha Bhutani for bringing me into the Open6GHub project, for managing the organizational aspects of my final demonstrator, and for conducting the antenna measurements. I also appreciate her significant contributions to the corresponding publication.

I thank Robert Huber for the collaboration on AJ printing and for all the espressi I enjoyed in his office.

I am deeply grateful to Elizabeth Bekker for her valuable feedback, for always having an open ear, and for the countless professional and personal discussions we had over specialty coffee at Winter.

I thank Luca Valenziano for our joint work on the UPD printer and for proofreading my thesis.

I also extend my thanks to Alexander Quint, Martin Pittermann, Hankun Yang, Luca Valenziano, and Elizabeth Bekker for their feedback on this manuscript.

I sincerely thank the entire IHE team for the great working atmosphere and the many enjoyable moments we shared at seminars, after-work beers, and at private gatherings.

Finally, I want to thank my parents for raising me to be the curious person I am today and for their unwavering and unconditional support. I am also grateful to them for teaching me many of the soft skills that have been invaluable in my work at the IHE and that will continue to benefit me in the future.

Table of Contents

Abstract	i
Zusammenfassung	iii
Acknowledgments	v
Abbreviations and Symbols	xi
1 Introduction	1
1.1 Vision	3
1.2 State of the Art	5
2 Theory	9
2.1 Introduction to Radio Frequency Electronics	9
2.1.1 Maxwell's Equations	9
2.1.2 Plane Waves	12
2.1.3 Transmission Lines	16
2.1.3.1 Ideal Transmission Line	16
2.1.3.2 Lossless Transmission Line	19
2.1.3.3 Terminated Transmission Line	20
2.1.3.4 Quarter Wave Transformer	22
2.1.3.5 Mismatched Transmission Lines	23
2.1.3.6 Realization of Transmission Lines	23
2.1.4 Scattering Parameters	23
2.2 Liquid-Solid Interaction	26
2.2.1 Contact Angle	27
2.2.2 Capillary Action	28
2.3 Utilized Machines	28

2.3.1	Aerosol Jet Printer	29
2.3.2	XTPL Delta Printing System	31
2.3.3	White Light Interferometer	33
3	Concepts and Constraints	35
3.1	Topography	35
3.1.1	Ramp-Based Interconnects	36
3.1.2	Planar Interconnects	37
3.2	Minimum Feature Size	39
4	Improving Printer Accuracy: Modifications and Limitations	43
4.1	Aerosol Jet Printing	43
4.1.1	Printing Speed Influence on Path Accuracy	44
4.1.2	Divert/Boost Shutter and Incremental Deposition Rate	46
4.1.3	Shutter On The Fly - Debugging the Printer	47
4.1.4	Crack Formation and Prevention	50
4.1.5	Summary on AJ Process Considerations and Improve- ments	52
4.2	UPD Printing	54
4.2.1	Semi-Automatic Conformal Printing by Path Projection	55
4.2.2	Conformal Printing Workflow	57
4.2.3	Conformal Printing Execution Time	58
4.2.4	Importance of Alignment for Conformal Printing	60
4.2.5	Semi-Automatic Conformal Printing Demonstrators	63
4.2.6	Nozzle Drift	64
4.2.7	Line Uniformity	69
4.2.8	Summary on UPD Process Considerations and Improve- ments	70
5	Isolated Component Demonstrators	71
5.1	Aerosol Jet Printed Transmission Lines	71
5.1.1	Design	72
5.1.2	Manufacturing	73
5.1.3	Measurement Equipment and Procedures	75
5.1.4	Results and Discussion	76
5.1.5	Summary on Aerosol Jet Printed Transmission Lines	79

5.2	Ramp-Based Interconnects	80
5.2.1	Technology Development	81
5.2.2	AJ Printed Ramp-Based Interconnects	84
5.2.2.1	Design	86
5.2.2.2	Manufacturing	87
5.2.2.3	Results and Discussion	89
5.2.2.4	Summary on Aerosol Jet Printed Ramp-Based Interconnects	93
5.2.3	UPD Printed Ramp-Based Interconnects	94
5.2.3.1	Design	94
5.2.3.2	Manufacturing	96
5.2.3.3	Results and Discussion	97
5.2.3.4	Summary on UPD Printed Ramp-Based Interconnects	101
5.3	Planar Interconnects	103
5.3.1	Technology Development	103
5.3.2	Design	107
5.3.3	Manufacturing	108
5.3.4	AJ Printed Planar Interconnects	109
5.3.4.1	Printing	109
5.3.4.2	Results and Discussion	111
5.3.5	UPD Printed Planar Interconnects	114
5.3.5.1	Printing	114
5.3.5.2	Results and Discussion	116
5.3.6	Summary on AJ and UPD Printed Planar Interconnects	119
6	Demonstrator: Active Leaky Wave Antenna with UPD Printed Interconnect in H-Band	121
6.1	Assembly Overview and System Simulation	122
6.2	Manufacturing	127
6.3	Measurement Results and Analysis	131
6.4	Summary on the Active LWA Demonstrator	137
7	Conclusion	141
A	Appendix	145

A.1 AJ Shutter On The Fly Code 145

References 149

Own Publications 161

 Journal Papers 161

 Conference Papers 162

Abbreviations and Symbols

Abbreviations

AJ	Aerosol Jet
Au	gold
AUT	antenna under test
BCB	benzocyclobutene
CPW	coplanar waveguide
CTE	coefficient of thermal expansion
Cu	copper
CuW	tungsten-copper
DC	direct current
DI	deionized
eWLB	embedded wafer level ball grid array
GaAs	gallium arsenide
GSG	ground-signal-ground
IHE	Institute of Radio Frequency Engineering and Electronics
InP	indium phosphide
ISS	impedance standard substrate

KIT	Karlsruhe Institute of Technology
LCP	liquid crystal polymer
LWA	leaky wave antenna
LRRM	Line-Reflect-Reflect-Match
MS	microstrip
MMIC	monolithic microwave integrated circuit
mmW	millimeter wave
PTFE	polytetrafluoroethylene
PA	power amplifier
PCB	printed circuit board
PI	polyimide
RF	radio frequency
Rx	receiver
SOLT	Short-Open-Line-Thru
SOTF	shutter on the fly
TGME	triethylene glycol monomethyl ether
TRL	Thru-Reflect-Line
Tx	transmitter
UPD	Ultra Precise Dispensing
VNA	vector network analyzer
WLI	white light interferometer

Constants

$c_0 = 299\,792\,458\text{ m/s}$	Speed of light in vacuum
$e = 2.718\,28\dots$	Euler's constant
$\epsilon_0 = 8.854\,18\dots \cdot 10^{-12}\text{ As/Vm}$	Vacuum permittivity
$j = \sqrt{-1}$	Imaginary unit
$\mu_0 = 1.256\,63\dots \cdot 10^{-6}\text{ N/A}^2$	Vacuum permeability
$\pi = 3.131\,59\dots$	Pi

Latin Symbols and Variables

Lowercase Letters

f	Frequency
\vec{j}	Current density
t	Time

Capital Letters

\vec{B}	Magnetic flux density
C'	Shunt capacitance per unit length
\vec{D}	Electric flux density
\vec{E}	Electric field intensity
G'	Shunt conductance per unit length
\vec{H}	Magnetic field intensity
L'	Series inductance per unit length
P	Power
R'	Series resistance per unit length
Y	Admittance
Z	Impedance

Greek Symbols and Variables

α	Attenuation constant
β	Phase constant
γ	Propagation constant
ϵ	Permittivity
λ	Wavelength
μ	Permeability
ρ	Electric charge density
φ	Phase
ω	Angular velocity

Mathematical Operators and Symbols

div	Divergence
rot	Curl
Δ	Laplace operator

1 Introduction

Since the first industrial revolution dating back to the end of the seventeenth century, the world has witnessed increasingly fast technological advances [Buc]. Our modern society became based on technology to a degree that would have been unimaginable only a century ago. A significant part of the vital infrastructure has been equipped with digital sensors and actuators. Communication in private, and in the professional realm is carried out largely through electronic devices. The biggest drivers for economic growth have been technological advances in recent years. It is no coincidence, that eight of the top 10 constituents of the MSCI World index in November 2024 are either tech companies or have a strongly technologically driven background [msc]. We hence do not only profit from the technological advances of the recent decades and centuries, but we also depend on them. They are indispensable for economic growth and thereby societal wealth. One of the current hopes for new developments with a huge impact is industry 4.0. The term has originally been coined by the German Federal Government at the end of 2011 [OT16] [LWW17] and nowadays describes the incipient fourth industrial revolution [BRSP21].

Industry 4.0 requires a dense network of sensors within manufacturing facilities that monitor both internal and external environments [San21]. Those sensors require high accuracy and need to monitor a wide range of variables. Radar is a popular technology for those applications due to its contactless and non-destructive behavior. The demand for increasing precision pushes the operation frequencies far above 100 GHz to achieve the required bandwidth [GGF⁺20]. The same effect can be observed for automotive radar systems, where they play a crucial role in the realization of autonomous vehicles. Safe autonomous systems need to be able to detect other road users reliably and precisely. This requires using a high radar bandwidth, which is only available at high frequencies. In consequence, the operating frequency of automotive radars has experienced a constant increase [WHM21] and will be lifted to 140 GHz in the next generation [CJW⁺13, KHBS13].

Industry 4.0 and autonomous vehicles both require significant communication data rates, which can only be expected to grow in the future. Nevertheless, they only make a small part of the total global data creation, capture, replication, and consumption per year. The International Data Corporation (IDC) refers to this value as the global datasphere and expects a growth to 291 zettabytes (ZB) in 2027 [Ryd23]. A focus on mobile data can be found in the Mobility Report by Ericsson. They predict a growth of the global mobile network traffic to a total of 370 exabyte (EB) per month until the end of 2027 [Eri21]. This anticipated growth can only be satisfied by new technologies, including 5G and 6G, for which frequencies extending into the sub-THz range are currently being explored [INA21, RXK⁺19, MTK⁺20]. The large absolute bandwidth in this frequency range promises ultra-high data rates of up to hundreds of gigabits per second. It is, therefore, seen as a key enabler for applications such as holographic connectivity, device-to-device communication, hotspot downloading, and wireless cellular fronthaul/backhaul networks [IR22]. The importance of the sub-THz frequency range is further punctuated by the establishment of the first IEEE standard for wireless communication in the range from 252 GHz to 325 GHz, IEEE Std. 802.15.3d [PKH20].

The previous elaborations show, that increased operating frequencies for radar and communication systems will be crucial for technological and societal development in the coming years and decades. Fortunately, significant advances in semiconductor technologies have been made in recent years enabling mmW and THz monolithic microwave integrated circuits (MMICs) [MYL⁺15]. One limiting factor for their widespread application is currently the lack of a suitable packaging technology. Those technologies connect an integrated circuit to the surrounding world. Unfortunately, the current options are either performing poorly (e.g. bond wires) or are very expensive (e.g. flip chips) [Son17]. The international research community is hence working deliberately on new packaging technologies. One auspicious candidate is printed interconnects. They are flexible due to their digital nature, promise high performance and will be relatively cheap. Since they promise to relieve a pressing challenge for technological growth in the near future, they have been investigated within this work.

The next section will introduce the vision of printed interconnects and explain why they promise excellent radio frequency (RF) performance, low cost and good prototyping capability. We then proceed to a presentation of the state of

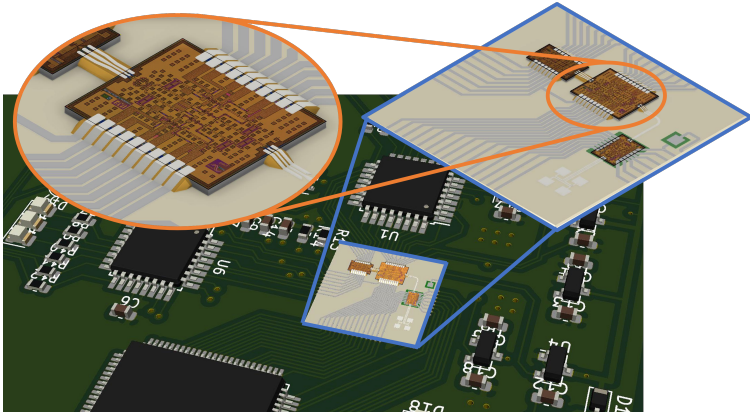


Figure 1.1: Vision of a system with printed RF interconnects: The RF part of the entire system is zoomed in blue and an MMIC featuring is zoomed in orange. The printed interconnects extend the CPW probe-pad configuration via a ramp or bridge to the PCB or the adjacent MMIC. This allows to keep the characteristic impedance constant which yields low losses over an ultra-broadband frequency range.

the art on new packaging approaches in general and detail the current state of the art on printed RF interconnects.

1.1 Vision

The most common way to get RF signals in and out of MMICs is through ground-signal-ground (GSG) probe pads. Those pads are used because they expose the ground and signal conductors on the same layer and, therefore, can be contacted with RF probes for measurements. Once the MMICs have been successfully validated with probe-based measurements, they are embedded into a system. This means that they are connected to a printed circuit board (PCB) or directly to another MMIC. Those connections must match the GSG pattern of the probe pads, which is the case for coplanar waveguide (CPW) transmission lines (see Chapter 2.1.3.6). Therefore, interconnects can be modeled as CPW lines. However, the manufacturing processes do not allow arbitrary shaping of the conductor dimensions, often resulting in an impedance mismatch between MMIC and interconnect. This mismatch must be compensated with a matching

network, which in turn reduces the operational bandwidth of the interconnect. This is why a technology that enables interconnects to maintain the characteristic impedance of the probe pads is needed.

Printed interconnects offer exactly this possibility. The ability to print nearly arbitrary dimensions according system's need allows for a constant transmission line impedance over the entire length, matching the MMIC. Our vision for printed interconnects is shown in Figure 1.1. The manufacturing of the depicted interconnects can be done in the following steps: First, the MMIC is placed on the PCB, and a ramp connecting the top of the MMIC and the PCB is created. Subsequently, the interconnect is printed from the probe pads to the CPW on the PCB. Alternatively, two MMICs can be connected directly. In either way, the dimensions of the printed metal are chosen to maintain the characteristic impedance of the probe pads. This yields high-performance, ultra-broadband interconnects that eliminate the need for matching networks.

Another advantage of printed interconnects is that the printing paths can easily be adjusted to compensate for tolerances in earlier manufacturing steps, such as a misalignment between the PCB and the MMIC. The simplicity of generating printing paths also enables fast prototyping, which reduces development costs and time to market.

The goal of this thesis was to perform an evaluation of the performance of printed interconnects operating above 100 GHz. It should also determine the constraints arising from the RF and the manufacturing side as well as develop the requirement manufacturing processes. Therefore, this thesis begins with an evaluation of the possible topographies for printed interconnects in Chapter 3. This chapter also includes an estimation of the required minimum feature size as a function of the maximum operating frequency. Having these basics established, two printing processes—acAJ and UPD printing—are selected. They are investigated in terms of performance and constraints in Chapter 4. Both printers are also enhanced in their capabilities to address the unique challenges of printed mmW interconnects.

In the subsequent Chapter 5, single-component demonstrators are fabricated using both printing technologies. They include transmission lines and interconnects in two topographies. Finally, the results from these chapters are combined for the creation of a larger system demonstrator in Chapter 6. Here, a

power amplifier and an LWA MMIC operating at 220–325 GHz are combined into an active beam-steering antenna with a UPD printed interconnect.

1.2 State of the Art

As mentioned above, wirebonds typically show a high insertion loss in the sub-THz range as seen in [DRT⁺19], where a single wirebond of length 100 μm connects a 280 GHz to 310 GHz GaAs frequency multiplier MMIC to a quartz stacked patch antenna. The simulated S-parameters of the wirebond interconnect show an insertion loss of 3 to 4 dB. A differential wirebond connects a 246 GHz SiGe BiCMOS BPSK Tx chip to a PCB antenna in [HSEZ24]. The differential wirebond interconnect has an insertion loss of less than 6 dB [HSZ22]. Reducing bond wire interconnect losses requires significant modifications of the standard bonding process as shown in [7]: The distance between the individual bond wires was fine-tuned with a 3D-printed positioner, and adequate dielectric encapsulation and a top metal layer were needed to reduce the losses to 1 dB up to 210 GHz. The other somewhat obvious way of reducing losses is to make bond wire interconnects extremely short which makes manufacturing more complicated due to the reduced tolerance. This approach has been investigated in [PSB⁺24] where losses of 0.6 dB were found up to 135 GHz for bondwires over a substrate gap as small as 30 μm .

A technology that resembles bond wires in shape but requires elaborate manufacturing facilities and exhibits better performance is presented in [ACHW⁺21]. The authors manufactured an air-bridge differential interconnect based on spray coating and laser lithography which connects a 220 GHz to 320 GHz GaAs balun to a quartz-cavity leaky-wave (LW) feed. The differential interconnect has a low loss of 0.2 dB, whereas the assembly loss, including the interconnect, balun, and 730 μm long feed line on quartz, varies between 2.1 dB and 2.7 dB.

Flip Chip is a common interconnect technology for mmW interconnects. In [KUSP14] an interconnect with a loss below 0.9 dB up to 170 GHz is presented, but this approach requires a tuned line topography to compensate for the capacitive effect introduced by the flip-chip overlap section. Therefore, it is unsuitable for off-the-shelf components. When using only 10 μm large micro-bumps, flip-chip interconnects operating up to 250 GHz with 1 dB insertion loss can be made [MSW⁺15]. The authors of [SDS⁺17] were able to increase

the maximum operating frequency with 0.9 dB insertion loss up to 500 GHz by further reducing the bump height to 2 μm , and by carefully designing the transition.

A common problem shared by all flip-chip assemblies is, that the orientation of neighboring chips needs to alternate between face-up and face-down. Face-down orientation can create a thermal bottleneck which makes it inhibitive for most amplifiers and many other active MMICs. This constraint can result in the need for interposer chips which add to the manufacturing cost of the assembly and deteriorate performance. If an MMIC is flip-chip bonded to another MMIC or PCB with a different coefficient of thermal expansion (CTE), changes in temperature cause mechanical stress on the assembly which can lead to bond failure [KC12].

Another popular interconnect technology is embedded wafer level ball grid array (eWLB). It embeds the MMICs in a molding compound and creates a lithographically structured fan-out layer [MOB⁺08]. The authors of [HVV⁺17] used this technology to make a waveguide transition with an average insertion loss of 3.4 dB from 116 - 151 GHz. It can also be used to create antennas directly in the fanout layer [AFS18] or to create chip to chip or chip to PCB connections. A chip to CPW on eWLB transition has exhibited a 0.7 dB insertion loss at 50 GHz [1]. The insertion loss of the eWLB to PCB transition was 0.63 dB at 80 GHz. The authors of [ASH⁺24] created an interconnect between InP and Si MMICs with a process that resembles eWLB. The interconnect is shaped as a 250 μm long CPW redistribution layer with 3 μm high contact vias. The CPW interconnect shows an insertion loss of less than 4 dB at 300 GHz.

Similarly to the flip-chip technology, eWLB suffers from poor thermal dissipation. Since it is a mask-based technology, it additionally comes with a high offset-cost making it unsuitable to prototyping and small batch series.

Furthermore, recent years have seen a significant increase in research on printed RF interconnects. They offer the potential for connecting mmW and sub-THz components by printing a short transmission line interconnect, thus avoiding the inherent parasitic effects of wirebond and flip-chip technologies. Most research on printed interconnects to date is focused on AJ printing due to its ability to achieve feature sizes as small as 10 μm [CCW⁺14b] and its tolerance to minor surface height variations. However, most work focuses on frequencies below 110 GHz or below 170 GHz. Work on printed interconnects in the sub-THz range is scarce.

The suitability of AJ printed silver for mmW applications was demonstrated in [CCW⁺14b] by printing a CPW on a liquid crystal polymer substrate with a measured insertion loss of 0.35 dB/mm at 110 GHz. The same authors additionally printed the substrate material (Polyimide) in [CCW⁺16] and measured a line loss of 0.35 dB/mm at 40 GHz for a stripline. A printed CPW line on a low temperature cofired ceramic substrate exhibited a loss of 0.6 dB/mm at 200 GHz in [IZZB18].

Additionally, AJ printing has been used to manufacture a W-band bandpass filter [CSP⁺18], a wilkinson power divider for 22 - 40 GHz [KHRC⁺], as well as a T-junction and a 3-dB branchline coupler operating at 34 GHz and 42 GHz respectively [PSC⁺19].

Furthermore, some work on AJ printed MMIC interconnects has been published. The one presented in [SDC⁺21] operates up to 16.5 GHz. A fully printed package that has been characterized up to 20 GHz was presented in [CKA⁺20]. In their work, both the metallic interconnects structures, and the substrate material itself have been printed. The work presented in [OAPC19] already doubles the operating frequency: A cavity-based microstrip interconnect is printed and shows a loss of 0.2 dB at 40 GHz. A slotline interconnect was printed and compared to a bond wire interconnect with compensation structures up to 67 GHz in [RJB⁺18]. AJ printing reduced the insertion loss by 0.56 dB at 40 GHz compared to wirebonds. Craton et al. presented a fully printed package including printed bypass capacitors with an average package loss of 1.1 dB from 75 - 92 GHz, including a 3 mm long transmission line, the interconnect, and a GSG launching structure in [CACP21]. Furthermore, in [IZZB19], an AJ printed interconnect between a GaAs MMIC and a low temperature co-fired ceramic package is shown, demonstrating a return loss of more than 10 dB up to 210 GHz and an insertion loss of 2 dB at 140 GHz.

Another printed interconnect approach is based on direct-write multi-photon laser lithography. In [MKH⁺24], a 274 GHz elevated slot antenna is connected to an amplifier MMIC by a printed CPW interconnect. To characterize the interconnect performance, two pieces of transmission lines were connected with a printed interconnect. It shows a deembedded 3 dB bandwidth of up to 290 GHz or above 330 GHz, depending on the transmission line geometry.

UPD printing is a newer alternative to AJ printing [LWW⁺22]. It is a promising printing technique for producing mmW interconnects and other passive RF

components, such as transmission lines [18], inductors [23], and capacitors [22]. It can achieve feature sizes as small as $1\text{ }\mu\text{m}$ [WKF⁺21], which is significantly smaller than the resolution achievable with AJ printing [CCW⁺14b]. In [14], an RF interconnect based on dielectric ramps is printed between a dummy chip and a glass substrate, which exhibits an insertion loss of 0.65 dB at 160 GHz. Unlike AJ printing, UPD is a direct-write technology and therefore requires a precise control of the distance between the printing nozzle and the substrate. This severely complicates printing onto complex topographies, which are often found in printed interconnect applications. Hence, UPD printing requires careful process optimization.

2 Theory

2.1 Introduction to Radio Frequency Electronics

This section gives an introduction to the basics of RF electronics. First, the most common quantities are introduced, as well as Maxwell's equations from which the mathematical description of a plane wave will be derived. This simple type of wave propagation will be used to understand basic properties such as the phase velocity, wavelength, and propagation constant. The theory of transmission lines together with some of their applications and most common physical realization will be introduced in 2.1.3. Lastly, scattering parameters will be presented. Sections 2.1.1 to 2.1.4 can be found in greater detail in [Poz12], [Cha05], and [MG92]. They also borrow from them.

2.1.1 Maxwell's Equations

Before exploring Maxwell's equations, their applications and implications, some common quantities need to be introduced. Those are the

- \vec{E} electric field vector,
- \vec{H} magnetic field vector,
- \vec{D} electric flux density vector,
- \vec{B} magnetic flux density vector,
- \vec{J} electric current density,
- \vec{I} electric current,
- ρ free electric charge density,
- σ electric conductivity,

μ_r	relative magnetic permeability,
ϵ_r	relative permittivity,
$\mu_0 = 1.25663706127 \cdot 10^{-6} \frac{N}{A^2}$	vacuum magnetic permeability,
$\epsilon_0 = 8.8541878188 \cdot 10^{-12} \frac{F}{m}$	vacuum permittivity.

The relation between electric/magnetic fields and flux densities for time- and space invariant, linear, lossless, and isotropic media are defined as

$$\vec{D} = \epsilon \vec{E} = \epsilon_0 \epsilon_r \vec{E} \quad (2.1a)$$

$$\vec{B} = \mu \vec{H} = \mu_0 \mu_r \vec{H}. \quad (2.1b)$$

The relation between the electric field and current is described by

$$\vec{J} = \sigma \vec{E} \quad (2.2)$$

$$I = \iint_S \vec{J} d\vec{s}, \quad (2.3)$$

where I is the current flowing through the surface S .

Having those quantities and relations defined, it is possible to understand Maxwell's equations. They describe the macroscopic interaction of electromagnetic fields. As RF electronics deal with time variant electromagnetic fields, many of the formulas used in higher abstraction levels are based on the equations published by Maxwell in 1865 [Max65] and 1873 [Max73]. Therefore, they will be presented in their basic form within this chapter:

$$\nabla \times \vec{E} = -\frac{\partial \vec{B}}{\partial t} \quad (2.4)$$

$$\nabla \times \vec{H} = \frac{\partial \vec{D}}{\partial t} + \vec{J} \quad (2.5)$$

$$\nabla \cdot \vec{D} = \rho \quad (2.6)$$

$$\nabla \cdot \vec{B} = 0 \quad (2.7)$$

Using Stokes' theorem, equations 2.4 and 2.5 can be written in integral form:

$$\oint_{\partial S} \vec{E} \cdot d\vec{l} = -\frac{\partial}{\partial t} \iint_S \vec{B} \cdot d\vec{s} \quad (2.8)$$

$$\oint_{\partial S} \vec{H} \cdot d\vec{l} = \frac{\partial}{\partial t} \iint_S \vec{D} \cdot d\vec{s} + \iint_S \vec{J} \cdot d\vec{s} = \frac{\partial}{\partial t} \iint_S \vec{D} \cdot d\vec{s} + I, \quad (2.9)$$

where ∂S is a closed contour around the surface S and I is the total electric current flowing through S .

Equations 2.6 and 2.7 can be transformed to the integral form using the divergence theorem, where ∂V describes the closed surface comprising the volume V , and Q is the total free charge comprised in V :

$$\oiint_{\partial V} \vec{D} \cdot d\vec{s} = \iiint_V \rho \, dv = Q \quad (2.10)$$

$$\oiint_{\partial V} \vec{B} \cdot d\vec{s} = 0 \quad (2.11)$$

When dealing with time harmonic signals, it is possible to further simplify Maxwell's equations. In this case, fields can be written as complex vectors with $e^{j\omega t}$ for the harmonic time dependence. The absolute value of the field vector describes the magnitude of the field and the phase φ_0 of the vector equals the phase of the field at $t = 0$. The complete complex notation for an electric field in x -direction is for example

$$E_x(x, y, z, t) = \hat{E}_x \cdot A(x, y, z) \cdot e^{j\varphi_{0x}} \cdot e^{j\omega t} \quad (2.12)$$

$$= E_x(x, y, z) \cdot e^{j\omega t}, \quad (2.13)$$

where \hat{E}_x is the amplitude of the electric field, $A(x, y, z)$ is a complex function describing how the field changes in space, and E_x is the complex electric field in x -direction. For simplicity, $e^{j\omega t}$ is commonly omitted.

The physical fields can be calculated taking the real part of the complex fields such as $\vec{\mathcal{E}} = \text{Re}\{\vec{E} \cdot e^{j\omega t}\}$, meaning for the field in x direction that

$$\mathcal{E}_x(x, y, z) = \text{Re}\{E_x(x, y, z) \cdot e^{j\omega t}\} \quad (2.14)$$

$$= \text{Re}\{\hat{E}_x \cdot A(x, y, z) \cdot e^{j\varphi_{0x}} \cdot e^{j\omega t}\} \quad (2.15)$$

$$= \hat{E}_x \text{Re}\{A(x, y, z)\} \cos(\varphi_{0x} + \omega t). \quad (2.16)$$

In many cases, the time differential of a field needs to be calculated such as in Maxwell's equations 2.4 and 2.5. In the time harmonic case, the time differential can be resolved to

$$\frac{\partial}{\partial t} = j\omega. \quad (2.17)$$

With equation 2.17, Maxwell's equations 2.4 and 2.5 can be simplified for harmonic signals to

$$\nabla \times \vec{E} = -j\omega \vec{B} \quad (2.18)$$

$$\nabla \times \vec{H} = j\omega \vec{D} + \vec{J}. \quad (2.19)$$

2.1.2 Plane Waves

In RF electronics, many problems deal with electromagnetic waves. As the simplest form of such a wave is the plane wave, it will be discussed in this chapter. This allows to introduce concepts such as phase velocity, propagation constant, and wave impedance for a simple example. The gained understanding will be necessary to understand the more complex transmission line types presented in Section 2.1.3. The mathematical deduction of the equations for plane waves can be done using Maxwell's equations as given in 2.4 to 2.7. A source- and current-free, linear, isotropic, homogeneous, and time invariant medium will be assumed, so we can write the equations as:

$$\nabla \times \vec{E} = -\frac{\partial \vec{B}}{\partial t} = -\mu \frac{\partial \vec{H}}{\partial t} \quad (2.20a)$$

$$\nabla \times \vec{H} = \frac{\partial \vec{D}}{\partial t} + \vec{J} = \frac{\partial \vec{D}}{\partial t} = \epsilon \frac{\partial \vec{E}}{\partial t}. \quad (2.20b)$$

Taking the curl of 2.20a and inserting 2.20b into 2.20a gives

$$\nabla \times \nabla \times \vec{E} = \nabla \times \left(-\mu \frac{\partial \vec{H}}{\partial t} \right) \quad (2.21)$$

$$= -\mu \frac{\partial}{\partial t} \nabla \times \vec{H} \quad (2.22)$$

$$= -\mu \epsilon \frac{\partial^2 \vec{E}}{\partial t^2}. \quad (2.23)$$

Using the vector identity $\nabla \times \nabla \times \vec{A} = \nabla(\nabla \cdot \vec{A}) - \Delta \vec{A}$, the above equation can be further simplified into

$$\Delta \vec{E} - \mu \epsilon \frac{\partial^2 \vec{E}}{\partial t^2} = 0, \quad (2.24)$$

because $\nabla(\nabla \cdot \vec{E}) = 0$ as $\nabla \cdot \vec{E} = 0$ in a source-free, homogeneous medium.

Equation 2.24 is called the *wave equation*. In 1886 Heinrich Hertz experimentally proved the existence of electromagnetic waves as described by the wave equation at the Karlsruhe Institute of Technology (KIT). A similar equation for \vec{H} can be derived using the same approach

$$\Delta \vec{H} - \mu \epsilon \frac{\partial^2 \vec{H}}{\partial t^2} = 0. \quad (2.25)$$

For harmonic signals, equations 2.24 and 2.25 can be further simplified using 2.17:

$$\Delta \vec{E} + \omega^2 \mu \epsilon \vec{E} = 0 \quad (2.26)$$

$$\Delta \vec{H} + \omega^2 \mu \epsilon \vec{H} = 0 \quad (2.27)$$

It is of use for the further processing of those equations to introduce a *propagation constant* $k = \omega \sqrt{\mu \epsilon}$. In literature, it also is referred to as *wave number* or *phase constant*.

To solve the differential equations above, a plane wave will be assumed for simplicity. The fields of a plane wave only depend on one coordinate. Within this section, we will assume that the wave propagates in z -direction, and that the electric field only exists in x -direction. Consequently, it is independent on x and y . In this case, equation 2.26 can be simplified to

$$\frac{\partial^2 E_x}{\partial z^2} + \omega^2 \mu \epsilon E_x = \frac{\partial^2 E_x}{\partial z^2} + k^2 E_x = 0 \quad (2.28)$$

as $\partial/\partial x = \partial/\partial y = E_y = E_z = 0$.

This is a differential equation with the solution

$$E_x(z) = E_x^+ e^{-j k z} + E_x^- e^{+j k z} . \quad (2.29)$$

To include the time dependence, the entire equation is multiplied with $e^{j \omega t}$, resulting in

$$E_x(z, t) = E_x^+ e^{j(\omega t - k z)} + E_x^- e^{j(\omega t + k z)} . \quad (2.30)$$

To derive the magnetic field of the wave from the already known electric field, Maxwell's curl equation 2.20a can be used:

$$-j \omega \mu H_y = \frac{\partial E_x}{\partial z} = -j k E_x^+ e^{j(\omega t - k z)} + j k E_x^- e^{j(\omega t + k z)} \quad (2.31)$$

$$H_y = \frac{k}{\omega \mu} \left(E_x^+ e^{j(\omega t - k z)} - E_x^- e^{j(\omega t + k z)} \right) \quad (2.32)$$

$$= \frac{1}{\eta} \left(E_x^+ e^{j(\omega t - k z)} - E_x^- e^{j(\omega t + k z)} \right) \quad (2.33)$$

with $\eta = \omega\mu/k = \sqrt{\mu/\epsilon}$ being the *intrinsic impedance* of the medium. In plane waves it describes the relation between \vec{E} and \vec{H} fields. Since it has the same unit as an impedance, it is also called the *wave impedance*. It is of interest that the \vec{E} and \vec{H} fields are orthogonal to each other and to the direction of propagation. This behavior is called a transverse electromagnetic (TEM) wave.

Besides the propagation constant, the *phase velocity* is a basic property of electromagnetic waves both in free space and in transmission lines. It is defined as the speed with which a point of constant phase is traveling through space. A point of constant phase for the wave traveling in positive z -direction has to satisfy the equation $\omega t - kz = \varphi$ with φ an arbitrary but fix phase. Since the phase is fixed, it needs to be zero when derived by the time so that the phase velocity v_p can be deduced as

$$\frac{\partial (\omega t - kz)}{\partial t} = \frac{\partial \varphi}{\partial t} = 0 \quad (2.34)$$

$$\omega - k \frac{\partial z}{\partial t} = 0 \quad (2.35)$$

$$v_p = \frac{\partial z}{\partial t} = \frac{\omega}{k}. \quad (2.36)$$

For a wave propagating in empty space,

$$v_p = \frac{\omega}{k} = \frac{\omega}{\omega\sqrt{\mu_0\epsilon_0}} = \frac{1}{\sqrt{\mu_0\epsilon_0}} = 2.988 \times 10^8 \text{ m/s} = c_0 \quad (2.37)$$

where c_0 is the speed of light in vacuum.

The distance between two consecutive points of the same phase in the propagation direction of the wave is called *wavelength*. It can be calculated as follows:

$$(\omega t - kz) - (\omega t - k(z + \lambda)) = 2\pi \quad (2.38)$$

$$\lambda = \frac{2\pi}{k} = \frac{2\pi v_p}{2\pi f} = \frac{v_p}{f} \quad (2.39)$$

In a lossy medium, k is replaced by the *complex propagation constant*

$$\gamma = j\omega\sqrt{\mu\epsilon} = j\omega\sqrt{\mu\epsilon'(1 - j\tan\delta_e)}, \quad (2.40)$$

where α is the *attenuation constant*, β as the *phase constant*, and $\underline{\epsilon}$ is the complex permittivity. The complex permittivity is used to describe losses in the medium and defined as $\underline{\epsilon} = \epsilon' - j\epsilon''$. The imaginary part accounts for losses caused by damping of vibrating dipole moments. Losses due to Ohm's law are indistinguishable from dielectric ones. Therefore, it is possible to include the total losses in the complex permittivity as $\underline{\epsilon} = \epsilon'(1 - j\tan\delta_e)$ with

$$\tan(\delta_e) = \frac{\omega\epsilon'' + \sigma}{\omega\epsilon'}. \quad (2.41)$$

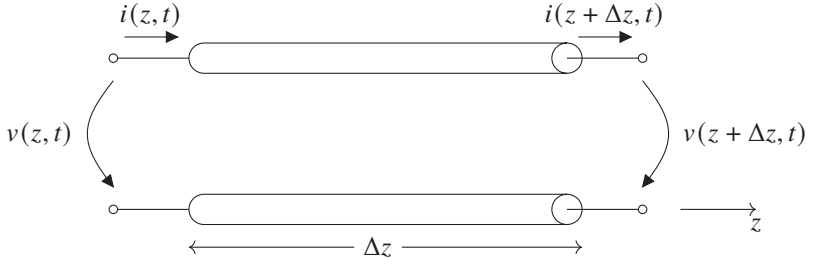
A more detailed description with deductions of the formulas for plane waves in lossy media is presented in [Poz12] in chapters 1.3 and 1.4.

2.1.3 Transmission Lines

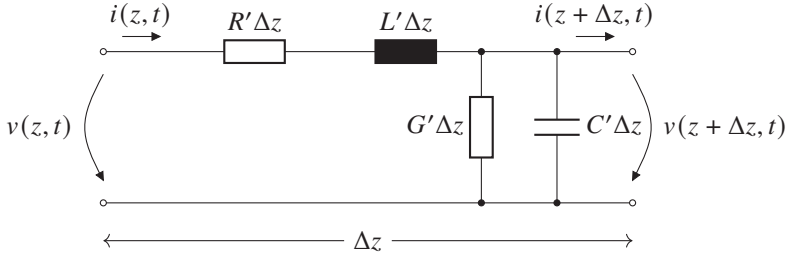
In low frequency electronics, calculations are usually not done using electric and magnetic fields or waves but using lumped components. This approach is valid because the lengths of the conductors are small in comparison to the wavelength. In RF electronics, however, more complex approximations are necessary in order to consider the substantially smaller wavelengths. Because of those, the current and voltage amplitude and phase are not constant over the length of a conductor. On the contrary, it is possible that the conductor length is a considerable part of the wavelength to multiple wavelengths. Nonetheless, it is desirable to use circuit theory to analyze circuits instead of waves. This is made possible by transmission line theory.

2.1.3.1 Ideal Transmission Line

As mentioned above, the challenge in RF electronics is that voltage and current vary over the length of a transmission line which makes it impossible to apply standard circuit analysis. But making a hypothetical transmission line segment infinitesimally small results in a quasi constant voltage and current over the segment. An infinitesimally small transmission line section can hence be analyzed with standard circuit theory. This approach is applied to the transmission line shown in Figure 2.1. The lumped components used to describe the transmission line segment in 2.1b have the following meaning:



(a) Voltage and current definitions for a transmission line.



(b) Lumped element equivalent circuit for a transmission line.

Figure 2.1: Definitions relevant for transmission line theory.

R' series resistance per unit length, in Ω/m

L' series inductance per unit length, in H/m

G' shunt conductance per unit length, in S/m

C' shunt capacitance per unit length, in F/m

Using Kirchhoff's equations for voltages and currents yields

$$v(z, t) - v(z + \Delta z, t) - R' \Delta z i(z, t) - L' \Delta z \frac{\partial i(z, t)}{\partial t} = 0 \quad (2.42)$$

$$i(z, t) - i(z + \Delta z, t) - G' \Delta z v(z + \Delta z, t) - C' \Delta z \frac{\partial v(z + \Delta z, t)}{\partial t} = 0. \quad (2.43)$$

Equations 2.42 and 2.43 can be divided by Δz . For the limit $\Delta z \rightarrow 0$ they become

$$\frac{\partial v(z, t)}{\partial z} = -R' i(z, t) - L' \frac{\partial i(z, t)}{\partial t} \quad (2.44)$$

$$\frac{\partial i(z, t)}{\partial z} = -G' v(z, t) - C' \frac{\partial v(z, t)}{\partial t}. \quad (2.45)$$

These are the *telegrapher equations* that describe the transmission line in the time domain. For harmonic sinusoidal voltages and currents, they can be simplified to

$$\frac{dV(z)}{dz} = -(R' + j\omega L')I(z) \quad (2.46)$$

$$\frac{dI(z)}{dz} = -(G' + j\omega C')V(z). \quad (2.47)$$

Differentiating equations 2.46 and 2.47 with respect to z and inserting them into each other yields

$$\frac{d^2 V(z)}{dz^2} - (j\omega L' + R')(j\omega C' + G')V(z) = 0 \quad (2.48)$$

$$\frac{d^2 I(z)}{dz^2} - (j\omega L' + R')(j\omega C' + G')I(z) = 0. \quad (2.49)$$

It is helpful to define

$$\gamma = \alpha + j\beta = \sqrt{(j\omega L' + R')(j\omega C' + G')} \quad (2.50)$$

as the complex propagation constant. With this simplification, the solutions for the differential equations 2.48 and 2.49 are

$$V(z) = V_0^+ e^{-\gamma z} + V_0^- e^{\gamma z} \quad (2.51)$$

$$I(z) = I_0^+ e^{-\gamma z} + I_0^- e^{\gamma z}. \quad (2.52)$$

Note the similarity to the propagation of a plane wave in equation 2.29. With the same reasoning as for plane waves, it follows that $e^{-\gamma z}$ represents a wave traveling in positive z -direction and that $e^{\gamma z}$ describes one traveling in the opposite direction.

To calculate the current for a known voltage, one can insert equation 2.51 into 2.46:

$$I(z) = \frac{\gamma}{j\omega L' + R'} (V_0^+ e^{-\gamma z} - V_0^- e^{\gamma z}). \quad (2.53)$$

Knowing both the voltage and the current on the transmission line, their ratio can be calculated. It is referred to by Z_0 and denominated the *characteristic impedance*. Its definition is

$$Z_0 = \frac{V_0^+}{I_0^+} = -\frac{V_0^-}{I_0^-}. \quad (2.54)$$

The characteristic impedance of a transmission line can be calculated as

$$Z_0 = \sqrt{\frac{j\omega L' + R'}{j\omega C' + G'}}. \quad (2.55)$$

2.1.3.2 Lossless Transmission Line

Calculating with lossy transmission lines is generally more complex than assuming the lossless case. Therefore, it is often of interest to start analyses by observing the lossless case and potentially incorporate losses in a later stage. Especially for good conductors with a low surface roughness and for dielectrics with low losses, the lossless case is close enough to reality for many applications.

The losses in a transmission line are introduced by the finite conductivity of the conductors and by the dielectric losses in a medium. Mathematically, they are represented by R' and G' respectively. In a lossless transmission line, both of them vanish. Consequently, equations 2.50 and 2.54 simplify to

$$\gamma = j\omega\sqrt{L'C'} \quad (2.56)$$

$$Z_0 = \sqrt{\frac{L'}{C'}} \quad (2.57)$$

It can be seen that the propagation constant is completely imaginary for a lossless transmission line or that $\alpha = 0$. Additionally, Z_0 becomes a real number for a

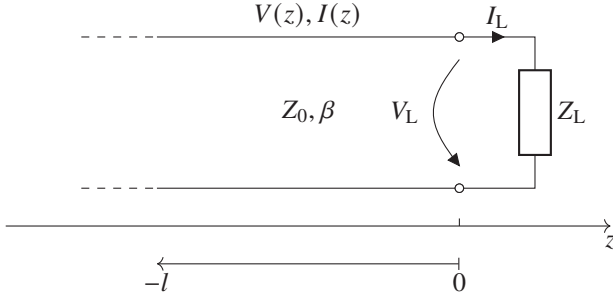


Figure 2.2: Terminated transmission line.

lossless transmission line. Voltage and current on the line can then be written as

$$V(z) = V_0^+ e^{-j\beta z} + V_0^- e^{j\beta z} \quad (2.58)$$

$$I(z) = \frac{V_0^+}{Z_0} e^{-j\beta z} - \frac{V_0^-}{Z_0} e^{j\beta z}. \quad (2.59)$$

2.1.3.3 Terminated Transmission Line

Equations 2.54 and 2.57 describe how voltages and currents depend on each other on a transmission line. For a terminated line as shown in Figure 2.2, another constraint exists. At $z = 0$, where the load impedance is connected, Ohm's law requires that

$$Z_L = \frac{V(0)}{I(0)} = \frac{V_0^+ + V_0^-}{I_0^+ - I_0^-}. \quad (2.60)$$

In many cases it is only possible to satisfy this equation when $I_0^- \neq 0$, meaning that a part of the energy transported to the load is reflected. The ratio of the incident and reflected part of a wave is described by the *reflection coefficient*

$$\Gamma = \frac{V_0^-}{V_0^+} = -\frac{I_0^-}{I_0^+}. \quad (2.61)$$

With the use of 2.61, equation 2.60 can be written as

$$Z_L = \frac{(1 + \Gamma)V_0^+}{(1 - \Gamma)I_0^+} = \frac{1 + \Gamma}{1 - \Gamma} Z_0. \quad (2.62)$$

Solving for Γ yields

$$\Gamma = \frac{Z_L - Z_0}{Z_L + Z_0}. \quad (2.63)$$

When $Z_L \neq Z_0$, the reflection coefficient will be different from zero. This is called a mismatch and a part of the energy will be reflected at the load. Therefore, a standing wave forms on the line and the voltage and current amplitude distribution is not constant. Consequently, the impedance seen at the input of the transmission line also varies with the length l of the line. At the point $-l$, as seen in Figure 2.2, the input impedance can be calculated as

$$Z_{in} = \frac{V(-l)}{I(-l)} = \frac{V_0^+ (e^{j\beta l} + \Gamma e^{-j\beta l})}{V_0^+ (e^{j\beta l} - \Gamma e^{-j\beta l})} Z_0 = \frac{1 + \Gamma e^{-2j\beta l}}{1 - \Gamma e^{-2j\beta l}}. \quad (2.64)$$

A form that is often easier to use can be found by inserting 2.63 for Γ .

$$Z_{in} = Z_0 \frac{(Z_L + Z_0) e^{j\beta l} + (Z_L - Z_0) e^{-j\beta l}}{(Z_L + Z_0) e^{j\beta l} - (Z_L - Z_0) e^{-j\beta l}} = Z_0 \frac{Z_L + j Z_0 \tan(\beta l)}{Z_0 + j Z_L \tan(\beta l)} \quad (2.65)$$

Special cases arise for an open or shorted transmission line. For the first one $Z_L \rightarrow \infty$ and 2.65 simplifies to

$$Z_{in} = -j Z_0 \cot \beta l. \quad (2.66)$$

For the latter case of a shorted transmission line, the input resistance can be given as

$$Z_{in} = j Z_0 \tan \beta l. \quad (2.67)$$

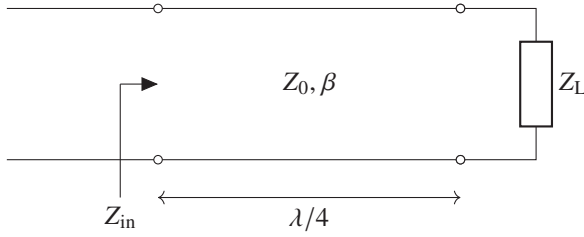


Figure 2.3: Quarter wave transformer

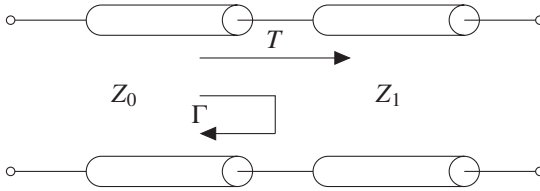


Figure 2.4: Reflection and transmission between two mismatched transmission lines

2.1.3.4 Quarter Wave Transformer

An especially interesting case of a terminated transmission line arises for a length of $\lambda/4$, because it can be used as an impedance transformer. Such a circuit is shown in Figure 2.3.

The input impedance of a quarter wave transformer can be calculated using equation 2.65 as

$$Z_{in} = Z_0 \frac{Z_L + j Z_0 \tan(\beta \cdot \lambda/4)}{Z_0 + j Z_L \tan(\beta \cdot \lambda/4)} = Z_0 \frac{Z_L + j Z_0 \tan(\pi/2)}{Z_0 + j Z_L \tan(\pi/2)} = \frac{Z_0^2}{Z_L}. \quad (2.68)$$

A quarterwave transformer is commonly used to achieve impedance matching. On the downside, equation 2.68 is only valid if the line length is close to $\lambda/4$. Id est, the matching only works for a limited frequency range and is hence not suitable for broadband circuits.

2.1.3.5 Mismatched Transmission Lines

When two transmission lines with different line impedances are connected, a part of the incident wave is reflected and a part is transmitted. This is typically the case for RF interconnects where the transmission line type additionally changes, and it is near impossible to keep the characteristic impedance perfectly constant. The case of two mismatched transmission lines is shown in Figure 2.4. The reflection coefficient Γ and the transmission coefficient T can be calculated as

$$\Gamma = \frac{Z_1 - Z_0}{Z_1 + Z_0} \quad (2.69)$$

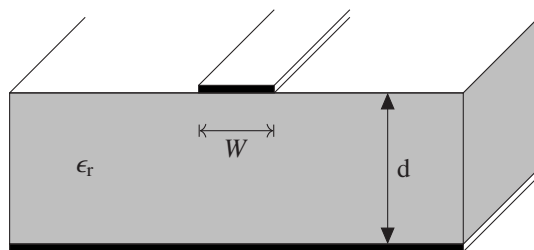
$$T = \frac{2Z_1}{Z_1 + Z_0}. \quad (2.70)$$

2.1.3.6 Realization of Transmission Lines

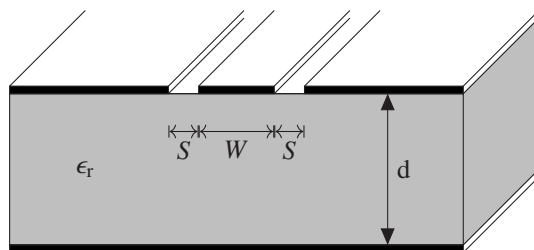
Transmission lines can have various forms and field distributions. Which line type to choose depends on the problem at hand. A microstrip line is easy to realize in a standard PCB production process and therefore cheap. It cannot transport high power though. For high power and low-loss applications, a waveguide is the better choice. CPW lines are commonly found on PCBs and MMICs since their field configuration matches the field configuration of most RF measurement probes. However, CPW lines are prone to higher order modes and show higher losses, so many applications will require a transition to a different kind of transmission line. Figure 2.5 shows the physical appearance of the transmission line types mentioned above with their most important design parameters. More details can be found in [GGB79] and [Poz12].

2.1.4 Scattering Parameters

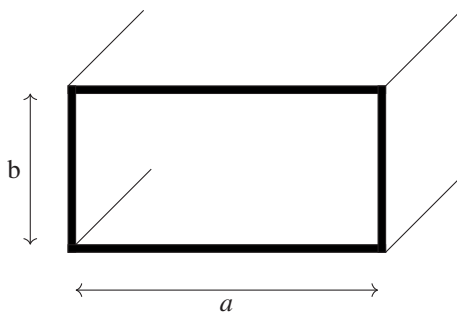
Electromagnetic fields, as well as currents and voltages are a somewhat bulky and often complicated way to describe the behavior of mmW circuits. This is why microwave networks are most often described using *scattering parameters*. They define the ratio of the incident and reflected power at a port as well as the ratio of the incident power and the power transmitted to another port. Since



(a) Microstrip line.



(b) Grounded coplanar waveguide.



(c) Rectangular waveguide.

Figure 2.5: Common transmission line types.

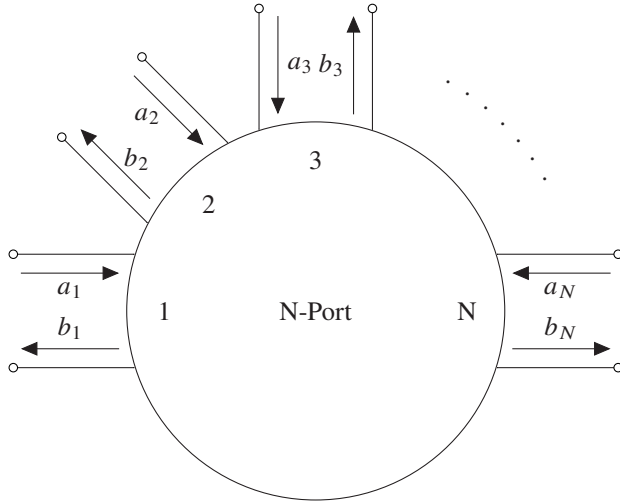


Figure 2.6: N-Port with incoming and reflected power waves.

most microwave circuits have more than one port, S-parameters are usually given in the form of a matrix. An arbitrary N-Port is shown in Figure 2.6. At each port, one so-called power wave enters the port ($a_1 - a_N$) and one power wave exits the port ($b_1 - b_N$). The entering and exiting power waves are related through the S-parameter matrix:

$$\begin{bmatrix} b_1 \\ b_2 \\ b_3 \\ \vdots \\ b_N \end{bmatrix} = \begin{bmatrix} s_{11} & s_{12} & s_{13} & \cdot & \cdot & \cdot & s_{1N} \\ s_{21} & s_{22} & s_{23} & \cdot & \cdot & \cdot & s_{2N} \\ s_{31} & s_{32} & s_{33} & \cdot & \cdot & \cdot & s_{3N} \\ \cdot & \cdot & \cdot & \cdot & \cdot & \cdot & \cdot \\ \cdot & \cdot & \cdot & \cdot & \cdot & \cdot & \cdot \\ s_{N1} & s_{N2} & s_{N3} & \cdot & \cdot & \cdot & s_{NN} \end{bmatrix} \cdot \begin{bmatrix} a_1 \\ a_2 \\ a_3 \\ \vdots \\ a_N \end{bmatrix} \quad (2.71)$$

The unit of the power waves is \sqrt{W} . This means that they behave more like voltages and currents than like powers - despite their name. It also means that the correct conversion factor for S-parameters to decibel is 20:

$$S_{\text{dB}} = 20 \log_{10} (S_{\text{lin}}) \quad (2.72)$$

The diagonal elements of a S-parameter matrix, s_{11}, s_{22} to s_{NN} , describe the input reflection at the corresponding ports, while a parameter s_{ij} describes the path from port j to port i .

A microwave network is called reciprocal if the describing S-parameter matrix fulfills the condition

$$[S] = [S]^t. \quad (2.73)$$

If a microwave network is lossless, its S-parameter matrix fulfills the condition

$$[S]^t [S]^* = [U], \quad (2.74)$$

where $[U]$ is the unitary matrix. This is equal to demanding that the sum of the squared absolute values of each element of a row shall be one:

$$\sum_{k=1}^N |s_{ik}|^2 = 1, \quad \forall i \in \mathbb{N}, 1 \leq i \leq N, \quad (2.75)$$

where i is an arbitrary row of the matrix.

2.2 Liquid-Solid Interaction

Beside the discussion of electromagnetic basics in the chapter above, it is also important to introduce some material science basics for this work. The behavior of printed materials is fundamentally influenced by surface interactions. Similarly, the filling of small gaps depends on capillary action, as will be discussed later. Therefore, the physical concepts of contact angle and capillary action will be introduced in this section.

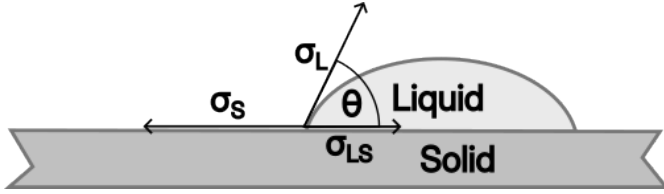


Figure 2.7: Contact angle between a solid and a liquid.

2.2.1 Contact Angle

When a droplet of a liquid is dispensed onto a solid, it will spread or contract until it reaches an equilibrium. In this state, the angle formed between solid and liquid where they meet is called contact angle. It depends on the medium above the surface and the liquid as well as the nature of the liquid and solid in contact. It changes with the surface tension of the liquid and hence with its temperature and purity. The Young equation describes the contact angle as

$$\cos \Theta = \frac{\sigma_S - \sigma_{LS}}{\sigma_L}, \quad (2.76)$$

where Θ is the contact angle, σ_S is the surface energy of the solid, σ_{LS} is the solid-liquid interfacial energy, and σ_L is the surface tension of the liquid [van08]. Fig. 2.7 depicts the relation of those quantities. For a contact angle between 0 and 90°, the liquid tends to spread over the solid, which is typically referred to as good wettability. Low wettability is attested for a contact angle between 90° and 180°. In this regime, the term dewetting is also commonly used to describe a liquid contracting into a near-spherical shape which exhibits poor adhesion to the substrate. In the case of water as liquid, this regime is called hydrophobic. It can e.g. be observed on water-repellent cloth or Teflon frying pans. When it comes to printing, poor wettability is a problem since it reduces the adhesion of the printed ink to the substrate. However, wettability can be improved by increasing the surface energy and hence decreasing the contact angle. A common way to achieve this is oxygen plasma treatment before printing: During oxygen plasma treatment of a nonpolar material such as polytetrafluoroethylene (PTFE), hydrogen atoms in the surface of the material are replaced by oxygen atoms. They have free valence electrons allowing the ink to bond to the surface and additionally increase the polarity of the substrate.

An additional advantage of oxygen plasma treatment is that organic residues on the surface are broken up into smaller, volatile compounds, thereby cleaning the surface.

2.2.2 Capillary Action

Capillary action describes the propagation of a liquid in a narrow space without the application of an external force. This is most commonly observed in a thin tube such as a straw. For a vertical tube, the resulting height of a liquid column can be calculated according to Jurin's law [Bat00]:

$$h = \frac{2\sigma_L \cos \Theta}{\rho g r}, \quad (2.77)$$

where h is the height of the column, ρ is the density of the liquid, g is the local acceleration due to gravity, and r is the radius of the tube. According to the previous section, σ_L is the surface tension of the liquid and Θ is the contact angle. From the term $\cos \Theta$ above the fraction follows, that the column height increases for a low contact angle which means for good wetting behavior between liquid and solid. This is to be expected since a low contact angle typically means that the liquid spreads wider over the solid. In consequence, oxygen plasma treatment would increase the height of the column due to the decreased contact angle.

2.3 Utilized Machines

An important part of the work done for this dissertation was the optimization of printing processes to render them suitable for RF applications. Therefore, the two printers investigated will be presented within this section. Additionally, surface measurement techniques played a crucial role in the process optimization, which is why the operating principle of a white light interferometer (WLI) will be presented as well.

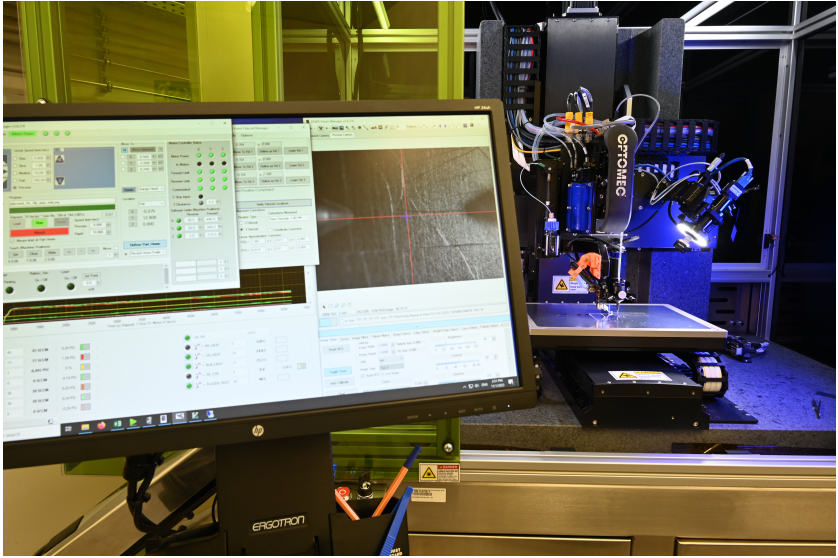


Figure 2.8: Photo of the Aerosol Jet printer used in this work including the control screen.

2.3.1 Aerosol Jet Printer

Aerosol Jet printing is a contactless additive manufacturing technique, that allows printing structures down to $10\text{ }\mu\text{m}$ minimum feature size [CCW⁺14b]. The raw material needs to be presented as an ink with a viscosity between 1 and 1000 cp. This ink is atomized into an aerosol, which is picked up by a nitrogen gas stream and subsequently filtered to achieve a homogeneous droplet size of approximately $5\text{ }\mu\text{m}$. To avoid drying the ink in the reservoir, the nitrogen stream is led through a bubbler before coming in contact with the ink, allowing it to be already saturated with the ink's solvents. The filtered aerosol is transported to the printing nozzle. This gas stream is called the atomizer flow. In the nozzle, a sheath gas stream is separately supplied and wrapped around the atomizer flow. This results in a focusing effect and shields the nozzle from the droplets at the same time, thus preventing nozzle clogging. This gas stream is called the sheath flow. The dimension of the nozzle, as well as the ratio of the atomizer to sheath flow rate primarily influence the printed line width. Figure 2.9a gives an overview of the working principle and of the most important gas streams.

Interrupting the deposition of ink droplets onto the substrate is done using a shutter. The AJ5X printer by Optomec as seen in Figure 2.8, which has been used in this work has two different shutter mechanisms. The first option is to interrupt the gas stream exiting the nozzle with a mechanical shutter, see Figure 2.9b. This mechanism consists of a spoon that is moved between nozzle and substrate and thereby interrupts the ink deposition. It has an extremely fast response time of approximately 5 ms but comes with the disadvantage that the spoon can fill up and cause ink splashes. The second shutter mechanism, depicted in Figure 2.9c, is called the divert/boost shutter. The idea behind it is to suck the aerosol out of the printing nozzle and replace it with dry nitrogen. The latter is necessary to keep the nozzle pressure constant and avoid turbulences. The atomizer stream is led out of the nozzle into a filter and a new stream called boost replaces it in the nozzle. To prevent any leakage from the original atomizer stream out of the nozzle, a part of the newly introduced boost flow is moving upwards through the nozzle and leaves it together with the atomizer flow. This creates a material movement in the opposite direction of the atomizer flow and effectively prevents any leakage. The obvious advantage of the divert/boost shutter is that there is no spoon that could fill up and cause splashes. Additionally, this mechanism does not require mechanical parts between nozzle and substrate allowing a lower nozzle-to-substrate distance, which typically reduces overspray. On the downside, the response time is significantly slower, around 100 ms.

The explanation above borrows from [5]. A detailed explanation of the working principle of AJ printers is given in [WSKH19], and Secor describes in [Sec18] how the atomizer and sheath gas streams influence the line geometry based on fluid dynamics. A thorough investigation of overspray is presented in [FRR21]. Mahajan et al. [MFF13] published an excellent experimental investigation on the influence of the ratio of atomizer to sheath flow, and of the printing speed. The findings presented in those references have been applied in the work presented here but are not necessary to understand it. They will therefore not be discussed in the following.

The great advantages of AJ printing are the fast printing speed, the versatility in terms of printed materials, and the ability to print onto complex surfaces. Since the standoff distance between nozzle and substrate is 2 - 5 mm, minor variations in substrate height do not influence the print. If more complex surfaces need to be printed on, it is even possible to equip the printer with two additional rotational axes for conformal printing.

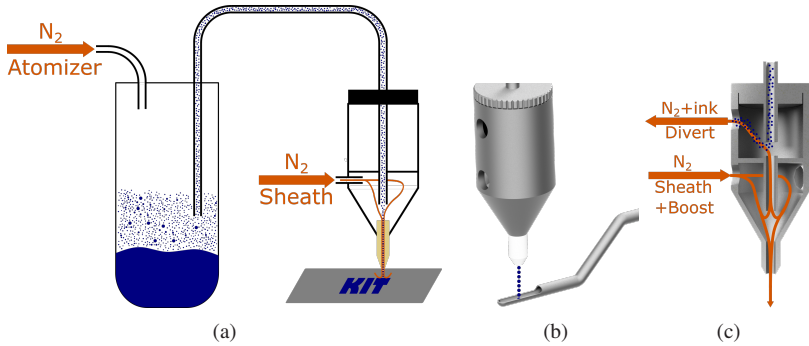


Figure 2.9: (a) Working principle of an AJ printer. (b) The ink deposition can be interrupted with a mechanical shutter. (c) Alternatively, the ink deposition can be interrupted by using the divert and boost gas streams. The boost stream ensures that the pressure in the nozzle stays constant while the divert stream leads the aerosol out of the nozzle into a filter. Figure reprinted from [5].

2.3.2 XTPL Delta Printing System

XTPL coined the term Ultra Precise Dispensing (UPD) referring to the technology utilized in their Delta printing system. The terms UPD printer, and Delta printer can be used interchangeably. They all refer to the same highly precise direct write printing system. It utilizes highly viscous inks extruded at a pressure up to 10 bar through a glass nozzle with an opening diameter between $1.5\ \mu\text{m}$ and $20\ \mu\text{m}$, while nozzle sizes up to $5\ \mu\text{m}$ are the most common. The system is connected via a passive pressure amplifier to a typical compressed air or nitrogen supply line. Amplification of the pressure is necessary to achieve the required specifications of the Delta Printing System. It triples the supply line pressure into a buffering tank followed by a pressure controller setting the input pressure to the actual printing system to 10 bar. The next element in the system chain is an electronic pressure controller. It is connected to the control computer and sets the pressure applied to the ink during every step of the printing process. Finally, the fine-tuned pressure reaches the ink reservoir (silver in Figures 2.10 and 2.11) which is directly connected to the printing nozzle. The ink reservoir is clipped to a holder which is connected to precise x-, y-, and z-axes.

The most commonly used ink on this printing system is the silver nanoparticle ink CL85 by XTPL. It contains an unusually high solid content (82 wt. %) and

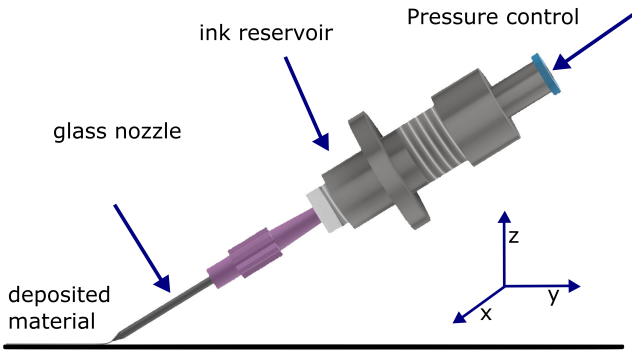


Figure 2.10: Schematic drawing of the UPD printing nozzle. The coordinate system defines the axes according to the motion system of the printer. Reprinted from [6].

therefore exhibits thixotropic behavior. This means that it has a lower viscosity when extruded through the narrow nozzle opening due to the applied shear force. Once extruded and in standstill, the viscosity is high again (> 100.000 cP). The thixotropic behavior allows creating higher aspect ratios than possible with less viscous inks in one pass.

The system is connected to a control computer which runs a terminal-like environment in which custom scripts in a proprietary programming language can be executed. This language supports variables, control loops, and subroutines. It also provides access to all relevant physical actions of the machine including the applied pressure and axis movement. A special atomic command 'veclineramp' combines pressure and motion control. It describes a linear movement with specified acceleration and deceleration distances together with the printing velocity and pressure. In this way, the slow rise and fall of the applied pressure in the beginning and end of each line segment can be compensated by the acceleration and deceleration distances. This allows for more homogeneous lines as further elaborated in section 4.2.7.

The nozzle and the substrate need to be constantly in very close proximity ($\leq 1\mu\text{m}$) or in touch during the printing process. Exceeding this distance causes interrupted lines. Since the nozzle is made of very thin glass, it is slightly flexible

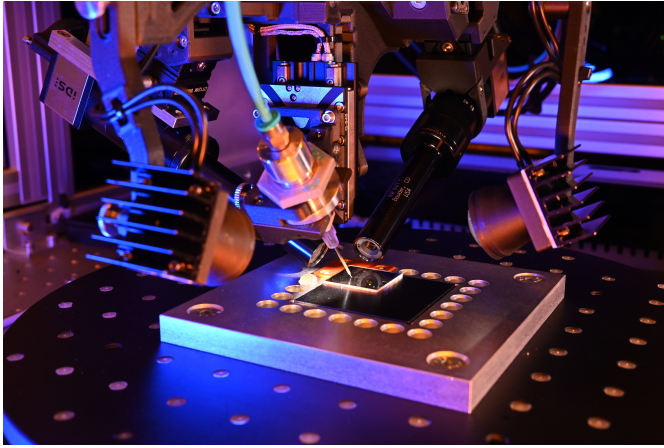


Figure 2.11: Photo of the Delta printing system utilized in this work.

and can be bent several micrometers. This means that it is possible to move the nozzle down by roughly $10\text{ }\mu\text{m}$ below the point of contact without breaking it. This intrinsic flexibility of the system allows compensating for minor variations in substrate height. Nonetheless, excessively bending the nozzle decreases the accuracy of the printed structures and increases the risk of breakage. Therefore, it is good practice to keep the initial overtravel below $3\text{ }\mu\text{m}$. This means that variations of $\pm 3\text{ }\mu\text{m}$ in substrate height can be compensated by the nozzle. Variations above this value need to be included in the programmed movements. The capability of the nozzle to compensate for substrate height variation through its intrinsic flexibility will be called “nozzle slack” in this work.

2.3.3 White Light Interferometer

White light interferometry is a non-contact method for large-area surface measurements. It is based on a Michelson interferometer in which a beam of light is split into two beams by a semi-transparent mirror. One beam is directed onto a reference mirror and the other one onto the sample surface. When the reflections of both beams are superimposed, interference occurs. However, the prerequisite is that the path lengths are approximately equal and the difference

in length is less than half of the coherence length [BWC13]. The maximum constructive interference is achieved when the two path lengths are exactly the same.

The use of white light is an important feature of this method. Due to the wide spectrum of white light, interference only occurs for nearly equal path lengths and a confusion of the order is not possible. Additionally, small changes in surface height strongly impact the interference enabling measurements of small changes.

In the Bruker Contour GT-X utilized in this work, the surface to measure is moved with respect to the lens and the interference is recorded with a camera sensor at each position. Subsequently, the height at each pixel can be computed. A surface larger than the field of view can be measured in a stitching process enabled by the automated x- and y-axes of the sample holder.

3 Concepts and Constraints

Before developing RF interconnects or optimizing printing technologies, it is essential to identify the requirements and constraints of the systems to be developed. This chapter investigates potential topographies for additively manufactured RF interconnects, analyzing their advantages and limitations. Actual system designs to be manufactured and measured, necessitate a co-design approach that combines manufacturing processes and system-level requirements. This is done in chapters 5 and 6. However, an initial abstract analysis is valuable for establishing target parameters for process optimization, including desirable minimum feature and gap sizes, as well as topographical constraints such as the ramp steepness.

This chapter begins by evaluating two topographies and concludes with an overview of the relationship between dimensions and performance of CPW lines. The findings provide insights into the minimum feature sizes likely to be required for optimal performance at a specific frequency range.

3.1 Topography

When it comes to possible topographies for additively manufactured MMIC to PCB interconnects, two approaches directly come to mind: a ramp based version where an MMIC is placed on top of a PCB and ramps provide a smooth transition from the MMIC to the PCB. Secondly, the MMIC and PCB could be placed in such a way that they are on the same height, e.g. by placing the MMIC in a cavity within the PCB or by placing MMIC and PCB on a submount. Both approaches will be discussed in the following sections.

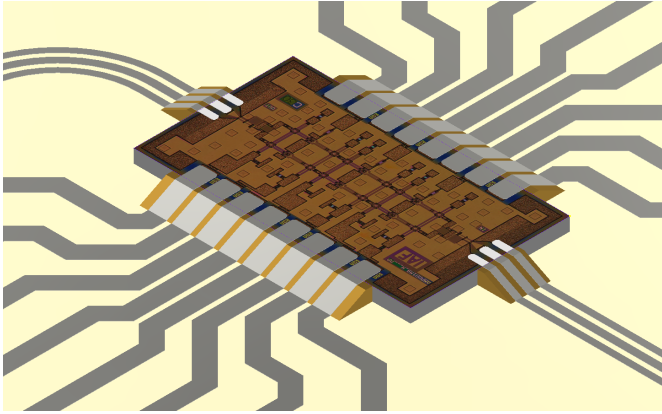


Figure 3.1: Ramp based interconnect design: The MMIC can be placed on top of a PCB and a ramp enables a smooth transition from the top of the PCB to the top of the MMIC.

3.1.1 Ramp-Based Interconnects

The eponymous feature of this topography is the existence of ramps in an interconnect. Those are always necessary when the height of one end of the interconnect does not match the height of the other end. This situation commonly arises when a MMIC is mounted on a PCB, as illustrated in Figure 3.1. This approach offers several advantages, primarily its simplicity and compatibility with standard, cost-effective processes. The MMIC can be placed directly on the PCB without requiring cavities, allowing both MMIC placement and PCB fabrication to utilize well-established manufacturing methods. Furthermore, existing RF PCB designs intended for bond wire interconnects can be adapted to printed interconnects with a modest redesign effort.

Ramp-based interconnects are also attractive in scenarios requiring stacked MMICs, i.e. in applications demanding extremely high integration densities.

Besides these advantages, ramp-based interconnects also have inherent limitations. The additional length required to bridge height differences increases losses, as losses scale with interconnect length. Furthermore, fabricating the ramps introduces an additional manufacturing step, increasing both complexity and potential tolerances. Finally, thermal management for active MMICs can

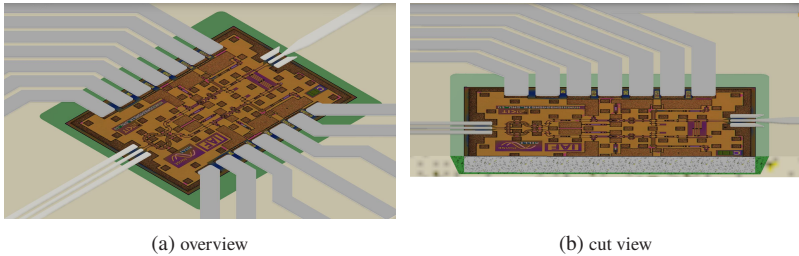


Figure 3.2: Cavity based interconnect design: The MMIC is placed in a cavity in the PCB. The remaining gap between the PCB and the MMIC is filled with a polymer (green) and finally the interconnect is printed between MMIC and PCB. b) reprinted from [16].

be challenging in this topography. Thermal vias may be required beneath the MMIC to dissipate heat, which can create a thermal bottleneck. However, this issue is not unique to ramp-based, printed interconnects and is commonly encountered in other packaging methods, such as bond wires and flip-chip technologies.

3.1.2 Planar Interconnects

To mitigate the intrinsic losses introduced by the length of the ramp, an alternative approach is based on eliminating the height difference altogether. For MMIC to PCB interconnects, this can be achieved by incorporating a cavity into the PCB to house the MMIC, ensuring both components are at the same height, as illustrated in Figure 3.2. When the cavity dimensions closely match the size of the MMIC, the printed interconnect and therefore the losses are as low as possible.

However, this design introduces several challenges. The fabrication of cavities in the PCB requires non-standard and potentially expensive manufacturing processes. Additionally, precise positioning of the MMIC within the cavity is critical, further increasing complexity. Another complication arises from the need to fill the gap between the MMIC and the PCB to provide a continuous substrate for subsequent printing. The smaller the gap, the more difficult it becomes to fill. Another critical consideration is thermal management.

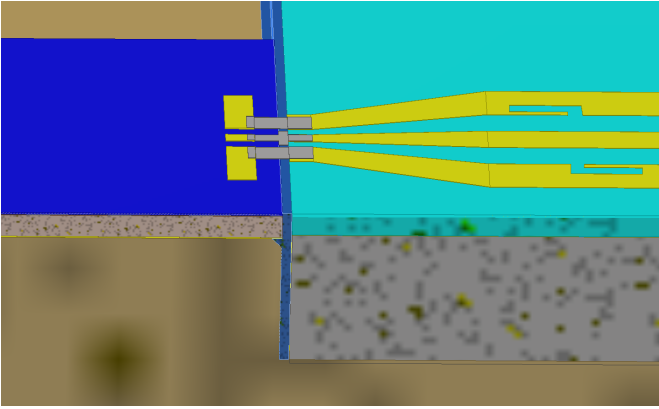


Figure 3.3: Submount-based interconnect design. Two MMICs on the left and right are placed on a submount (brown). The remaining gap is filled with a polymer (vertical blue structure) and the interconnect (silver) is printed over the levelled structure.

Despite these challenges, cavity-based interconnects offer significant advantages. Thermal management can be improved if the design is done right. A PCB cavity can floor at a lower metal layer or go all the way through the PCB so that the MMIC is directly connected to a (metal) back-plane below the PCB. In both cases, thermal conductivity to the heat-sink is improved. However, if the cavity floors on the PCB dielectric, thermal management could also be aggravated.

Alternatively, MMIC and PCB can be placed on a submount providing the leveling functionality. Submounts are typically CNC-machined and made of metal. They eliminate the need for cavities but introduced a new component in the assembly and therefore increases production cost. However, surmounts are commonly used in high-performance RF applications, offer excellent thermal management, and enable a direct transition into a waveguide. Submounts also enable MMIC to MMIC interconnects between MMICs featuring different semiconductor systems and different heights. They thereby are an excellent choice for heterointegration.

A submount-based interconnect is depicted in Figure 3.3. In this design, two MMICs of different height are connected by a printed interconnect.

3.2 Minimum Feature Size

Most RF interconnects exhibit a field configuration similar to that of CPW lines. This is because RF measurement contact pads need the signal and ground contacts in one plane to enable contacting by measurement probes. Consequently, interconnect technologies such as bond wire, flip-chip, and printed interconnects usually follow a GSG pattern, resembling the conductor configuration of CPW lines. As a result, analyzing the performance of CPW lines with varying geometries across different frequencies provides valuable insights into the minimum feature sizes required for printed interconnects.

Figure 2.5b illustrates the key dimensions of a grounded coplanar waveguide. By removing the ground plane and increasing the substrate height, this configuration becomes a standard CPW line. A unique property of CPW lines is the possibility to set the wave impedance through the conductor width (W) and the gap size (S). An infinite number of combinations yields the same impedance. This makes it worthwhile to evaluate how different combinations with the same characteristic impedance affect performance across the frequency spectrum.

To this end, simulations were conducted for a grounded CPW line on a 250 μm -thick alumina substrate ($\epsilon_r = 9.9$) with a 4 μm gold metallization ($\sigma = 4.561 \times 10^7 \text{ S/m}$, $R_a = 0$). The dimensions were selected to yield a characteristic impedance of 50 Ω according to ADS LineCalc, with the gap size S swept from 10 - 40 μm . As demonstrated in [STH03,ZH06], the effective permittivity of the CPW line exhibits a frequency dependence which has also been found here, see Figure 3.4a. This frequency dependence impacts the characteristic impedance in return.

However, a more drastic impact on losses can be found by observing the energy radiated by the CPW transmission lines. Figure 3.4b shows that more power is radiated at higher frequencies and that this loss mechanism is severely aggravated by larger structure sizes. A combination of all loss mechanisms can be found by evaluating the insertion loss of the transmission lines. For a length of 1 mm, the simulated losses of CPW lines with different dimensions forming a 50 Ω characteristic impedance are shown in Figure 3.4c. If a maximum acceptable loss of 1.5 dB/mm is chosen, a maximum operating frequency can be determined for each transmission line. They have been summarized in table 3.1. However, the maximum operating frequencies in this table are only indicators:

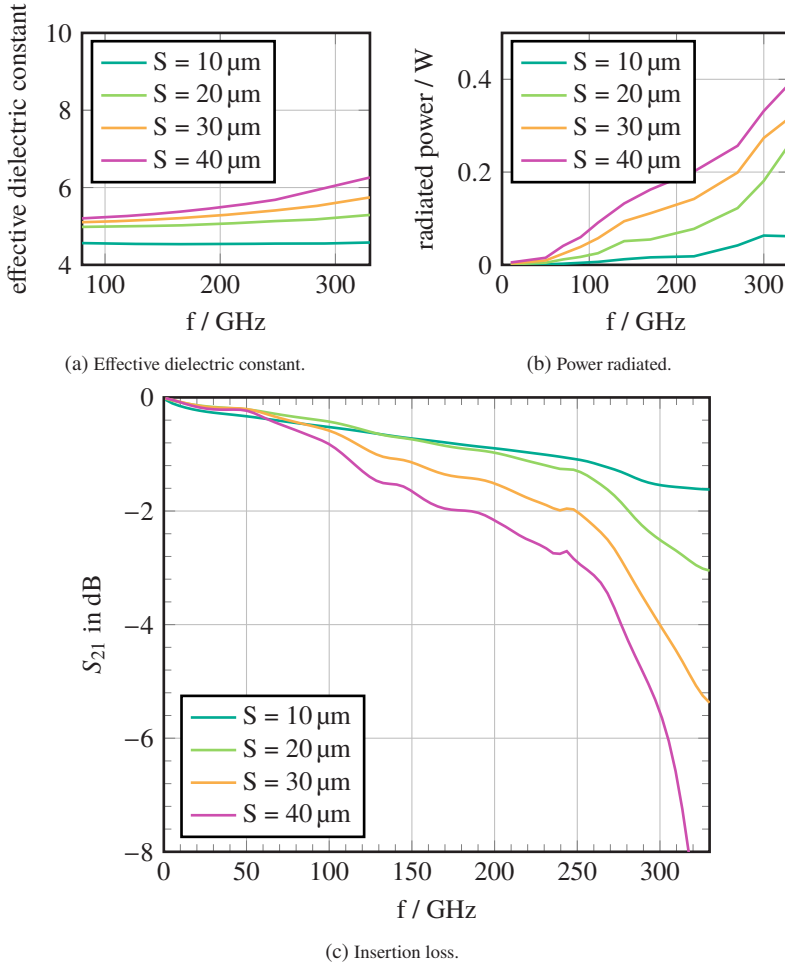


Figure 3.4: The performance of a CPW line degrades at higher frequencies. The plots above show simulated values for a 1 mm long grounded CPW on a 250 μm thick Alumina substrate with 4 μm gold cladding. Different dimensions have been investigated that maintain a 50 Ω characteristic impedance. The conductor width corresponding to the conductor spacing given in the legends are shown in Tab. 3.1.

CPW S	CPW W	Maximum frequency with loss below 1.5 dB
40 μm	69 μm	131 GHz
30 μm	51 μm	198 GHz
20 μm	31 μm	262 GHz
10 μm	12 μm	293 GHz

Table 3.1: Maximum operating frequency for the CPW lines with varying dimensions shown in Fig. 3.4. All lines are designed for $50\ \Omega$ characteristic impedance. The maximum operating frequency has been chosen as the frequency at which the loss per millimeter reaches 1.5 dB.

For any real application, they depend on the materials used, the thickness and conductivity of the conductor as well as the actual dimensions of the transmission line. The trends observed above are independent of those properties but their severity and therefore the maximum operating frequency depends on them.

Nevertheless, these results provide useful guidance for determining desirable minimum feature sizes in the manufacturing process of printed interconnects, given a target operating frequency. Based on the observations above, a minimum feature size of approximately 20 μm , or at least 30 μm , is likely required for operation in D-band (110 - 170 GHz). For H-band interconnects (220 - 330 GHz), achieving minimum feature sizes as small as 10 μm would provide an important performance improvement.

It is of interest to apply those findings to the two printing technologies employed in this work: AJ printing can reliably create a minimum gap size of 20 μm and therefore is best used up to D-Band. UPD printing however is capable of manufacturing feature and gap sizes down to 1 μm and can do so with a certain ease to 5 μm . Therefore, it promises high-performance printed interconnects all the way to H-Band. The following chapter 4 will continue by presenting more constraints introduced by both printing technologies and show how to push them to their limits and beyond.

4 Improving Printer Accuracy: Modifications and Limitations

As discussed in Chapter 3, printed mmW interconnects benefit significantly from structure sizes down to 10 - 20 μm . Achieving such precision necessitates pushing the capabilities of the Aerosol Jet printer to its limits. Therefore, a careful investigation is required to fine-tune the process parameters for optimal printing performance. This chapter explores the constraints imposed by the physical behavior of the printer on line geometry and structure size and provides strategies to utilize the printer for high-precision applications.

In the case of the UPD printer, as outlined in Section 3.1, compensating for height differences between components, such as MMICs and PCBs, is often essential. This is particularly true for ramp-based topographies or cavity-based approaches where the filler material may not achieve a perfectly level surface. Out of the box, the UPD printer supports only manually taught surfaces or planar surfaces for printing. Consequently, developing a process to enable printing on complex surfaces without manual teaching was necessary. Furthermore, this chapter investigates the approximation of printing paths and strategies for compensating for acceleration and deceleration effects during nozzle movement, as detailed in Section 4.2.

4.1 Aerosol Jet Printing

Aerosol Jet printing offers numerous desirable features, including the ability to achieve structure sizes as small as 10 μm while maintaining a nozzle-to-substrate distance of 2 - 5 mm. This flexibility makes the process indifferent to minor variations in substrate height, enabling seamless printing on ramps and planar surfaces alike. Additionally, the printer supports a wide range of materials with viscosities between 1 and 1000 cP, enhancing its versatility.

The following considerations and optimizations have been made for the Optomec AJ5X printer available in our cleanroom. This model also integrates advanced features such as laser sintering, UV curing, and the option to install a 5-axis unit for printing on complex surface geometries. With printing speeds of up to 10 mm/s, and in some cases even 20 mm/s, combined with line widths ranging from 10 - 500 μm , an Aerosol Jet printer ensures rapid production and low manufacturing costs.

However, understanding the printer's limitations and the impact of process parameters such as printing speed and shutter mechanisms on the resulting structures is critical, particularly when targeting feature sizes suitable for mmW applications. The following sections investigate the physical behavior of the printer, identify potential challenges in achieving very small structures, and propose solutions to address these issues.

Chapter 4.1 has been previously published in [5]. Text, structure, images, tables, presentation, and content can show modifications here. The author of this thesis contributed the ideas, observations, measurements, and work presented in Chapters 4.1.1, 4.1.2, and 4.1.3. Florian Häslich proposed that crack formation is caused by drying colloidal films and provided the theoretical background in chapter 4.1.4. Robert Huber contributed his expertise in AJ printing and served as an intellectual sparring partner. Akanksha Bhutani, Uli Lemmer, and Thomas Zwick provided guidance and feedback on the original publication.

4.1.1 Printing Speed Influence on Path Accuracy

Secor [Sec18] and Mahajan et al. [MFF13] have demonstrated in their work, that the printing speed mainly affects the print thickness and not the line width. They have also included comprehensive theoretical explanations. When printing very small-scale structures with high precision, the printing speed exhibits another influence. In this regime, single-digit micron deviations from the desired printing path become relevant and potentially intolerable. Unfortunately, printing small structures at a high speed causes visible deformations. To demonstrate this behavior, we printed a simple rectangular pattern with speeds from 0.5 mm/s to 7 mm/s and varied the side length from 100 μm to 400 μm . The pattern and its deformation can be seen in Figure 4.1e: The actually printed dimension of the rectangle is reduced over the desired value. We call this error

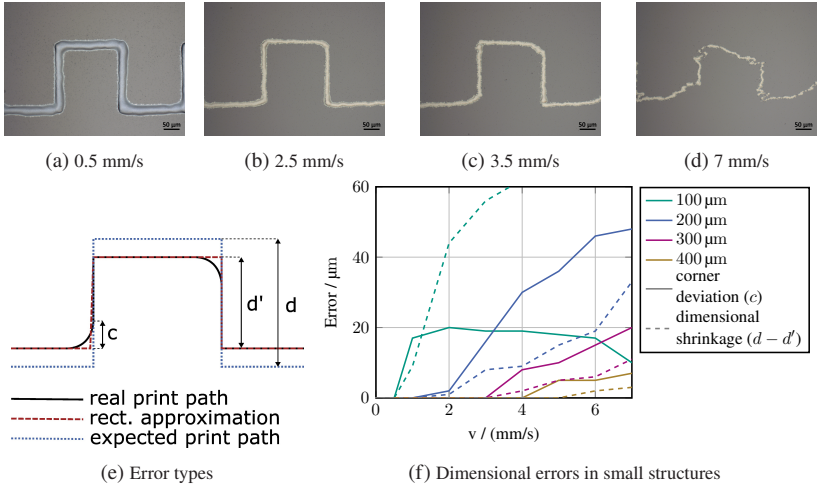


Figure 4.1: Selecting a too high printing speed can cause deformations in small structures. Printed paths and their deformation for printing speeds 0.5 mm/s, 2.5 mm/s, 3.5 mm/s, 7 mm/s are shown in a, b, c and d, respectively. Figure (e) illustrates the types of errors to be expected. The dotted blue line is the programmed print path, the black line is the actually observed print path and the dashed red line is a rectangular approximation of the observed path. We call $d - d'$ the dimensional shrinkage and c the corner deviation. Figure (f) shows measurements of both errors dependent on the printing speed and on the side length d of a rectangular pattern. Solid lines depict the corner deviation and dashed lines show the dimensional shrinkage. Figure reprinted from [5].

$d - d'$ the dimensional shrinkage. Additionally, some corners become rounded. This is called the corner deviation within this thesis. Note that dimensional shrinkage only occurs for the axis that is performing a forth and back movement. In the example displayed here, this is the y-axis. The dimensional shrinkage can hence be seen in the height of the rectangular pattern. If the pattern was rotated by 90° , the x-axis would perform a forth and back movement resulting in a dimensional shrinkage between the left and right lines of the pattern. We measured the dimensional shrinkage for various target side lengths and show it as dashed lines in figure 4.1f. The solid lines describe the corner deformation as defined in figure 4.1e. It can be seen that the errors become negligible for dimensions exceeding $400\ \mu\text{m}$ and that structure sizes of $100\ \mu\text{m}$ and below require printing speeds as low as $0.5\ \text{mm/s}$ to keep the errors at bay. This limitation means that the printing speed cannot be used as a variable to control

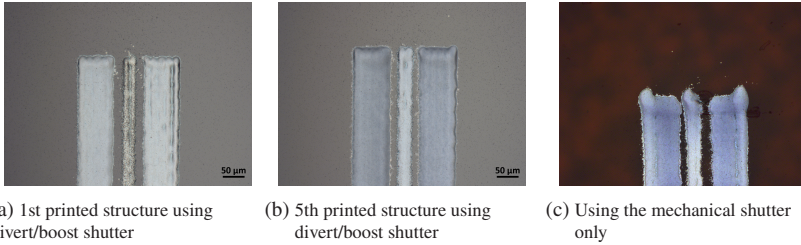


Figure 4.2: The divert/boost shutter causes changing printing behavior over time in the beginning of a printout after a prolonged non-printing period, as seen in (a) and (b). Using the mechanical shutter solves this problem but causes excessive material buildup in the beginning of a print path due to the very fast reaction time and limited printer acceleration. This behavior is shown in subfigure (c) where the left and center structure show a bulge on the top left, and the right structure shows a bulge in the top right corner. Those are the respective start points of the printing paths. Figure reprinted from [5].

the material thickness for ultra-small structures. Instead, the atomizer flow rate, aerosol density, and ink composition have to be utilized for this purpose.

4.1.2 Divert/Boost Shutter and Incremental Deposition Rate

We have discussed in the previous section that very small structures require a low printing speed to maintain a high dimensional accuracy. Thicker layers are the necessary result of slow printing speeds. We will discuss in section 4.1.4 that a high layer thickness can lead to crack formation during drying caused by the surface tension of the evaporating solvent. Therefore, it is often desirable to limit the mass output by selecting a very low atomizer flow rate between 6-15 standard cubic centimeters per minute (SCCM). In this case, the divert/boost shutter has a noticeable influence on the printed material. To demonstrate this behavior, we turned the divert/boost shutter off for multiple minutes, and then printed the same test structure five times directly after each other. The result is shown in Figure 4.2. Figure 4.2a shows the first printout after staying idle and Figure 4.2b shows the fifth printout. The fifth printout is clearly more homogeneous than the first one which means that the printing behavior is not constant directly after turning the divert/boost shutter off for a prolonged time. Unfortunately, turning the shutter off for multiple minutes

cannot be avoided in many situations because substrates need to be placed, alignment markers need to be found, and so on. Small structures often have a short printing time so that a significant percentage of the print is performed in the phase of non-constant printing behavior, which reduces the reproducibility of the results. A possible solution could be to define a dumpsite that the printer goes to before every printout. A more reliable and consistent solution would be to reduce the use of the divert/boost shutter and combine it with the mechanical shutter: The divert/boost shutter is only used for prolonged non-printing periods to prevent the mechanical shutter spoon from filling up. Shortly before the print starts and during the print, only the mechanical shutter is used to avoid the influence of the divert/boost shutter. This approach has been used for the print in figure 4.2c. The influence from the divert/boost shutter has effectively been removed, but another aggravating effect can be observed: The response time of the mechanical shutter is extremely fast - between 2 - 5 ms - which makes the acceleration of the printer visible. In the positions where the printing paths start (the corners in the above figure) an excessive material buildup can be observed because the mass output is constant but the velocity is not. The remedy for this problem is using shutter on the fly, which will be discussed in the next section.

4.1.3 Shutter On The Fly - Debugging the Printer

Shutter on the fly is a special option for the printing path creation offered by Optomec for its AJ printers. The idea is shown in figure 4.3c: The movement starts with the shutter closed and it is only opened when the printhead is already accelerated to the desired printing speed. In the same way, the shutter is turned off again while the printer is still moving at the desired speed and the deceleration is done in a non-printing movement. This approach allows removing acceleration and deceleration effects from the printed lines. There are two crucial requirements for this mode of operations: First, that the on/off timing of the shutter is well known. Second, that it is constant. Both are required to calculate the positions at which the shutter needs to be operated. Unfortunately, the default code produces the result shown in figure 4.3a in the top: there are long lead-in lines attached to the desired structures, which indicates that the calculation of the shutter open position is flawed. By performing a series of tests, we were able to exclude the shutter timing and the assumed values for the acceleration and jerk of the printer as culprits and found an imprecision in

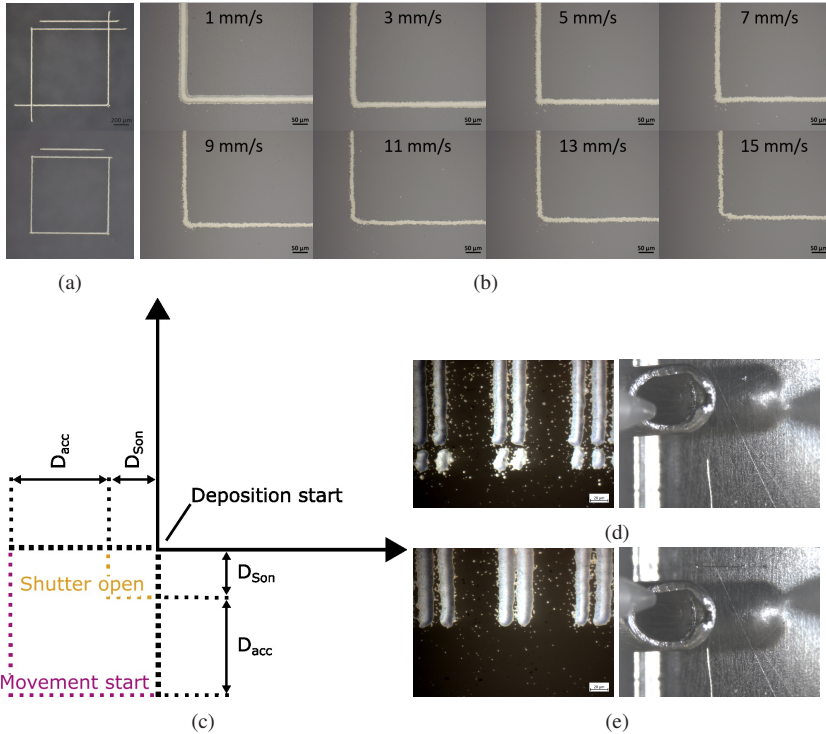


Figure 4.3: (a) A non-optimized shutter on the fly calculation routine causes long lead-in lines (top) in the SOTF test structure (bottom), which is composed of four individually printed lines forming a square and one base line. (b) The optimized SOTF subroutine code eliminates the undesired lead-in lines completely. (c) Schematic working principle of SOTF. The movement starts at the purple position. When the printer reaches the orange "shutter open" position, it is moving already at the desired printing speed and opens the shutter. Due to the shutter open time, the printed line only starts D_{Son} later. (d) Positioning the spoon too far to the back of the printer causes undesired ink splashes at the line ends. The spoon moves towards the upper end of the image to open. (e) Correctly positioning the spoon eliminates them. Figure reprinted from [5].

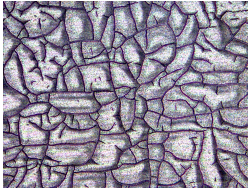
the SOTF calculation subroutine as the error source. This subroutine calculates the position where the shutter needs to be turned on and the position where the movement starts in dependence of the desired printing velocity and the first line to be printed. We implemented an improved SOTF calculation subroutine, that reduces the complexity of the calculations and is more error resistant since we only require approximate knowledge of the printer acceleration and jerk. We ensure that the distance D_{acc} is long enough for the printer to be moving at the desired printing velocity at the shutter open position. The distance of this position to the first printed point, D_{Son} , can then be calculated with a simple motion equation:

$$D_{\text{acc}} = 0.5 \cdot a \cdot v_{\text{print}}/j + 0.5 \cdot v_{\text{print}}^2/a \quad (4.1)$$

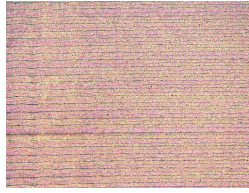
$$D_{\text{Son}} = v_{\text{print}} \cdot t_{\text{Son}}, \quad (4.2)$$

where a is the acceleration, and j is the jerk of the printer, v_{print} is the desired printing velocity, and t_{Son} is the opening time of the shutter. Taking into account the angle of the first printed line, the x and y coordinates of the start point of the movement and of the actuation point of the shutter can be calculated. The resulting code for the ACS motion controller used in the AJ5X printer is given in the appendix. Note that only the code for the calculation of the start point is shown there, because the calculation of the shutter-off point has not been changed and this part of the code is proprietary to Optomec. We found through experiments that acceleration distances below 300 μm always cause defects even though they should theoretically be sufficient for a very low printing speed. This might be caused by higher order derivatives of the position that are not accounted for in the calculation or by delays stemming from the motion controller. However, it is simple to avoid this problem with an if-clause that ensures a minimum acceleration distance.

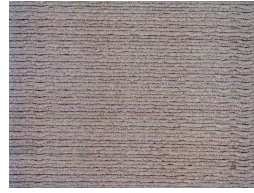
We ran thorough tests of our code using the mechanical shutter and the test structure shown in figure 4.3a in the bottom. The square is composed of four individually printed lines which allows seeing any deficiency of the SOTF routine in the corners where the lines would either not touch or form a cross if anything was off. We then swept the printing speed over a range from 1 mm/s to 15 mm/s and found the improved SOTF calculation subroutine to work perfectly for the entire range as can be seen in figure 4.3b. This figure shows a zoom into the corner where both lines start. It can be seen that there is neither a gap nor a cross for any tested speed.



(a) Silver ink sintered on a non-preheated hotplate



(b) Sintering on a preheated hotplate can avoid cracks



(c) Photonic sintering can avoid cracks as well

Figure 4.4: Three printed silver surfaces. The crack formation in (a) is caused by drying the ink before sintering it as it happens when using a non-preheated hotplate. Using a preheated hotplate or photonic sintering can avoid this effect. Reprinted from [5].

There is one more source of error when using SOTF with the mechanical shutter: The movement of the mechanical shutter is very fast and the system is designed in a way that allows minor vibrations. This means that the spoon must not be centered around the printing nozzle but placed more towards the front of the printer in the off-position. This placement avoids a short reopening of the shutter because of vibrations when the shutter is turned off. The effect of an improperly placed spoon is depicted in figure 4.3d and the correct placement is shown in figure 4.3e. This consideration is only relevant for very small printed features and could be ignored for wide lines since the distance and size of this effect would be insignificant compared to the line width.

4.1.4 Crack Formation and Prevention

A common defect for printed silver is the formation of cracks within the printed structures. Most often, those cracks are detected after the sintering step. However, they are often not caused by the actual sintering but by the previous drying of the ink. The mechanics of this defect will be briefly described in the following together with adequate countermeasures. During evaporation-based drying of colloidal films, a drying front can be observed that moves from the edges to the center. This process causes a buildup of capillary pressure which puts a tensile stress oriented orthogonally to the drying front on the film. It is relieved through cracks, that can be frequently observed in drying processes [TR05]. Those defects only occur in films with a height above a critical thickness, that depends on particle size, rigidity and packing [ST07]. The

commonly used silver nanoparticle inks form a colloidal film after printing and before sintering. If the printed structures exceed a critical thickness, capillary pressure buildup during evaporation-based drying causes cracks in AJ printed silver [DGH⁺19]. Since nanoparticles are by definition very small (around 35 nm for Novacentrix JS-A221AE, the ink used for AJ printing in this work), the critical thickness is small as well and can be exceeded during printing. It was shown in the section about the printing speed that ultra-fine features require a slow printing speed which results in a higher material thickness. This can make it impossible to stay below the critical thickness for some applications which causes cracks if the film is allowed to dry completely before sintering. If sintering starts before the film is fully dried on the other hand, sintering necks emerge that increase the particle to particle bonding significantly above the previously predominant van der Waals force. They can resist the capillary pressure and thereby prevent cracks.

We want to point out two common causes for drying and hence cracks in AJ printing. One stems directly from the creation of the printing paths: In many scenarios it is tempting to start a job and perform other tasks while the printer is running, especially since large prints with fine features require a low printing speed and hence consume a considerable amount of time. In the end of a print, the printer stays in the last position and turns off the divert/boost shutter. Consequently, a constant stream of dry nitrogen leaves the nozzle, flows over the printed structure and dries it. Adding a movement command to the end of the printing script file that moves the printhead away from the printout solves this problem.

The second relevant mechanism appears when the prints are thermally sintered in a non-preheated oven or hotplate. Before a sufficiently high temperature for the formation of sintering necks is reached, the solvent left in the ink can evaporate and the printout dries. Using a preheated oven or hotplate can solve this issue. The same is true for photonic sintering, e.g. in a Novacentrix PulseForge machine. Figure 4.4 shows cracks caused by sintering on a non-preheated hotplate and the exact same structure sintered on a preheated hotplate and in a Novacentrix PulseForge 1200 photonic sintering machine. Both of them effectively avoid cracks.

The observations made in this section are heavily dependent on the utilized ink. The physical principle of crack formation in drying colloidal films is not, however. The ink only influences the critical thickness. We have presented two

approaches, that can work for many applications but that don't claim generality. Every material and project requires its idiosyncratic solutions, but it can be very helpful to understand the processes leading to cracks. Despite one's intuition, cracks can also be formed while the ink is drying and not only during the sintering step because of a CTE mismatch. Knowledge of possible sources of the observed defects, allows finding adequate solutions to them.

4.1.5 Summary on AJ Process Considerations and Improvements

Printing features below 200 μm and down to 10 μm with an accuracy better than 20 μm means pushing an AJ printer to its limits. Considerations and effects become important that can be neglected in other regimes of operation. We showed that the printing speed needs to be chosen according to the geometrical accuracy requirement of the design. Unlike for printing large structures, the printing speed cannot be used to control the print thickness. This is why a very low atomizer gas flow, low aerosol density, and cautious ink composition need to be used to limit the material thickness.

We demonstrated that the divert/boost shutter can cause a non-constant printing behavior after a significant off-time. Using the mechanical shutter and SOTF is an excellent remedy for many problems, because it removes the influence of the divert/boost shutter and any acceleration effects. We improved the SOTF calculation subroutine and included a thorough test over a wide range of printing speeds which shows that our calculation approach is indeed robust and yields an extremely high precision. We also discussed the importance of the shutter spoon placement to avoid satellite lines.

Finally, we showed that drying the ink can cause cracks and suggested two alternative sintering procedures that can avoid them. Altogether, we presented a wide range of potential pitfalls for printing ultra-small and highly precise structures with an AJ printer. For each of those potential difficulties we presented a solution. We summarized the considerations that need to be kept in mind for ultra-fine feature and highly precise AJ printing in the flow-chart in figure 4.5.

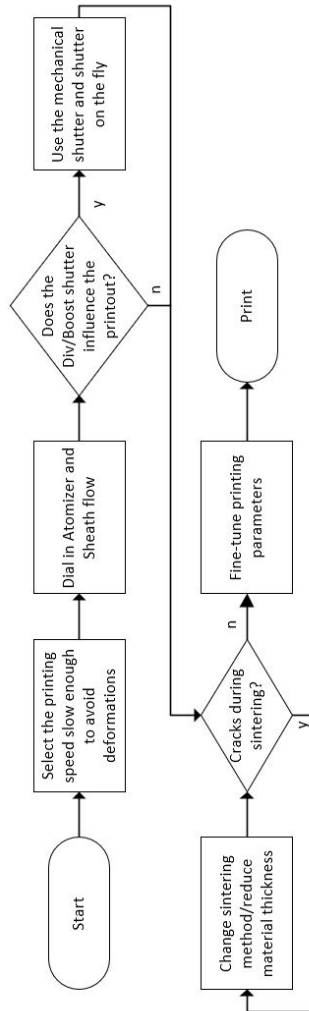


Figure 4.5: We suggest following this flow-chart to develop a process for ultra-fine feature AJ printing: Start with the printing speed, select the shutter mechanism, potentially fix the sintering or curing process and finally fine-tune the printing parameters. Figure reprinted from [5].

4.2 UPD Printing

Many challenges associated with AJ printing are inherently solved in UPD printing. For example, printing is typically performed at velocities between 0.01 - 0.2 mm/s, which naturally avoids path deformations caused by rapid movements. Additionally, UPD printing does not produce overspray, making it easier to print small gaps without risking short circuits. The slow response time of the applied pressure (in the order of seconds) eliminates the need for shutter-on-the-fly mechanisms. However, this slow pressure adjustment introduces new considerations necessary to prevent material buildup, which will be discussed in the following sections.

The most significant challenge in UPD printing arises from the requirement that the nozzle must remain in constant contact with the substrate. For substrates that are not perfectly flat - such as those used in ramp-based topographies for printed interconnects - the printing paths must precisely accommodate the surface geometry. Out of the box, this capability is limited to manually teaching the surface profile, a labor-intensive process that is impractical for larger production volumes. To address this limitation, an automated 3D printing path creation method has been developed, which will be detailed in the following sections.

Additionally, this section will discuss other challenges unique to UPD printing, particularly those encountered when striving for maximum precision. They comprise material buildup due to slowly changing pressure, nozzle drift, and alignment precision.

Chapter 4.2 has been previously published in [6]. Text, structure, images, tables, presentation, and content can show modifications here. The author of this thesis contributed the idea of using a custom program to project 2D paths onto measured profiles or surfaces for 3D-printing path generation. The initial projection program was developed by Jonathan Wendel during his bachelor's thesis, which was supervised by Georg Gramlich and Martin Roemhild. It was subsequently modified and further improved by Georg Gramlich in cooperation with Lilli Weiss, who conducted extensive testing. The leveling procedure detailed in Chapters 4.2.2 and 4.2.4 was developed by Georg Gramlich and Lilli Weiss during her bachelor's thesis. The analysis of different projection methods and line homogeneity presented in chapter 4.2.1 and 4.2.7 was carried out by Georg Gramlich, while Martin Roemhild contributed the idea of approximating

lines using segments of constant length. Martin Roemhild was the first to observe nozzle drift, and Georg Gramlich conducted the systematic analysis of this phenomenon presented in chapter 4.2.6. The importance of alignment and its mathematical formulation, as presented in chapter 4.2.4, was developed by Georg Gramlich, who also fabricated the demonstrators shown in Chapter 4.2.5. Holger Baur provided valuable expertise in printing and microelectronic manufacturing techniques. Norbert Fruehauf, Akanksha Bhutani, and Thomas Zwick offered guidance and feedback on the original publication.

4.2.1 Semi-Automatic Conformal Printing by Path Projection

One has to choose between two fundamentally different approaches when developing conformal printing with a direct write system. One option is to measure the surface height in situ and modify the printing paths within the printer during the printing process. In this case, the surface geometry can either be measured prior to printing (e.g. leveling procedures in modern FDM 3D-printers or the manually scripted approaches for conformal UPD printing) or it can be measured continuously during the printing process itself. Both of those options require a sensor within the printer. Since such a sensor is not available in our printer, and we wanted to develop a versatile approach that does not require complicated and expensive hardware modifications, we opted for another possibility: measuring the surface outside the printer, projecting the printing paths onto it and creating 3D-printing paths to be loaded into the printer. This option has the outstanding advantage to leverage pre-existing surface measurement equipment available in many labs and not to require any additional investment. The obvious drawback is, that good alignment is required as we will discuss in section 4.2.4.

Since the UPD printer is only capable of printing straight lines, each surface needs to be approximated by linear segments, which can be done in multiple ways. Figure 4.6 shows the three options for the approximation for which we will discuss the drawbacks and advantages. All projection algorithms should take care of edge prevention and leave long flat lines untouched, which can be achieved through additional checks. The graphics in figure 4.6 are all created under the assumption that those additional precautions are taken.

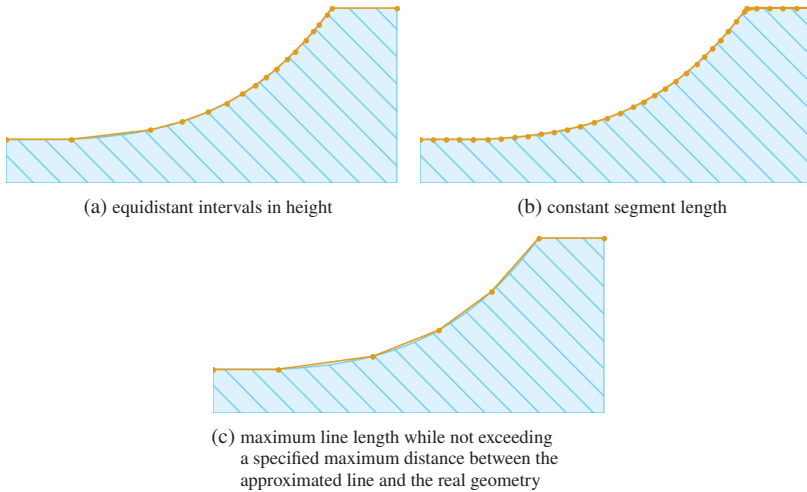


Figure 4.6: Multiple approaches to approximating a complex surface with linear segments. Dots depict the end of each segment and hence also show the locations at which printed lines will more likely show bulges.

The first option to approximate a complex surface profile by linear segments is shown in figure 4.6a. A new point is inserted every time the height of the surface changes by a specified amount. This approach is somewhat intuitive for the UPD printing system because it allows to always change the height of the nozzle once the nozzle slack has been reached exhausted. The downsides of this approach are the creation of many short segments which means longer printing times, and a high volatility in segment length dependent on the incline of the substrate, which can lead to less homogeneous line geometries.

Secondly, the surface can be approximated by segments of a constant length as shown in figure 4.6a. The advantage over the previous length lies in the constant segment length with makes it easier to optimize the printing parameters for a uniform line geometry. On the downside, the segment length has to be chosen small enough to approximate the real geometry sufficiently well which means using a short segment length in most applications which in turn means a long printing time.

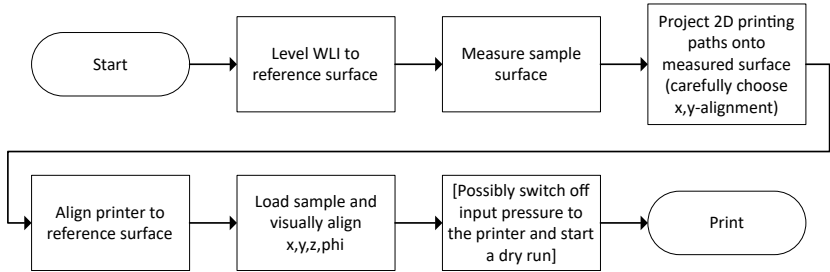


Figure 4.7: This flow chart illustrates the necessary steps to print onto a complex surface topography with the semi-automatic projection approach presented developed in this work. Some steps are optional: Alignment to a reference surface only needs to be checked sporadically, and the dry run without pressure applied can be omitted for rather simple surfaces or less important samples. Figure reprinted from [6].

The last option presented here is also the most complex one. The surface is approximated with the lowest number of segments possible while not exceeding a maximum height difference between the approximated surface and the real surface, see figure 4.6c. This allows to stay within the nozzle slack while significantly reducing the printing time. Since fewer segments are needed, many of them also become long enough to utilize the `veclineramp` command which increases the line uniformity, see chapter 2.3.2 for an explanation of this command. On the other hand, this means that some segments might be too short to use the `veclineramp` command which will require additional care to ensure homogeneous lines.

4.2.2 Conformal Printing Workflow

This section elaborates on the required workflow for semi-automatic conformal printing onto complex surfaces with the approach presented above. Alignment between the measured sample surface and the sample in the printer needs to be excellent as will be discussed in chapter 4.2.4. Rotational misalignment around the x- and y-axes can be avoided by leveling the WLI and printer to the same reference substrate. In other words, levelling the WLI and the printer to the same flat surface ensures, that all surface tilts, steps, etc. in the measurement data will also be found on the sample surface in the printer. A simple glass slide or even a silicon wafer does an excellent job as reference surface. Once the

WLI has been leveled, the sample surface can be measured, potentially using x,y-stitching for print areas exceeding the field of view. Since the WLI has been leveled to a reference substrate, it is crucial not to perform any digital levelling steps in the post-processing of the measurement data.

The measurement data needs to be exported into a .sdf file format which then can be loaded into the projection program developed within this work. The 2D printing paths are designed in AutoCAD and imported into the projection program as a .dxf file. It is crucial to know the precise location where the origin of the printing paths in the .dxf file is to be placed on the measured surface. This location can be measured e.g. in Vision64 for Bruker WLIs and needs to be entered into the projection program. This program also allows to correct for a rotational misalignment between printing paths in the .dxf file and measured surface by virtually rotating the surface around the z-axis. Once the projection algorithm has been chosen, the printing paths can be projected onto the surface and a printfile can be exported.

Next, the printer needs to be levelled to the same reference surface used for the WLI before loading the sample. Once the nozzle has been visually aligned to the origin of the print paths, the printfile can be loaded and the print can be started. However, it can be wise to check the correct alignment by shutting off the output of the pressure amplifier, releasing the pressure in the tubing connecting the pressure amplifier to the printer, and starting the print with no input pressure. In this way, the nozzle movement across the surface can be observed without ink deposition and the correct alignment can be verified. The explanation of the suggested workflow has been summarized in Fig. 4.7.

4.2.3 Conformal Printing Execution Time

The most important metrics for the projection algorithms presented in section 4.2.1 are how many points are needed to map the printing paths to the surface, the printing time, and the smoothness of the resulting prints. To evaluate the first two metrics, we have created two ideal surface files and projected printing paths onto them. The first surface is a linear ramp of 100 μm height and length, resulting in a slope of 45° . The second one is the first half of a sinus curve spanning over a length of 200 μm with a height of 100 μm . Both profiles start and end with a 50 μm long flat segment. The yz-profiles of the printing paths are

shown in table 4.1. The shown paths are printed as five parallel lines forming a $200\text{ }\mu\text{m}$ wide surface. The projected printing paths onto the ramp-shaped surface as displayed in our projection program is shown in figure 4.8. The printing times in table 4.1 have been measured by running the generated scripts in the printer without a nozzle connected. The lineramp command has been used with a $10\text{ }\mu\text{m}$ ramp up and a $40\text{ }\mu\text{m}$ ramp down distance. All lines with a length of $5\text{ }\mu\text{m}$ or less were printed without the lineramp command. The segment length for the equidistant segment projection method was $5\text{ }\mu\text{m}$ which means that this projection did not utilize the lineramp command at all. The z step height as well as the maximum allowed distance between the projected path and the real geometry have been set to $1\text{ }\mu\text{m}$.

Table 4.1: Evaluation of the three discussed projection algorithms. Two artificial surfaces have been used to evaluate the number of points required to map the printing paths to the surface and to measure the printing time. The printing paths consist of five parallel lines spanning from the beginning to the end of the profiles shown in the second line. Table reprinted from [6].





Projection method	Number of points		Printing time / s	
				
Equidistant height	510	760	197	298
Constant segments	245	395	108	174
Longest segments	20	350	56	197

Table 4.1 shows that the equidistant height projection method is the least favorable one. It requires the longest printing time and the largest number of points. The other two algorithms show a similar performance and the choice has to be made based on knowledge of the surface topography to be printed on: If the surface can be approximated by long segments ($80\text{ }\mu\text{m}$ and above), the longest segments method yields high uniformity and the shortest printing time. This is the case for the ramp shaped surface in the table. However, if the approximation requires many short segments, as for the sinusoidal surface in the table, the constant segments method will achieve higher uniformity and a similar or lower printing time.

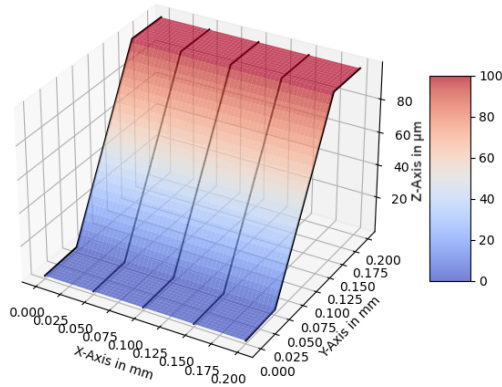


Figure 4.8: The projected printing paths on the ideal ramp shaped surface utilized in the analysis of the projection algorithms as shown in table 4.1. Reprinted from [6].

4.2.4 Importance of Alignment for Conformal Printing

In most printing systems, the importance of alignment is evident. Misalignment leads to a shift in the deposited structure and can cause functional defects. In conformal printing with the UPD system, alignment plays an even more critical role. If the surface to be printed on is shifted, tilted, or rotated relative to the 3D printing paths, the nozzle may either crash into the substrate or lose contact. In the first case, the nozzle can be damaged. In the second case, ink deposition is interrupted. Both scenarios result in a defective printout.

In this section, we investigate the precision required for alignment depending on the surface to be printed on.

The first important consideration is the acceptable height deviation along the z-axis. In Chapter 2.3.2, we discussed that the nozzle is made of very thin glass and therefore is slightly flexible. The z-axis can be lowered by approximately 10 μm beyond the point of contact without damaging the nozzle. This is referred to as overtravel. However, excessive bending of the nozzle reduces the accuracy of the printed structures and increases the risk of breakage. To mitigate this, it is good practice to keep the initial overtravel below 3 μm . Since ink deposition

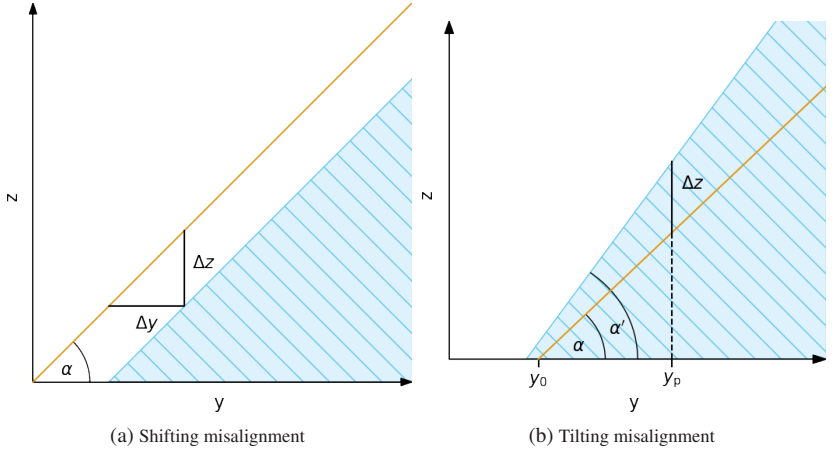


Figure 4.9: Misalignment mechanisms for conformal printing. The orange line depicts the surface that has been measured, that the printing path is projected on, and therefore the path that the nozzle follows. The blue face represents the surface actually found in the printer. a) shows misalignment by shifting, while b) shows a tilting misalignment. Reprinted from [6].

remains continuous up to a substrate-to-nozzle distance of $1\text{ }\mu\text{m}$, deviations of up to $\pm 4\text{ }\mu\text{m}$ between the 3D printing path and the actual substrate can be tolerated when using $3\text{ }\mu\text{m}$ overtravel.

Having established the maximum tolerable z-height inaccuracy, we now examine different types of misalignment. First, the print paths may be shifted along any axis relative to the surface. Second, the surface in the printer may be tilted along the x- or y-axis. Third, the surface may be rotated around the z-axis. Rotational misalignment can typically be avoided, as the stage can be rotated, and since most structures have sufficiently discernible features for precise rotational alignment. For this reason, we focus on shifted and tilted surfaces in this section.

To facilitate understanding and visualization, we assume a ramp-shaped surface along the y-axis that is independent of the x-axis. This is shown in figure 4.9 where the measured surface and the corresponding printing paths are orange, while the actual (shifted or tilted) surface is represented by the blue face.

Shifting the print paths relative to the surface in the printer can easily occur if the print job's starting point is not carefully chosen. A shift in the z -direction is straightforward: any micrometer misalignment directly translates to a micrometer displacement between the print path and the real surface. Misalignment in the x - and y -directions, however, presents a more complex issue.

Figure 4.9a illustrates the effect of a misplaced starting point by a distance of Δy when the surface inclination is α . The resulting displacement Δz can be calculated as:

$$\Delta z = \Delta y \cdot \tan(\alpha). \quad (4.3)$$

As expected, a larger misalignment leads to a greater distance between the nozzle and the surface. Additionally, the equation shows that misalignment becomes more critical as the surface inclination increases. When the maximum inclination of the surface to be printed on is 45° , for example, a $3\text{ }\mu\text{m}$ misalignment leads to a maximum z -misalignment of $3\text{ }\mu\text{m}$.

The second type of misalignment worth investigating is a tilted surface. Figure 4.9b depicts a ramp along the y -axis where the surface is tilted around the x -axis. Again, the measured surface and hence the print paths are displayed in orange, while the actual surface in the printer is shown as a blue face.

In the measurement data, the surface is at a zero z -height at y_0 , and the inclination is α . The additional tilt around the x -axis is given by $\Delta\alpha$ so that the inclination of the actual surface is $\alpha' = \alpha + \Delta\alpha$. When printing at a distance y_p from the starting point, the additional compression of the nozzle is:

$$\begin{aligned} \Delta z = & y_p \cdot [\tan(\alpha + \Delta\alpha) - \tan(\alpha)] \\ & + y_0 \tan(\alpha) \cdot [1 - \cos(\Delta\alpha) - \tan(\alpha + \Delta\alpha) \sin(\Delta\alpha)]. \end{aligned} \quad (4.4)$$

Since the tilt $\Delta\alpha$ is typically small, the small-angle approximation can be applied, simplifying the equation to:

$$\Delta z = y_p \cdot [\tan(\alpha + \Delta\alpha) - \tan(\alpha)] - y_0 \Delta\alpha \tan(\alpha) \tan(\alpha + \Delta\alpha) \quad (4.5)$$

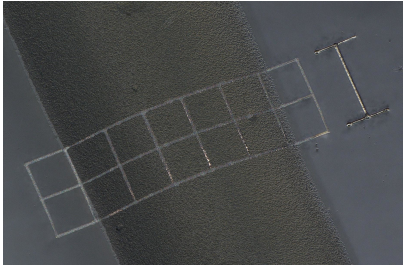
The above equation shows that the deviation worsens for steeper surfaces. It is also aggravated when printing farther from the start point (y_p) and when the slope is positioned farther from the start point (y_0).

From our experience, it is typically possible to keep misalignment in the x- and y-directions within $\pm 3 \mu\text{m}$. Since the maximum slope to be printed on is known from the measured surface data, equation 4.3 can be used to calculate the maximum expected height deviation from x,y-misalignment and, therefore, the remaining nozzle slack. Subsequently, the maximum permissible tilt can be determined with equation 4.5.

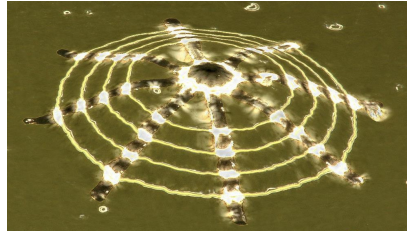
In Chapter 4.2.2, we introduced an approach for eliminating tilts by leveling both, the surface measurement equipment (e.g., WLI), and the printer to the same reference surface. By following this method, we have consistently achieved tilt values ($\Delta\alpha$) too small to detect, enabling us to print onto steeper surfaces since only shifting misalignment needs to be considered.

4.2.5 Semi-Automatic Conformal Printing Demonstrators

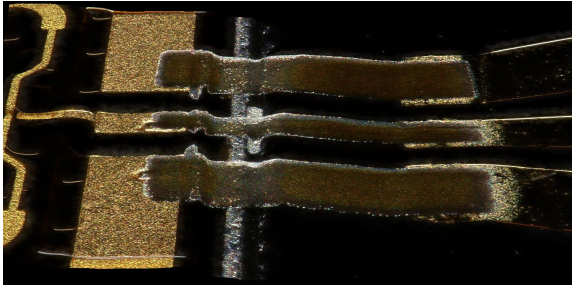
We have manufactured some demonstrators showing the capabilities of our semi-automatic conformal micro-metal printing approach. We used two different substrates to print on: The first one is a glue line dispensed on a glass slide. It has a width of $540 \mu\text{m}$ and a height of $43 \mu\text{m}$. The slope is hence small and alignment easy as we discussed in section 4.2.4. We printed a $100 \mu\text{m}$ mesh over this line and a $200 \mu\text{m}$ scale bar next to it as seen in figure 4.10a. The second substrate we used is μSLA printed by horizon microtechnologies. It shows a cylindrical pyramid with a total height of $43 \mu\text{m}$ and near vertical $5 \mu\text{m}$ steps. Those steps make excellent alignment crucial. We have printed a star over this pyramid to demonstrate that printing in any direction is possible with our approach to conformal printing. It also shows that the surface to be printed on does not need to show uniformity in any dimension since we project the printing paths on a full 3D surface measurement.



(a) Printed silver mesh over a glue line with a printed 200 μm scale bar. The height of the glue line is 43 μm . Reprinted from [6].



(b) Star printed over a circular pyramid with a height of 47 μm . The vertical steps make alignment crucial for this print. Reprinted from [6].



(c) An application example: A printed radio frequency interconnect between two monolithic microwave integrated circuits on a complex surface topology. Reprinted from [6].

Another demonstration of the power of the semi-automatic conformal printing approach presented here comes from our own applications: We have put it to use to print a radio frequency interconnect between two monolithic microwave integrated circuits with a complex topology. This application can be seen in figure 4.10c. It can be seen, that the center conductor becomes significantly wider after approximately one third of the length. This is intentional behavior to compensate for changes in the dielectric properties of the material below the interconnect and shows the excellent alignment of the printed structure.

4.2.6 Nozzle Drift

During long print jobs on the UPD printer, nozzle drift can sometimes be observed. This phenomenon becomes apparent when the print-head is commanded

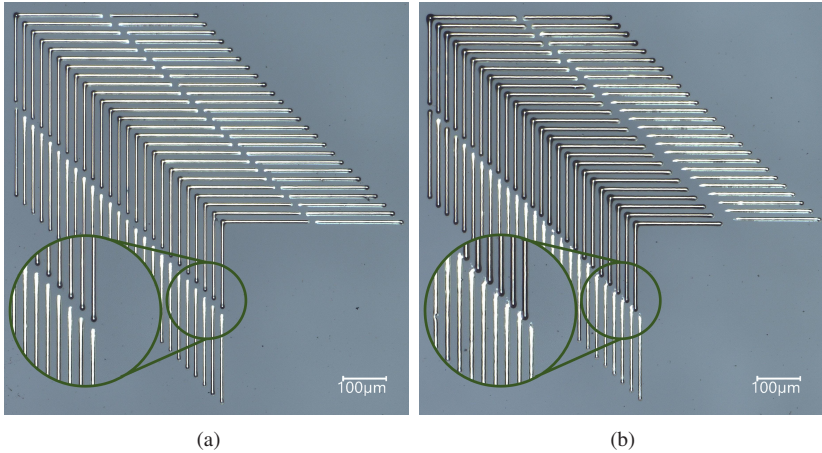


Figure 4.11: Structures printed during a long term stability test. The inner part of the structure is printed in the beginning of each iteration. Two adjacent completing lines are then separated by a 5 min jog motion, making it possible to observe the nozzle drift over time and distance. a) shows little drift while b) shows a significant nozzle drift in x-direction, as visible from the misalignment of the original and continued vertical line segments. Reprinted from [6].

to return to the starting position after completing a print job and is found to be misplaced. Nozzle drift can occur along all axes and directly impacts the accuracy of printed structures. To systematically investigate this effect, we developed an experimental procedure to analyze and quantify nozzle drift.

Experimental Setup

The experiment begins by printing a set of equidistant L-shaped alignment patterns directly after each other. Since these structures are printed consecutively, the drift between them is assumed to be minimal. After printing this initial reference pattern, the printer undergoes a series of non-printing jog movements or idles for 5 min before resuming the print job by extending one vertical and one horizontal line from the previously printed pattern. Nozzle drift is made visible by misalignment between the original and the extended line segments. This process is repeated until all alignment patterns are completed.

By measuring the offset between the original and extended lines, the drift in the x- and y-directions can be quantified, while the drift in the z-direction is directly measured using the printer's built-in substrate detection routine. A completed pattern with minimal nozzle drift is shown in Fig. 4.11a while Fig. 4.11b exhibits severe nozzle drift in x-direction. In this experiment, the jog/idle period was 5 min and a total of 25 alignment structures was printed, resulting in a print time of approximately 2 h per structure.

A total of 12 test structures were fabricated, with three successive structures undergoing the same 5 min jog movement between adjacent L-patterns. Since it also takes time to print the initial patterns, the continued line segments, performing the z-detection, and since the nozzle was rinsed for 30 s before continuing a pattern, the total time per test structure was approximately 8 h. The total runtime of the experiment and hence the time over which nozzle drift has been analyzed was 32 h and 16 min.

The following jog movements were investigated:

1. A diagonal back-and-forth movement of 50 mm in x and y and 10 mm in z,
2. The same movement pattern as above but with all distances scaled by a factor of 0.01,
3. No movement at all but an idle wait time of 5 min,
4. A movement pattern corresponding to filling a 100 μm -long pad in y-direction with lines spaced at a pitch of 3 μm .

Each jog movement was repeated until 5 min had elapsed. Following each jog section, the nozzle was rinsed for 30 s. To track all movements made by the nozzle including rinsing etc., the movement commands (`vecmoveto`, `moveby`, `moveto`) were modified to log the traveled distance. Before extending an alignment structure, the total displacement along each axis and the elapsed time were recorded. This approach allowed for an evaluation of nozzle drift as a function of both time and distance moved.

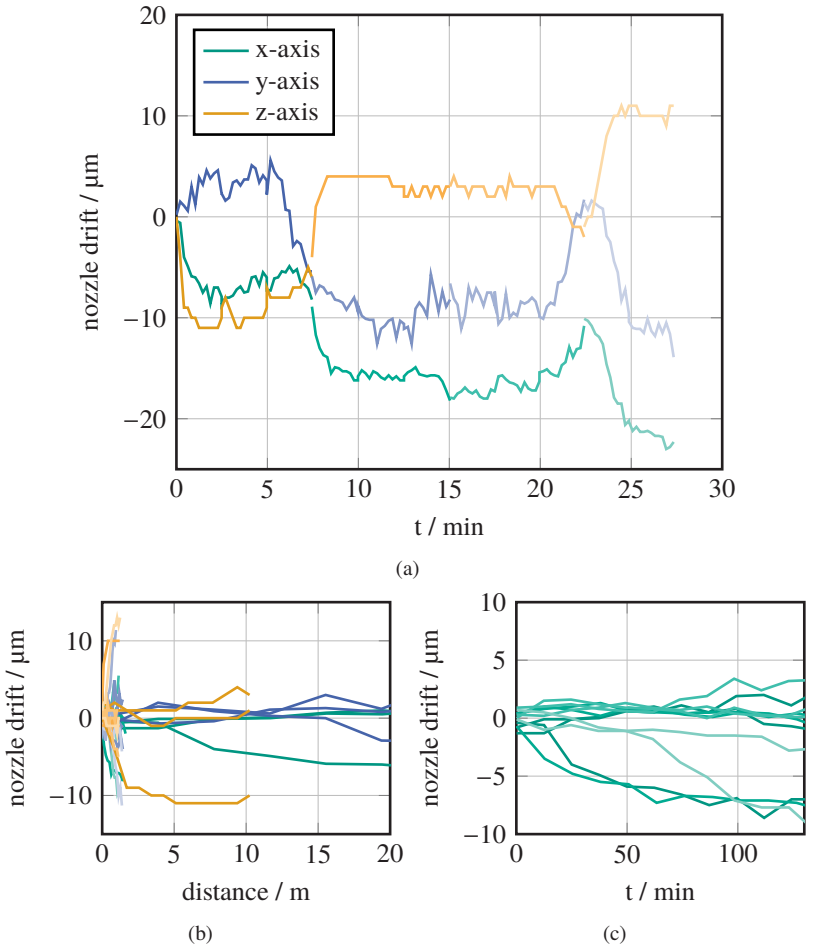


Figure 4.12: Measured nozzle drift in the UPD printer during a long term test. Jog movements are differentiated by color saturation while axes are color-coded according to the legend in a). The plots show that nozzle drift is time-dependent rather than distance-dependent, but no pattern with predictive capacity is discernible. b) and c) show the nozzle drift for each of the 12 sequentially printed structures individually, while a) shows the integrated drift over the entire duration of the experiment. Reprinted from [6].

Results and Analysis

Figure 4.12b presents the measured nozzle drift as a function of the distance moved along each axis. Each dataset corresponds to one of the 12 structures, and the different jog movements are visually differentiated by decreasing color saturation in the same order they are introduced above. The axes are color-coded. The results indicate that reducing the total movement distance does not influence nozzle drift; instead, the displacement is condensed into a shorter movement range. This suggests that nozzle drift is primarily time-dependent rather than distance-dependent.

This hypothesis is further supported by Fig. 4.12c, which plots nozzle drift in the x-direction as a function of elapsed time. Each dataset corresponds to one of the 12 structures, with the same color and saturation-coding as above. The data confirms that nozzle drift is a continuous process over time, but no clear pattern or periodicity is observed. Additionally, the type of jog movement does not appear to influence the drift behavior.

Figure 4.12a shows the cumulative nozzle drift over time. Since all 12 structures were printed consecutively, nozzle drift can be integrated over all of them providing a long-term evaluation of the process. There is no apparent correlation between jog movement type (indicated by color saturation) and drift further reinforcing the conclusion that drift is primarily time-driven rather than movement-dependent. However, no clear regularity or predictive pattern for nozzle drift can be discerned.

One possible explanation for this behavior is a sensitivity of the system to minor fluctuations in ambient temperature. While the UPD printer is situated in an air-conditioned cleanroom environment, minor temperature changes can occur depending on the equipment running and the number of people present. However, we are currently unable to conclusively determine the root cause of nozzle drift.

This study has experimentally confirmed the existence of nozzle drift in long UPD print jobs. The results demonstrate that nozzle drift is primarily a function of time rather than motion. As a result, nozzle drift is unlikely to be a significant issue for short-duration print jobs. However, for long-duration print jobs where high accuracy is required, implementing a manual realignment step may be necessary to ensure precision.

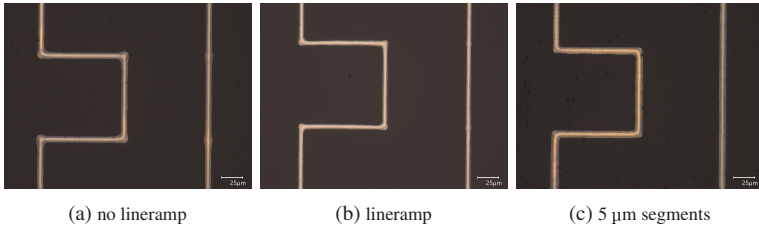


Figure 4.13: Printing the same structure with and without lineramp. The Ω -shaped structure has 100 μm long segments and the vertical line is printed with multiple 100 μm long segments which end at the corners of the adjacent Ω -structure. The rightmost structure is printed without lineramp but by splitting all lines in 5 μm long segments, which also significantly increases line uniformity. Reprinted from [6].

4.2.7 Line Uniformity

Depending on the application, it is crucial that the printed lines are as uniform as possible. When structures are printed with multiple segments, the connecting points of those segments typically show the largest deviation from a uniform line. Since conformal prints are composed of many segments, special care needs to be taken to achieve uniform lines. We have analyzed three different approaches within this work: Standard printing with no special care, see figure 4.13a, printing with the lineramp command as discussed in section 2.3.2, see figure 4.13b, and dissecting every line in 5 μm long segments, see figure 4.13c. The latter approach acknowledges that it is impossible to completely eliminate bulges at the end of a segment and places them close enough together that the entire line is made of bulges and hence uniform.

We measured the line widths as well as the bulges at the connecting points of the individual segments of the vertical line to analyze the uniformity of the lines. When no special care is taken, i.e. no lineramp is used, the line width can increase by up to 40 % at segment ends. Utilizing lineramp decreases this value significantly to 15 %. Splitting the line in many 5 μm long segments further improves uniformity and the maximum deviation from the average line thickness we found was only 7 %. But this increased uniformity comes at the cost of a wider line. We partially compensated for this by lowering the printing pressure from 9000 mbar to 6500 mbar but still found the line width to increase from 6.8 μm to 8 μm .

In conclusion, we suggest using lineramp for thinner lines and for a potentially shorter printing time. If line uniformity is of utmost importance, we recommend splitting all lines in 5 μm long segments. This approach may become obsolete if a printer is equipped with a motion controller and multiple segments can be printed without stopping the movement in between.

4.2.8 Summary on UPD Process Considerations and Improvements

In Chapter 3.1, we observed that ramp-based interconnects are attractive when switching from bond-wire-based packages to printed interconnects, as they require minimal design modifications. Even planar interconnects often involve some degree of surface steps, since achieving a perfectly level gap or cavity fill is extremely challenging. As a result, the UPD printer must be capable of printing onto non-planar surfaces.

Previous approaches typically relied heavily on user intervention, requiring the operator to manually teach the surface. The work presented in this chapter significantly reduces the labor involved and enables printing on nearly arbitrary topographies. Our method is based on surface measurement and automatically projects print paths onto it, eliminating the manual teaching step.

We have highlighted the importance of alignment for conformal UPD printing and examined how different projection methods influence printing time. Additionally, we introduced the concept of nozzle drift and demonstrated how it can affect print accuracy in long-duration jobs. Furthermore, we have shown how the uniformity of printed lines can be improved.

In summary, we have significantly extended the capabilities of the UPD printing technology and developed the necessary tools for its application in mmW electronics. The conformal printing process we developed is summarized in the flowchart shown in Figure 4.7.

5 Isolated Component Demonstrators

Before implementing printed interconnects at the system level, it is prudent to thoroughly investigate their performance. A logical first step in this process is to measure the performance of printed transmission lines, providing a fundamental understanding of the losses to be expected.

This chapter begins with an AJ-printed transmission line and a detailed analysis of the origins of the measured losses. The results demonstrate excellent performance in the D-band.

Subsequently, the two interconnect topographies introduced in Chapter 3.1 will be examined. Section 5.2 focuses on the ramp-based topography, presenting interconnects fabricated using both UPD and AJ printing. Section 5.3 follows with an investigation of cavity-based interconnects produced through both printing technologies.

Each interconnect section begins with an overview of the required technologies and the processes developed for assembling the demonstrators. They provide a comprehensive understanding of the manufacturing techniques necessary for printed interconnects. Since a multitude of challenges had to be solved, the approaches presented in those sections were crucial to the success of this work.

5.1 Aerosol Jet Printed Transmission Lines

The first step in evaluating the performance of printing processes for mmW applications should be to measure the performance of printed transmission lines in the target frequency range. Therefore, this section presents AJ printed microstrip (MS) transmission lines on a polyimide (PI) substrate. They have been characterized in D-Band using a Thru-Reflect-Line (TRL) calibration

to de-embed the probe pad to MS transition. The process optimizations and solutions developed for printing mmW transition lines will be presented in this section. It also provides a detailed analysis of the physical properties of the printed line including its profile, conductivity, and roughness which are used to discuss the origin of the measured losses.

The work presented in chapter 5.1 has been previously published in [15] in the Proceedings of the 51st European Microwave Conference (EuMC). Text, structure, images, tables, presentation, and content can show modifications here. The design, manufacturing, and measurements were conducted by Georg Gramlich. Joachim Hebel and Christian Bohn provided feedback on the simulations and measurements. They also introduced the author to probe-based RF measurements. Uli Lemmer and Thomas Zwick provided guidance and feedback on the original publication.

5.1.1 Design

The stackup used in this investigation consists of a solid brass ground plane, a 100 μm PI dielectric layer, and a 7.7 μm -thick printed silver top layer. The transmission line was designed for a standard 50 Ω impedance, corresponding to a width of 220 μm in this configuration. The probe pad employs a vialess ground transition due to the limitations of AJ printing, which does not support via fabrication without integrating additional processes. To maximize the bandwidth of the transition, butterfly-shaped ground pads were implemented.

The dimensions of the probe pad and the CPW to MS transition were optimized to minimize reflection loss when used with GGB Picoprobes. During this optimization, a minimum gap width of 20 μm was maintained to prevent short circuits caused by overspray during AJ printing. The resulting design of the probe pad and the CPW-to-MS transition is shown in Fig. 5.1. A continuous ground plane was employed in the design, and all simulations were conducted using CST Microwave Studio.

The research question in this section is to determine the losses per millimeter of an AJ printed transmission line. Therefore, a custom multilayer TRL (mTRL) calibration was printed, allowing to remove the influence of the probe contacts and of the CPW-to-MS transition from the measurements. The mTRL calibration includes an open, a thru, and three lines with lengths of 289 μm ,

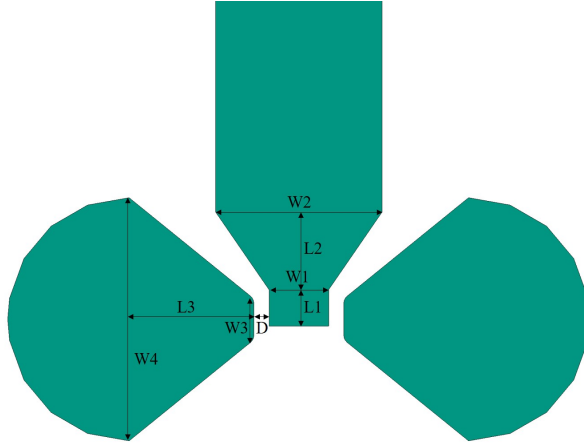


Figure 5.1: Structure of the probe pad and the CPW to MS transition. Dimensions: $W1 = 78.8 \mu\text{m}$, $W2 = 220 \mu\text{m}$, $W3 = 53 \mu\text{m}$, $W4 = 321 \mu\text{m}$, $L1 = 48 \mu\text{m}$, $L2 = 102.5 \mu\text{m}$, $L3 = 166 \mu\text{m}$, $D = 20 \mu\text{m}$. Reprinted from [15].

$316 \mu\text{m}$, and $359 \mu\text{m}$. To ensure monomodal propagation at its end, as required for accurate mTRL calculations [DJM02, WMD91], the launcher was designed to be $1000 \mu\text{m}$ long. Additionally, a 1 mm -long line was fabricated to accurately measure losses per millimeter, avoiding potential errors caused by upscaling measurement imprecision.

5.1.2 Manufacturing

A 1 mm -thick brass sheet was used as the ground plane. The sheet was cut into $20 \text{ mm} \times 20 \text{ mm}$ pieces, onto which a thin layer of Duralco 4460 glue (purchased from Polytec) was spin-coated. This adhesive securely bonded a $100 \mu\text{m}$ -thick PI film to the brass sheet. Duralco 4460 was specifically chosen for its high-temperature stability (315°C), ensuring that thermal sintering does not degrade the adhesive and that it does not limit the temperature tolerance of the final device.

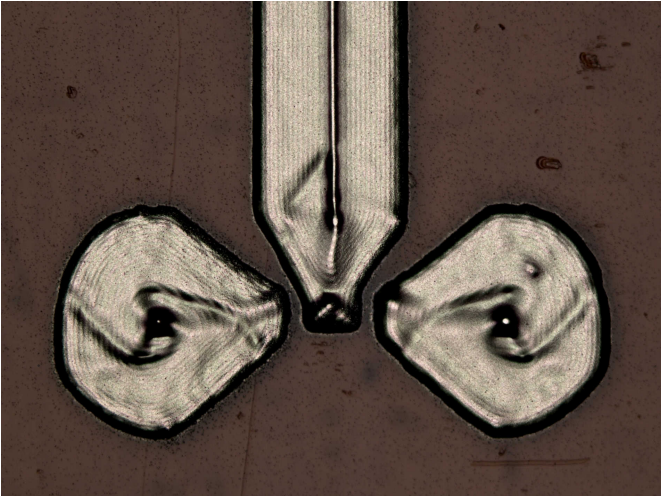


Figure 5.2: Aerosol Jet printed probe pad with broadband vialess ground transitions for D-Band. Reprinted from [15].

The conductive top layer was fabricated using the Optomec AJ 5X aerosol jet printer in a cleanroom environment. Since only planar structures were required, the printer was configured in a 3-axis setup. We selected JS-A221AE silver nanoparticle ink by Novacentrix due to its ability to achieve fine features, high aspect ratios, and low surface roughness, while also being water-based. To ensure homogenous surfaces, the ink was diluted in a 1:2 ratio by volume with deionized water. The bubbler was filled with DI water, and no gas bypass was used. All printing and printing path design parameters are detailed in Table 5.1.

To minimize disturbances in regions with the highest current and field densities—such as the borders of the printed structures—a perimeter fill pattern was used. Additionally, the starting point of the printing pattern was placed far from the probe contacts to avoid irregularities. The printing speed was deliberately kept very low due to the small feature sizes and sharp edges required. Speeds exceeding 1 mm/s noticeably reduced geometric precision due to mass inertia effects.

Substrate adhesion on the PI film was found poor without pretreatment. Activation in an oxygen plasma for three minutes significantly improved adhesion and has been implemented as pretreatment step. Another challenge encountered

Table 5.1: Aerosol jet printing parameters for the microstrip line on polyimide. Reprinted from [15].

Sheath	18 SCCM
Atomizer	9 SCCM
UA power	350 mA
UA temperature	26 °C
Ink volume	3 mL
Printing speed	0.5 mm/s
Line width	17 μm
Line pitch	9 μm

during process development was crack formation in the printed structures, attributed to the high thickness (7.7 μm) resulting from the slow printing speed. This issue was resolved by implementing flash sintering instead of conventional thermal sintering. The samples were processed directly after printing in a Novacentrix PulseForge 1200 system without prior drying. The theoretical foundation for this behavior has been presented in chapter 4.1.4.

5.1.3 Measurement Equipment and Procedures

All RF measurements were conducted using a Keysight PNA-X network analyzer equipped with OML frequency extenders for the 110 - 170 GHz range and Model 170 Picoprobes by GGB. The Model 170 Picoprobes were chosen for their individually suspended contacts, which can compensate for a minor unevenness arising from the manufacturing process.

A two-tier calibration approach was employed to evaluate the transmission line parameters: an initial calibration on a CS-15 impedance standard substrate for on-wafer measurements, followed by the mTRL calibration algorithm as a second tier. The second tier calibration allowed to remove the influence of the probe contact and of the CPW-to-MS transition from the measurements.

The surface roughness of the printed transmission lines was measured using a Bruker Contour GT-K WLI with a 20x magnification lens. Surface roughness is a critical parameter at mmW frequencies, as it directly contributes to

losses [GH15]. The microstrip line profile was also extracted from the WLI measurements.

The high thickness of the metal film produced by the printing process rendered standard four-point probe sheet resistance measurements impractical. A thick film results in very low measured resistivity, with the measurement accuracy severely impacted by noise. To address this, a thin line with four contact pads was printed specifically for a four-point measurement. This approach increases the measured resistivity while eliminating the influence of contact resistance and measurement cable resistance. The conductor cross-section, required for calculating the specific resistivity, was measured using a WLI.

5.1.4 Results and Discussion

In this chapter, the primary focus is on estimating the performance of the printed microstrip line. Insertion loss is the most relevant parameter derived from the RF measurements. Figure 5.3 shows the measured insertion loss of the printed 1 mm line prior to the second-tier calibration. That means that the measurement includes the actual 1 mm line segment, as well as the probe contact, the CPW-to-MS transition and the 1 mm long launcher at both sides. Contrary to the typical behavior of a transmission line, the insertion loss decreases with increased frequency. This ostensible anomaly can be attributed to the influence of the probe pads, which feature a vialess CPW-to-microstrip transition. This transition relies on capacitive coupling, which improves at higher frequencies and compensates for the increased line loss.

The influence of the CPW-to-MS transition and the line loss can be separated with a second-tier mTRL calibration. After this calibration, the reference plane is located at the midpoint of the thru standard, corresponding to the endpoints of the measured transmission line. Since the line length was designed to be 1 mm, the insertion loss after mTRL calibration directly represents the line loss per millimeter. It is shown in Fig. 5.4.

Comparing the measurements before and after second tier calibration allows estimating the performance of the CPW-to-MS transition. The insertion loss for a single transition is approximately 0.5 dB at 110 GHz. As expected, the performance improves for higher frequencies.

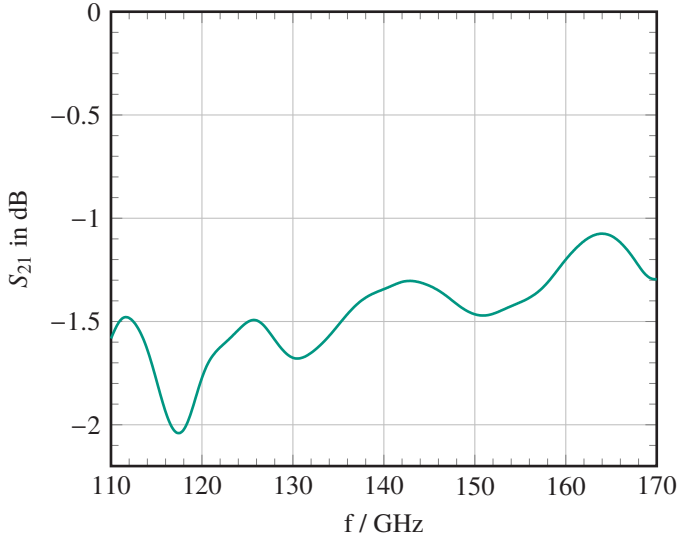


Figure 5.3: Insertion loss of a 1 mm long AJ printed microstrip line without second tier TRL calibration. Reprinted from [15].

Figure 5.4 shows a transmission line loss of 0.12 dB/mm at 110 GHz, and a maximum loss of 0.36 dB/mm in D-band for the AJ printed microstrip line. Understanding the loss mechanisms behind the measurement is crucial for future optimizations. They can be investigated through simulations, where different loss mechanisms are successively introduced. The primary contributors are dielectric losses in the substrate, ohmic losses in the conductors, and conductor surface roughness. In this work, the top and bottom layers must be analyzed separately, as they differ in material composition.

To accurately model the transmission line geometry, the printed MS line was measured with a WLI. The cross-sectional profile, shown in Fig. 5.5, shows a thickness of 7.7 μm and slightly inclined sidewalls. Defining the start and endpoint of the line at half the thickness gives a line width of 210 μm .

A series of simulations was conducted, incorporating the measured line width and sidewall slope. These simulations are shown in Fig. 5.4 alongside the measured data. The pale purple baseline is a lossless simulation and an increased color saturation indicates successively introduced loss mechanisms.

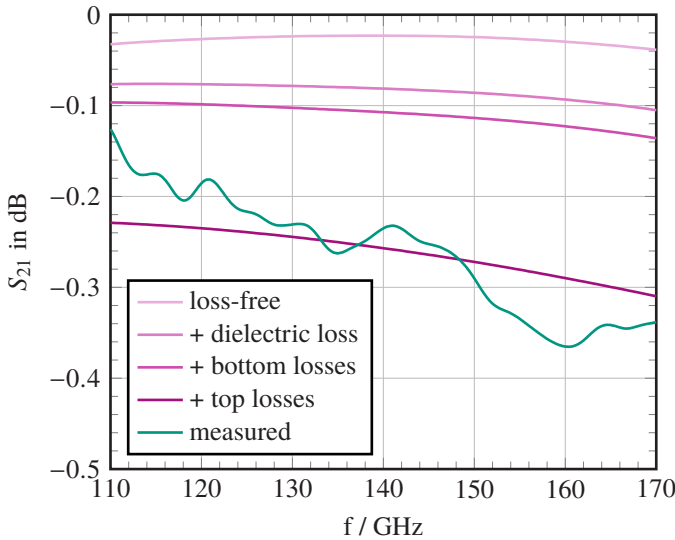


Figure 5.4: Insertion loss of a 1 mm long printed microstrip line after second tier calibration (green) and simulation of such a line with successively introduced losses (purple). Reprinted from [15].

The lossless simulation accounts only for radiation losses. In the next step, dielectric losses were introduced, resulting in an additional 0.06 dB loss at the center frequency of 140 GHz. Subsequently, bottom conductor losses were included, modeled with a conductivity of $\sigma = 1.59 \times 10^7$ S/m and a measured surface roughness of $R_q = 135$ nm. These losses contributed only 0.03 dB at the center frequency. Finally, top conductor losses, attributed to the printed silver, were introduced. They were the most significant, accounting for 0.15 dB at 140 GHz.

Supplementary simulations indicated that the effect of surface roughness on the top conductor are negligible, as the measured roughness was $R_q = 91$ nm, which is 2-3 times better than typical laminated substrates used for RF applications. However, the conductivity of the printed silver was measured to be 9.593×10^5 S/m. This is only 1/66 the conductivity of bulk silver, making it the primary contributor to losses. Therefore, any attempt to reduce the losses must focus on improving the conductivity of printed silver.

Table 5.2 provides a comparison of the AJ printed microstrip line with values reported in the literature, and with simulations. The performance we measured closely aligns with that of AJ printed MS lines on liquid crystal polymer (LCP) substrates reported in [CCW⁺14a].

When compared to a microstrip line on LCP fabricated using a lithographic process [KUP13], our results demonstrate that aerosol jet printing is a viable competitor to lithography in the D-band. For additional context, the table also includes simulated losses for a microstrip line on PI made of copper (Cu) with a surface roughness of $R_q = 300$ nm, a common value for RF substrates.

5.1.5 Summary on Aerosol Jet Printed Transmission Lines

This subchapter analyzed the performance of AJ printed transmission lines. It included a detailed analysis of the origins of the measured losses, providing insight for possible optimizations. To this end, microstrip transmission lines and probe pads with a vialess CPW-to-MS transition were printed on a PI substrate. By applying an mTRL calibration, we de-embedded the probe contact and

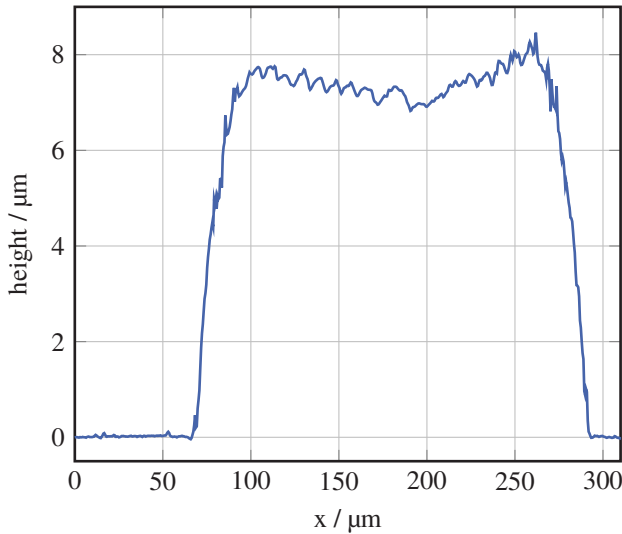


Figure 5.5: Profile of a printed microstrip line, measured with a WLI. Reprinted from [15].

Table 5.2: Comparison of microstrip line losses in D-Band reported for different technologies. Reprinted from [15].

Ref.	Process	min loss in dB/mm	max loss in dB/mm
This	AJ on PI	0.12	0.36
[CCW+ 14a]	AJ on LCP	0.35	0.51
[KUP13]	Lithography on LCP	0.1775	0.331
	Simulated AJ on PI	0.23	0.31
	Simulated Cu on PI	0.14	0.21

the probe pad to microstrip transition. This enabled us to calculate the pure transmission line loss. They were measured to be as low as 0.12 dB/mm at 110 GHz, with a maximum loss of 0.36 dB/mm observed in D-band.

A comprehensive characterization of the printed lines was conducted, including assessments of surface roughness, and conductivity. Using this data in simulations, we identified the resistivity of the printed silver as the primary contributor to the line losses.

The findings in this chapter clearly show that AJ printing is suitable for mmW applications since the losses of printed transmission lines are sufficiently low. They also indicate room for improvement by utilizing inks or sintering processes that yield a higher conductivity.

5.2 Ramp-Based Interconnects

As discussed in chapter 3.1, ramp-based interconnects come with the great advantage of being compatible with well established manufacturing techniques. Additionally, they allow an easy transition from bond wires to printed interconnects for improved performance without the need for major design changes. Therefore, chapter 5.2 investigates the performance of ramp-based interconnects, both manufactured by AJ and UPD printing.

5.2.1 Technology Development

Some process steps in the manufacturing of ramp-based interconnects are independent of the printing technology utilized. Those steps will be presented within this section. The most important step certainly is the creation of the ramp to be printed on. The technological development for this step includes the actual dispensing of the ramp, but also the selection of the ramp material, as well as the pre- and post-treatment.

The ramps for printed interconnects should be easy and quick to manufacture for them not to introduce unreasonable cost in the manufacturing process. They also have to avoid any gaps between the ramp and the conductors to allow the creation of continuous printed structure. Therefore, it is not possible to use premade ramps and simply place them next to the MMIC. This approach would always cause a small gap between the components which would lead to discontinuities in the printed silver and hence to poor electrical performance.

Dispensing ramps directly onto the MMICs and PCBs to be connected, is an easy and fast way to create ramps that avoid gaps between the components they connect. Dispensing can be done with standard equipment. It is even possible to equip the UPD printer with an adapter for standard dispensing cartridges and nozzles. This allows to benefit from the precision of the printer while using off-the-shelf materials and therefore reduce costs.

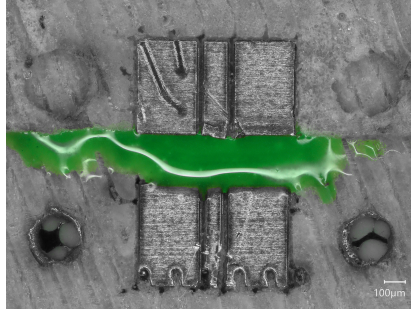
As ramp materials, adhesives are a good choice. They are tailored to dispensing techniques, show good adhesion to the commonly used materials and can be cured with relative ease. Multiple technical adhesives have been analyzed for their suitability for dispensed ramps. They vary in their curing method (thermal vs. UV) and their viscosity. All of them are optically transparent and can be dispensed with standard equipment. The following paragraphs will present an analysis of desirable and problematic properties technical adhesives can exhibit for ramp dispensing. To illustrate those properties, all adhesives have been mixed with green pigments for better visibility. They have then been used to create a ramp between two pieces of Rogers CLTE-MW PCB placed on top of each other. Each of those PCBs features a CPW transmission line. The setup is the same as in chapter 5.2.2 where the performance of an AJ printed ramp-based interconnect has been investigated. To make the behavior of the adhesive more easily visible, all images of the dispensed ramps have been post-processed so

that only the green color of the glue remains saturated whereas all other colors have been converted to grayscale. Those photos are shown in Fig. 5.6.

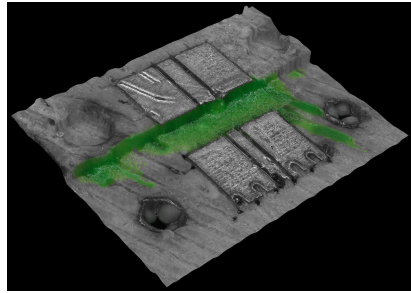
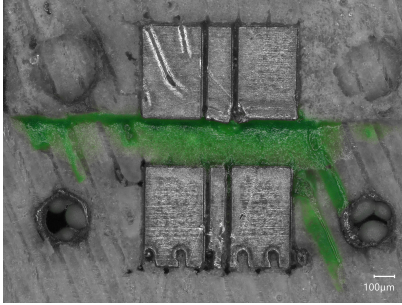
One of the most important requirements for the ramp material is its temperature stability. It needs to withstand temperatures up to 250 °C for 10 min to allow thermal sintering of the printed interconnects. The continuous operating temperature however is allowed to be significantly lower. All tested adhesives satisfy this criterion.

Another important factor to consider is the viscosity of the adhesive. A low viscosity comes with the advantage of easy dispensing and compatibility with AJ printing as an alternative dispensing technology. Therefore, the UV curable adhesive NEA 121 by Norland has been tested for its performance as ramp material. While dispensing is possible with both technologies, it comes with a severe downside: Due to the low viscosity, it can quickly spread over large surfaces. Especially the copper cladding of a Rogers substrate with a typical surface roughness of 300 nm is often covered by a thin adhesive layer. This thin layer acts as an electric insulator severely degrading the performance of printed interconnects. A possible remedy is the introduction of a glue scrubbing step after ramp dispensing. This step is enabled by the ProtoLaser R4 by LPKF which is set to low power and ablates material from the CPW segments. It effectively removes the glue layer and the topmost part of the copper cladding. This approach has successfully been utilized for the AJ printed ramp based interconnects presented in section 5.2.2. Fig. 5.9 shows the signs of the glue scrubbing process: Vertical lines caused by the laser are visible on the copper left and right to the printed interconnect.

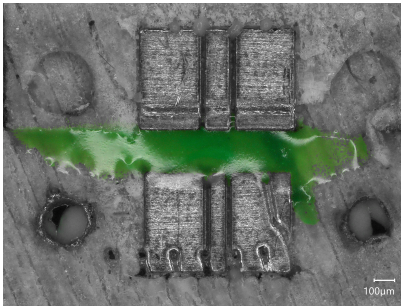
While glue scrubbing solves the issue of glue spreading over conductors, it also introduces an additional processing step. Therefore, it is desirable to find an alternative adhesive that does not form an insulating layer from the start. The effects that caused the problem is the contact angle of the adhesive on the substrate material in combination with the low viscosity enabling fast spreading. Therefore, two approaches to mitigate the undesired spreading are possible: The contact angle can be tuned, or the viscosity can be increased to slow down the spreading process sufficiently so that the adhesive can be fully cured before it has spread. Tuning the contact angle is significantly more complicated since it depends on adhesive and substrate and needs to be adapted for every combination anew. Choosing an adhesive with a higher viscosity, however, presents a more versatile solution since it is mostly independent of the substrate.



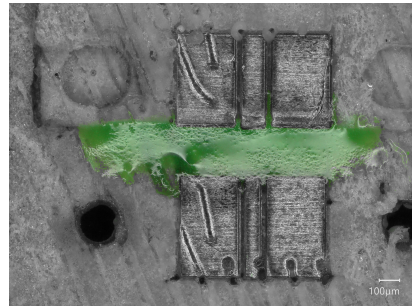
(a) Glue before curing (EP501 in this photo). A similar shape is seen for all adhesives tested before curing.



(b) EP501 after curing.



(c) NEA 121 after curing.



(d) NEA 123M after curing.

Figure 5.6: Investigation of multiple adhesives for ramp dispensing. All adhesives have been mixed with green pigments for better visibility. EP501 spreads widely during the thermal curing process while both UV curable adhesives maintain their shape. NEA 123M exhibits the best final shape since excessive spreading is reduced by the higher viscosity compared to NEA 121.

The thermally curing one-component epoxy adhesive EP501 by polytec has been chosen as a candidate. It has a viscosity of 13 000 cP and can withstand a short time operating temperature of up to 275 °C. It is cured for 10 min at 150 °C and compatible with standard dispensing equipment. As expected, it can be dispensed without undesired spreading as seen in Fig. 5.6a, which shows the dispensed ramp before curing. However, while the glue is heated up for curing, its viscosity decreases significantly before curing starts. This enables it once again to spread in an undesired way as seen in Fig. 5.6b, which shows the same ramp after curing. It can be seen that no ramp is present any more but that the adhesive has spread all over the substrate.

The problem of EP501 is the temporary low viscosity during thermal curing. Therefore, an alternative which does not exhibit this temporary low viscosity is required. It can be found by once again utilizing a UV curable adhesive: Norland offers a UV curable adhesive NEA 123M with a viscosity of 12 000-15 000 cP and a continuous operating temperature of 150 °C which also withstands the required temperature for sintering for a short time. Additionally, it comes with a latent heat catalyst, which allows to thermally cure it in places inaccessible to UV light. Fig. 5.6d shows a ramp dispensed with NEA 123M after curing. It is visible, that no excessive spreading took place and that the ramp exhibits the desired shape.

One final issue had to be resolved for the processes involving UPD printing. Printing onto a ramp requires a measurement of the surface topology. However, a white light interferometer requires light reflected from the surface into the lens. All previously investigated adhesives are optically transparent, however. Therefore, they are mixed with Alumina powder with 40 nm particle size in a weight ratio of 1 part alumina powder to 10 parts adhesive whenever optical measurements are necessary. Alumina withstands high temperatures and the small particles color the adhesive and reflect light back into the lens of a WLI. They therefore enable optical measurements of the ramp surface. This approach has been employed in section 5.2.3.

5.2.2 AJ Printed Ramp-Based Interconnects

This section investigates the performance of ramp-based AJ printed interconnects. To this end, two pieces of 80 µm thick Rogers CLTE-MW RF-PCBs

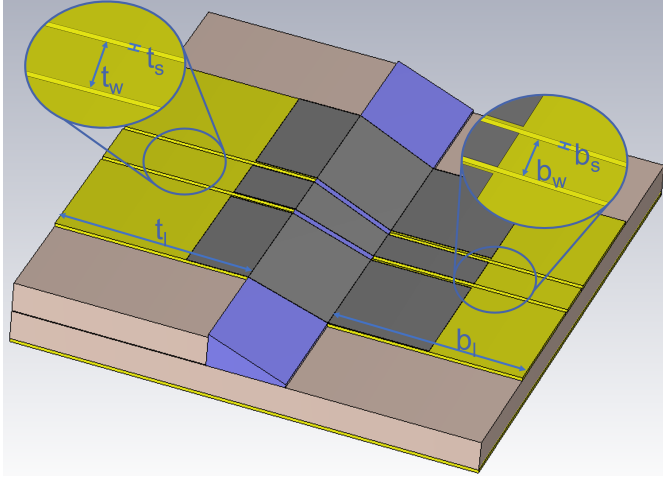


Figure 5.7: Simulation model of the printed interconnect. The dimensions are specified in Table 5.3. Figure reprinted from [17].

with $8\text{ }\mu\text{m}$ copper cladding have been placed on top of each other. Each of those PCBs features a CPW line. This substrate material has been chosen for its good performance at mmW frequencies. Its permittivity is approximately 2.96 at 10 GHz and the dissipation factor is 0.0015 at the same frequency.

A ramp has been dispensed onto the assembled PCBs, providing a smooth height transition between them. It has a length of $200\text{ }\mu\text{m}$ and a height of $80\text{ }\mu\text{m}$. In the last step, the actual interconnect has been AJ printed onto this assembly. This approach enables the precise characterization of the interconnect itself. A drawing of the assembly is shown in Figure 5.7. The interconnect has been characterized up to D-Band.

The work in chapter 5.2.2 have been previously published in [17] in the Proceedings of the 2025 German Microwave Conference (GeMiC). Text, structure, images, tables, presentation, and content can show modifications here. Design, simulation, manufacturing, measurement, and analysis was done by Georg Gramlich. Uli Lemmer, Thomas Zwick, and Akanksha Bhutani provided guidance and feedback to the original publication.

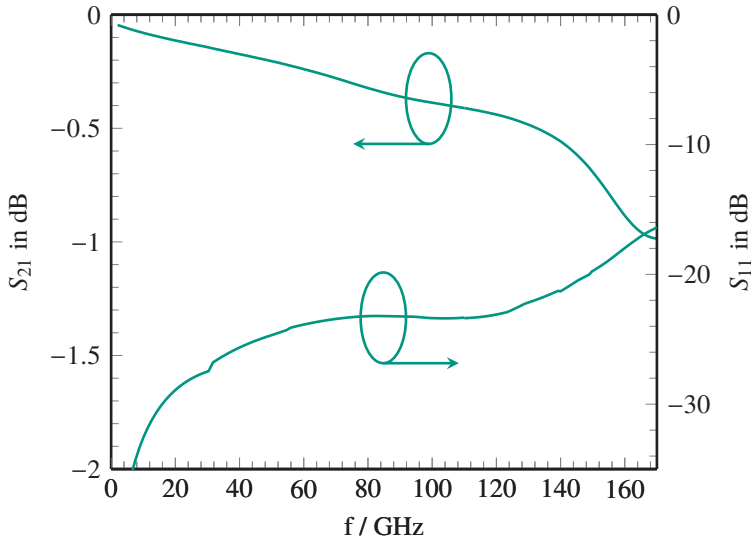


Figure 5.8: Initial CST simulation of the printed interconnect. Figure reprinted from [17].

5.2.2.1 Design

The assembly has been modeled in CST Microwave Studio as depicted in Figure 5.7. The figure shows, that both PCBs share the same ground plane and are attached to each other with a thin glue layer (blue). Since the effective substrate height changes for both transmission line segments, they were designed with slightly different dimensions, which results in a tapered interconnect (silver). This allows to keep the characteristic impedance constant at $50\ \Omega$ over the entire assembly. The dimensions of the CPW lines are shown in Table 5.3.

Figure 5.8 shows the insertion and reflection loss of the printed interconnect simulated in CST Microwave studio. The simulation includes dielectric and ohmic losses. Since the conductivity of printed silver is typically poor, a conductivity of 10 % of the bulk conductivity has been assumed (resulting in $6.3012 \times 10^6\ \text{S/m}$). The simulated insertion loss is below 1 dB from 2 - 170 GHz with an input matching better than 18 dB in this frequency range.

Table 5.3: Design parameters of the AJ printed ramp-based interconnect. The descriptors are shown in Figure 5.7. Reprinted from [17].

t_w	t_s	t_l	b_w	b_s	b_l
129 μm	20 μm	500 μm	86 μm	20 μm	500 μm

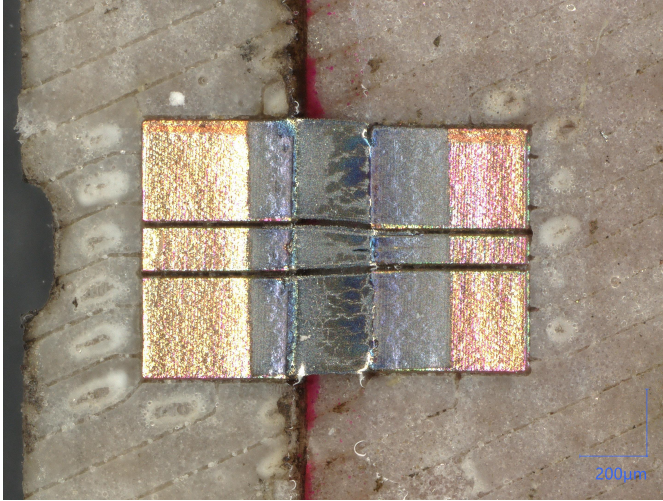


Figure 5.9: Photo of the AJ printed interconnect. Figure reprinted from [17].

5.2.2.2 Manufacturing

The two PCBs were fabricated using a ProtoLaser R4 by LPKF. This is a picosecond laser, capable of cold ablation which can manufacture structure sizes as small as 20 μm . Additionally, it is possible to cut the PCB in the same process as structuring the metal layer and thus to minimize misalignment errors. Due to the small size of the PCBs, they were attached to a glass carrier using Crystalbond 509 for processing. This prevented them from being drawn into the exhaust of the ProtoLaser by its air purge.

The assembly of the two PCBs was done using the advanced automatic sub-micron bonder FINEPLACER® femto 2 by *FINETECH*. A single-component epoxy adhesive, EP501 from Polytec, was automatically dispensed onto the bottom PCB, and the top PCB was precisely placed using the bonder's built-in pattern recognition software. Prior to creating the ramps, the substrates needed to be treated in an oxygen plasma for 3 min to improve wetting behavior on the PTFE based substrate. Afterward, the UV-curable adhesive NEA121 ($\epsilon_r = 3.0$ and $\tan \delta_e = 0.031$ at 110 GHz [19]) from Norland was dispensed to form the ramp structure. The low viscosity of this adhesive, combined with its contact angle on the copper layer of the CLTE-MW substrate, caused it to spread over the copper during dispensing. The resulting thin glue layer on the metal acted as an insulator, severely degrading the performance of any subsequently printed interconnects. To address this issue, the glue scrubbing process presented in chapter 5.2.1 was applied, which effectively solved the problem.

Once this assembly was prepared, the interconnects were printed. Since the minimum gap size from the simulation was 20 μm (see Table 5.3), a 100 μm nozzle, and the ultrasonic atomizer were employed. It was loaded with 3 mL of JS-A221AE silver nanoparticle ink from Novacentrix, diluted with pure water at a 1:2 volume ratio. To prevent rapid ink drying, 5 vol% of triethylene glycol monomethyl ether (TGME) was added to the mixture.

The printing parameters for the AJ printer, along with the design parameters used for the printing paths, are summarized in Table 5.4. To mitigate material buildup at the start and end of the printed lines and to eliminate inconsistencies caused by the divert/boost shutter mechanism, SOTF with the mechanical shutter was used. This selection is based on the considerations discussed in chapter 4.1 and the debugged version of the SOTF algorithm presented there was employed.

Prior to printing, the substrates underwent oxygen plasma treatment for 3 min. Thermal sintering was performed on a preheated hotplate at 200 °C for 10 min directly after printing.

The final assembly can be seen in Figure 5.9. It shows that the alignment of both PCBs is excellent. It also shows that the AJ-printed interconnect exhibits the same taper as the CST design shown in Figure 5.7.

Table 5.4: Aerosol jet printing parameters. Table reprinted from [17].

Sheath	20 SCCM
Atomizer	5 SCCM
UA power	400 mA
UA temperature	24 °C
Ink volume	3 mL
Printing speed	2 mm/s
Line width	16 μm
Line pitch	10 μm

5.2.2.3 Results and Discussion

All D-Band measurements in this chapter were performed on a Keysight PNA-X with OML frequency extenders for 110 to 170 GHz and Model 170 Picoprobes by GGB. The setup was calibrated with an Line-Reflect-Reflect-Match (LRRM) calibration on a CS-15 impedance standard substrate for on-wafer measurements. Measurements from DC to 125 GHz were performed with Keysight N5295A frequency extender modules and Titan 110 probes by MPI. A Short-Open-Line-Thru (SOLT) calibration on a AC2-2 RF calibration substrate was used.

Figure 5.11 shows the measured insertion loss of the printed interconnect as a red curve. A deviation from the original CST simulation, represented by the dark green dashed curve, is evident. To investigate the source of this deviation, the actual dimensions of the fabricated interconnect and PCB were measured using a microscope and a WLI. Figure 5.10 shows the WLI measurement and Table 5.5 shows the deviation between target values and measured dimensions. An interesting observation from this comparison is, that the printing process (maximum deviation of 9 μm) is significantly more accurate than the PCB manufacturing process (maximum deviation 14 μm). The measurements were integrated into the simulation model, resulting in the blue dashed curve in Figure 5.11.

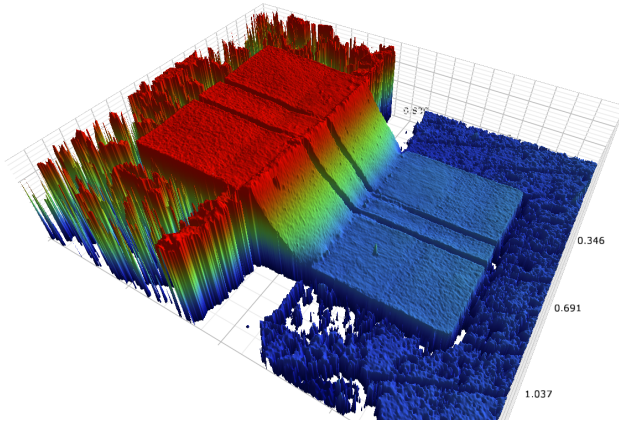


Figure 5.10: White light interferometer measurement of the printed interconnect. Reprinted from [17].

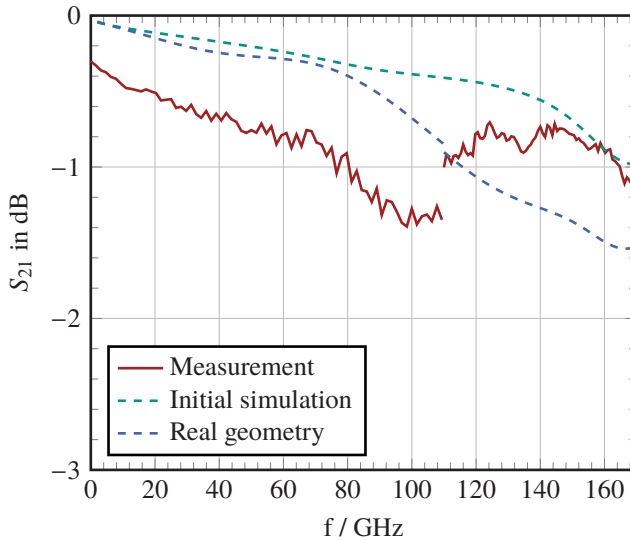


Figure 5.11: Insertion losses of the printed interconnect and both PCBs. Comparison of measurement and simulations. Incorporating the actually manufactured dimensions into the simulation yields good agreement between measurement and simulation. Figure reprinted from [17].

Table 5.5: Manufacturing tolerance in μm : Positive values mean a larger structure has been manufactured than designed and vice versa. w is the width of the CPW center conductor and s is the spacing between the CPW conductors. Table reprinted from [17].

Top				Bottom			
PCB		print		PCB		print	
w	s	w	s	w	s	w	s
+9 μm	-8 μm	-1 μm	0 μm	+14 μm	-8 μm	+9 μm	0 μm

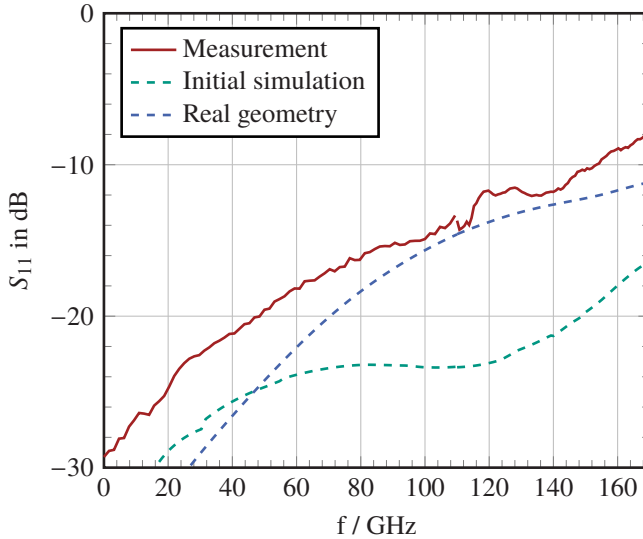


Figure 5.12: Matching of the printed interconnect. Comparison of measurement and simulations. Figure reprinted from [17].

Note that the measurement and simulations contain both the interconnect and the 0.5 mm long feeding lines at both ends. Consequently, the losses attributed solely to the interconnect are expected to be slightly lower than the measured and simulated values.

The input matching for the measurement and the simulations is presented in Figure 5.12. In this plot, good agreement is observed between the measurement and the simulations with the realized dimensions of the printed interconnect.

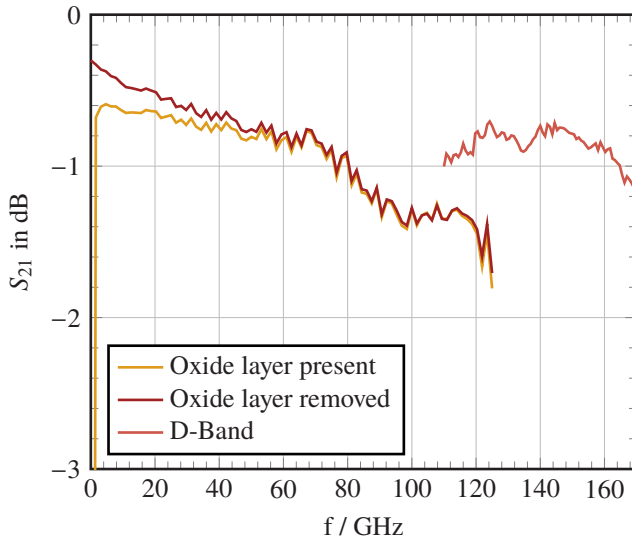


Figure 5.13: A thin oxide layer forms on the copper of the PCB forming a capacitor between probe tip and transmission line. This results in high losses and poor matching at low frequencies. Removing the copper layer by short immersion in a solution of citric acid drastically increases performance at low frequencies. The measurement in D-Band has been taken without any pre-treatment since the influence of the oxide layer is negligible at high frequencies.

An interesting observation can be made through the analysis of Fig. 5.13. The interconnect has originally been designed with a focus on D-Band. Therefore, the D-Band measurement has been taken first. The DC to 125 GHz measurements have been taken with a delay of 18 months. During this timeframe, the assembly was stored in air in a non-air-conditioned office in southern Germany. It was exposed to the typical swings in ambient temperature and humidity. This caused the copper cladding of the Rogers PCB to develop an oxide layer. Apparently this layer was thick enough that the RF probe could not penetrate it. Therefore, energy is coupled capacitively from the probe into the CPW line with no DC connection. This results in the poor performance at low frequencies observed in the orange curve in Fig. 5.13. Briefly immersing the assembly in citric acid or hydrochloric acid removes this oxide layer and yields the measurement shown

in red. Comparing both curves shows that the oxide layer becomes negligible above 50 GHz.

Another observation made from Fig. 5.13 is the poor alignment of the upper end of the DC-125 GHz and the lower end of the D-Band measurements. At 110 GHz the difference is 0.29 dB. This difference is most likely caused by the degradation of the printed interconnect over time since the lower band measurements were taken 18 months later. The difference increases up to 125 GHz, however, the measurement in the lower band is not reliable at those frequencies since the probes used are only qualified for operation to 110 GHz. While the observations presented are by no means a quantitative analysis, they indicate longevity of printed interconnects while also pointing to a performance degradation over time.

The printed interconnect exhibits a return loss of better than 10 dB from DC to 153 GHz and better than 8 dB in the entire measured range from DC to 170 GHz. Within the entire spectrum, the insertion loss of the assembly ranges between 0.31 dB and 1.43 dB, confirming the suitability of AJ printing for ultra-broadband interconnects from DC up to D-Band.

5.2.2.4 Summary on Aerosol Jet Printed Ramp-Based Interconnects

In this chapter, the performance of AJ printed ramp-based interconnects has been investigated. An assembly made of two RF-PCBs placed on top of each other was used. The ramp connecting them was 200 μm long and 80 μm high.

The realized AJ printed interconnect exhibits a return loss better than 10 dB from DC to 153 GHz and better than 8 dB up to 170 GHz. Within the entire measured frequency range, the insertion loss of the assembly is between 0.31 dB and 1.43 dB. It could be shown that AJ printing can produce interconnects with excellent performance and a large bandwidth from DC into D-Band.

5.2.3 UPD Printed Ramp-Based Interconnects

For the investigation of UPD printed ramp-based interconnects, a different approach has been chosen than for the AJ printed version in chapter 5.2.2. This is because at the time of the investigation, MMICs featuring a lossy thru line were available. Printing interconnects between a PCB and an MMIC allowed to get a better grasp on the performance in later systems, that would also incorporate MMICs.

This chapter describes the process of fabricating a printed interconnect between a RF-PCB and an optical modulator MMIC operating from DC to 110 GHz. The MMIC is a proprietary development of *SilOriX* and is produced on a 700 μm thick silicon wafer. The substrate used is *Rogers* RO3006, which has a relative permittivity of $\epsilon_r = 6.5$. The optical modulator MMIC has only been used as a lossy thru line in this work, since the main interest lies in characterizing the printed interconnect. The printed interconnect has been characterized up to 170 GHz. Additionally, this chapter contains an analysis of an unexpected, lower cutoff frequency of the printed interconnect which traces it back to the chip technology.

The work presented in chapter 5.2.3 have been published in [20]. Text, structure, images, tables, presentation, and content can show modifications here. Georg Gramlich proposed the topography of the assembly, conducted the RF measurements, and provided constant feedback. Manufacturing was carried out by Lilli Weiss during her bachelor's thesis under the supervision of Georg Gramlich and Luca Valenziano. Martin Roemhild and Holger Baur contributed to the development of the projection program, as described in chapter 4.2. Adrian Schwarzenberger, Carsten Eschenbaum, and Christian Koos provided the MMIC and its simulation model. Norbert Fruehauf, Thomas Zwick, and Akanksha Bhutani provided guidance and feedback on the original publication.

5.2.3.1 Design

The chosen topography for the MMIC-to-PCB interconnect is depicted in Figure 5.14. Due to the MMIC height of 700 μm , placing the MMIC on top of the PCB would have resulted in extremely long and hence lossy interconnects. Therefore, a combination of a cavity and a ramp is employed: The 250 μm thick

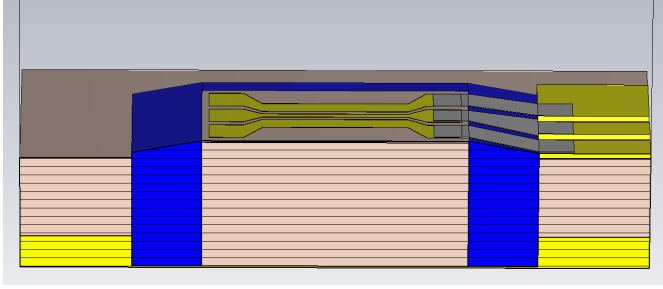


Figure 5.14: Cross-section of the interconnect topography. The MMIC is placed in a cavity in the PCB (beige) and submount (yellow). The remaining gap is then filled with a polymer (blue). Figure reprinted from [20]. © 2025 IEEE.

PCB is attached to a metal carrier extending the ground plane. Subsequently, a cavity is laser-processed into the PCB and the carrier. The MMIC is then placed in the cavity leaving a $100\text{ }\mu\text{m}$ height difference between the MMIC and PCB top. This allows a better comparison to chapter 5.2.2. The cross-section of this topography is shown in Figure 5.14.

The interconnect was then designed to maintain a $50\text{ }\Omega$ impedance over the gap. Therefore, it was necessary to include a jump in the line geometry at the end of the PCB. The resulting dimensions are labeled in Figure 5.15 and detailed in Table 5.6. The optimization and simulation of the interconnect was carried out in *CST Microwave Studio*. The return loss of the simulated interconnect is shown in Figure 5.18.

Table 5.6: Design parameters of the UPD printed ramp-based interconnect. The descriptors are shown in Figure 5.15.

t_w	t_s	b_{wg}	b_{sg}	b_w	b_s
$65\text{ }\mu\text{m}$	$30\text{ }\mu\text{m}$	$105\text{ }\mu\text{m}$	$25\text{ }\mu\text{m}$	$75\text{ }\mu\text{m}$	$40\text{ }\mu\text{m}$

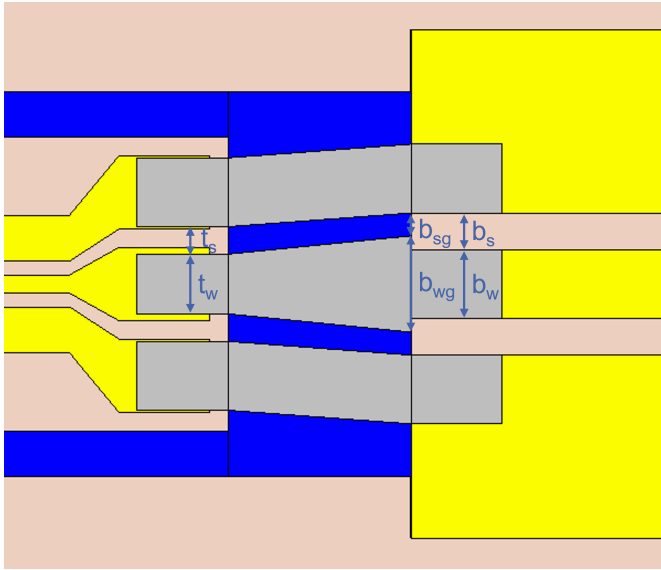


Figure 5.15: Dimensions of the printed interconnect.

5.2.3.2 Manufacturing

Manufacturing the package requires seven steps: attaching the PCB to the subcarrier, laser-structuring PCB and cavity, placing the MMIC in the cavity, dispensing the ramp, adhesive scrubbing as described in chapter 5.2.1, and finally printing the interconnect. These steps are detailed below.

First, the unstructured PCB is bonded to the subcarrier using AFT402 die attach foil from *Furukawa Electric*, chosen for its high conductivity and ability to ensure uniform attachment. Waviness caused by uneven adhesive layers is completely avoided. Structuring the PCB and cavity is done with a ProtoLaser R4 by *LPKF*. It can create the cavity and structure the PCB top layer at the same time, eliminating misalignment.

The MMIC must be placed into the cavity with high precision, requiring a top-to-top alignment. We achieved excellent alignment accuracy using the advanced automatic sub-micron bonder FINEPLACER® femto 2 by *FINETECH*. This

machine has multiple capabilities necessary for our process, including automatic dispensing of glue into the cavity (EP501 by *polytec*). Since the chips are picked from a vacuum release gel pak, an additional alignment step is required for top-to-top alignment: The residual adhesion of vacuum release gel paks can cause the chip to shift on the tool tip during pickup reducing alignment accuracy. To mitigate this problem, the MMIC is placed on a transfer station and picked up at a precisely controlled position. Afterward, the position of the MMIC on the tool tip is known, allowing for accurate placement in the cavity. Excellent parallelism between the MMIC and the PCB surface is achieved through the gimbal functionality of the tool tip.

Following MMIC placement, the ramp is dispensed using the UPD system. NEA 123M UV adhesive from *Norland* is used, mixed with 40 nm alumina powder in a 10:1 weight ratio. This adhesive was selected for its dual UV and thermal curing capabilities, essential for complete curing within the cavity's deep slots. Alumina particles have been added to the adhesive to improve visibility under a WLI, as explained in chapter 5.2.1. The high viscosity of NEA 123M (12000 - 15000 cP) decreases the spreading of the glue onto the PCB metal, it cannot be completely avoided, however. Therefore, the previously introduced glue scrubbing process has been employed.

Finally, the interconnect is printed onto the ramp using the UPD printer, equipped with a 5 μm nozzle. Since the interconnect had to be printed onto a ramp, our program for 3D printing path creation, presented in chapter 4.2, has been used. The fabricated interconnect can be seen in Fig. 5.16.

5.2.3.3 Results and Discussion

The RF measurements were conducted using a *Keysight* PNA-X network analyzer, complemented by *OML* frequency extension modules. *GGB* Picoprobes, with 100 μm pitch were employed for the measurements across the entire spectrum. For DC to 110 GHz, calibration was achieved through an LRRM procedure on a CS-5 impedance standard substrate (ISS). For measurements in D-Band, an LRRM calibration was performed on a CS-15 ISS.

In order to determine the loss stemming from a single printed interconnect, it was fabricated on only one side of the MMIC as seen in Figure 5.14. This design choice facilitated de-embedding the MMIC. The reflection loss at the

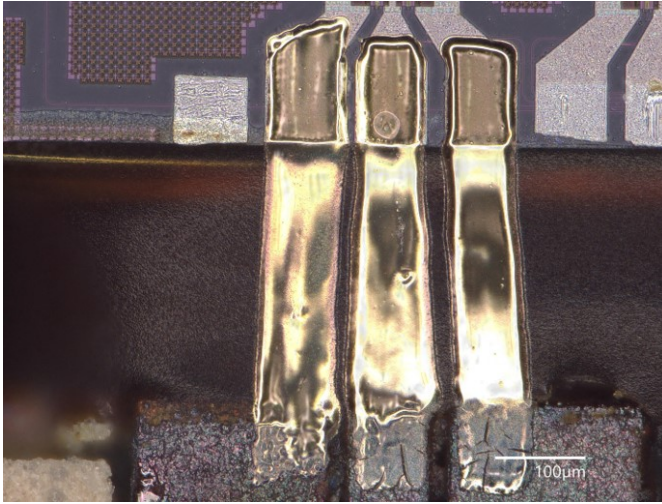


Figure 5.16: UPD printed interconnect between the PCB and an optical modulator MMIC. Figure reprinted from [20]. © 2025 IEEE.

side of the PCB of this assembly is presented in Fig. 5.17. It shows a return loss below 11.8 dB from 300 MHz to 170 GHz.

To evaluate the performance of the interconnect, the loss measured for the MMIC alone was removed from the loss measured for the entire assembly. This was achieved by calculating the decibel difference between the total assembly measurement and that of the MMIC alone. The result is shown in Figure 5.18, where the red curve represents the interconnect alone.

For a direct comparison with simulation outcomes, the assembly shown in Figure 5.14 was cut off immediately after the probe pads in CST. This new simulation considered only the components that remain after de-embedding: the CPW transmission line on the PCB, the printed interconnect, and the probe pads. The simulation results for this model are represented by the green curve in the plot. A notable discrepancy between simulation and measurement becomes apparent above 90 GHz, a difference possibly caused by manufacturing tolerances.

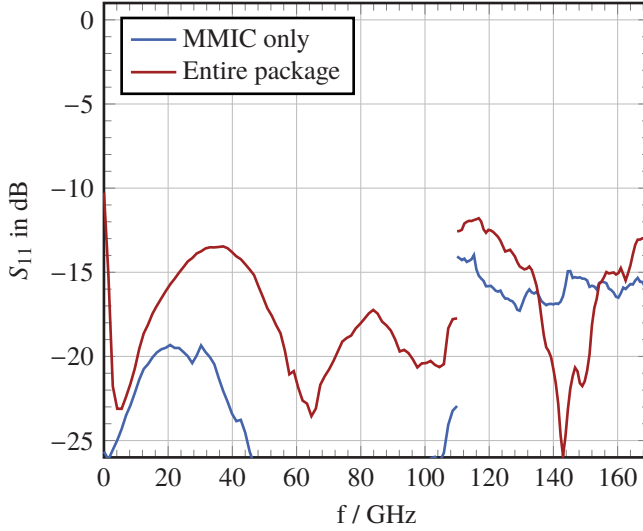


Figure 5.17: Return loss measurement of the MMIC alone and of the entire package. Figure reprinted from [20]. © 2025 IEEE.

To explore the origin of the difference between simulation and measurement, the actual geometrical dimensions of the printed interconnect were measured and incorporated into the simulation. This yields the orange curve in Figure 5.18. It shows a significantly improved agreement between measurement and simulation. Table 5.7 shows the deviation of the realized dimensions to the design dimensions. It is visible, that there is room for improvement. The UPD system is capable of printing with higher accuracy than achieved in this investigation and harvesting this potential could yield improved RF performance as indicated in Figure 5.18.

An intriguing aspect of the measured data is the observation that the package exhibits lower losses than the MMIC alone below 30 GHz, resulting in an ostensible gain in Fig. 5.18. This phenomenon, seemingly contravening physical principles, has been consistently observed across numerous measurements and is believed not to result from measurement inaccuracies alone. It is hypothesized that the coupling efficiency between the probe and the PCB is superior to that between the probe and the MMIC. This hypothesis is plausible given that the

Table 5.7: Manufacturing tolerance of the UPD printed interconnect. Positive values mean that a larger dimension was realized than designed and vice versa. The descriptors are shown in Figure 5.15.

t_w	t_s	b_{wg}	b_{sg}	b_w	b_s
+5 μm	-10 μm	-13 μm	0 μm	+5 μm	-7 μm

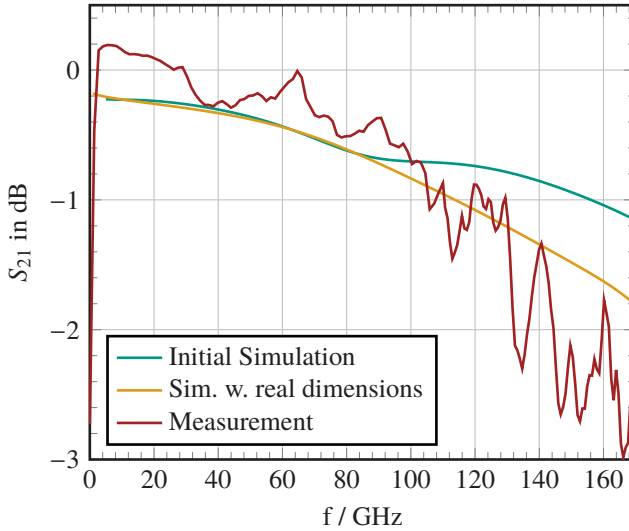


Figure 5.18: Loss of the printed interconnect. The measured loss has been calculated by subtracting the insertion loss measurement of the MMIC alone from that of the entire package. The values above zero for low frequencies can be explained by better coupling of the electromagnetic wave from the probe into the Rogers PCB (package) than into the MMIC due to the lower permittivity of the PCB. They are a systematic and unavoidable measurement error.

relative permittivity of the PCB ($\epsilon_r = 6.5$) is closer to that of air compared to the permittivity of silicon ($\epsilon_r = 11.9$) of the MMIC. The wave propagation occurs in air within the probe tips in the utilized air coplanar waveguide probe resulting in a less dramatic increase in permittivity and hence in better coupling when probing onto Rogers compared to probing the MMIC. If wave coupling into the PCB is more efficient than into the MMIC, an ostensible gain upon probing the PCB is anticipated. This perceived gain is eventually offset by the increasing losses at higher frequencies. It is important to understand that the “gain” observed in Figure 5.18 does not signify a physical gain; rather, it arises from the better coupling efficiency from the probe into the PCB than into the MMIC.

Another point of interest is, that the transmission of the package experiences a steep drop below 1.6 GHz. This behavior can be explained by the aluminum probe pads of the MMIC: Aluminum is prone to rapid oxidation upon exposure to air, resulting in the formation of a thin, non-conductive oxide layer. When silver is printed onto this oxide layer, a small capacitor is created. The influence of this unwanted capacitor diminishes at higher frequencies. It effectively acts as a high-pass filter.

Taking all the above considerations into account, it can be concluded that the UPD printed interconnect demonstrates a loss of less than 1 dB across the frequency range from 1.6 GHz to 110 GHz, with the input matching exceeding 13 dB within this spectrum. Beyond 110 GHz, the losses increase significantly, reaching a maximum of 3 dB at 165 GHz, while the reflection loss remains better than 12 dB.

5.2.3.4 Summary on UPD Printed Ramp-Based Interconnects

This chapter explored the performance of UPD printed ramp-based interconnects. A more complex package involving a submount, a cavity, an MMIC and Rogers PCB was created. The interconnect was printed between a CPW segment on the PCB and the MMIC.

The insertion loss of the interconnect alone was determined and found to be below 1 dB from 1.6 GHz to 110 GHz. The reflection loss was better than 13 dB within this range. Additionally, the interconnect was characterized up to 170 GHz, where it exhibits significantly higher losses, up to 3 dB. Below

1.6 GHz, the interconnect demonstrates high-pass filter characteristics, caused by an oxide layer forming on the aluminum probe pads of the MMIC.

The interconnect presented in this chapter shows good performance in the target frequency range of up to 110 GHz. An increased operational bandwidth could likely be achieved by an improved system design but was not required here, because the maximum operating frequency of the employed MMIC was 110 GHz.

5.3 Planar Interconnects

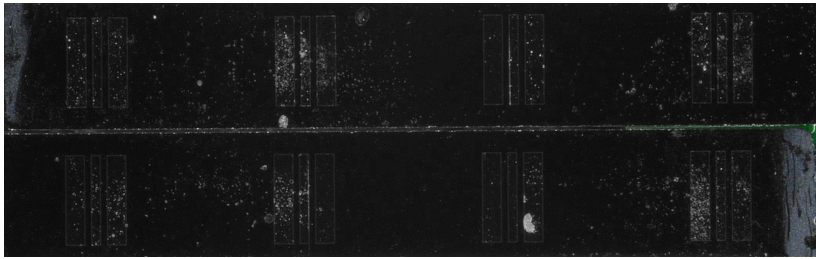
As discussed in chapter 3.1, planar interconnects promise lower losses due to the intrinsically shorter interconnect length. They also enable better thermal management for active MMICs when a submount is used. Therefore, chapter 5.3 investigates the performance of planar interconnects, both manufactured by AJ and UPD printing.

Unlike the chapter on ramp-based interconnects, the same overall assembly has been chosen. The only difference is the printing system that has been employed for the interconnect. Therefore, this chapter starts by presenting the technology developed for planar interconnects. Then, the demonstrator design and the manufacturing of the demonstrator system except for the printing step will be detailed. Subsequently, the manufacturing, as well as the measurement results and their discussion will be detailed separately for the AJ and UPD printed interconnects.

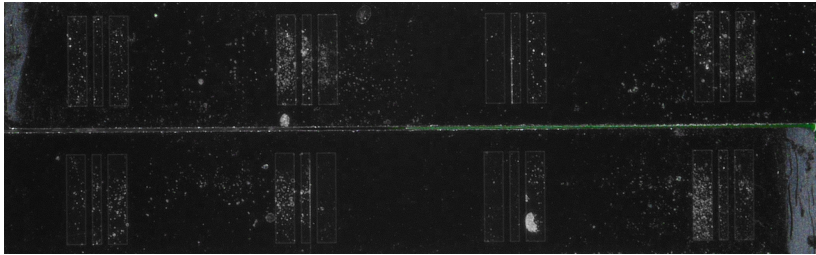
The contents of chapter 5.3 have previously been published in [16] and [18]. The contents of [16] have been published in the Proceedings of the 52nd European Microwave Conference (EuMC). Text, structure, images, tables, presentation, and content can show modifications, restructuring, and extensions here. The technology development described in chapter 5.3.1 was conducted by Georg Gramlich and has not been previously published. He also performed the design, simulation, manufacturing, measurement, and analysis of the work presented in this chapter. Robert Huber contributed his expertise in AJ printing and served as an intellectual sparring partner. Martin Roemhild and Holger Baur provided their expertise in UPD printing. Norbert Fruehauf, Uli Lemmer, Akanksha Bhutani, and Thomas Zwick provided guidance and feedback on the original publications.

5.3.1 Technology Development

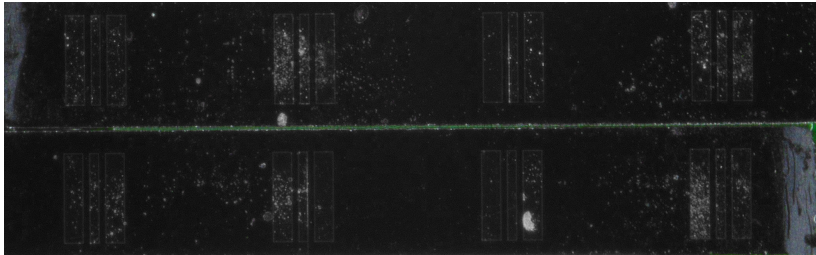
In this chapter the design possibilities for interconnects without ramps will be elaborated. Subsequently, the required processes to manufacture those interconnects will be presented.



(a) 2 min 20 s



(b) 10 min 20 s



(c) 30 min 0 s

Figure 5.19: Temporal propagation of the technical adhesive NEA 123M in the 11 μm wide gap between two MMICs. No pretreatment has been applied to the MMICs. The glue has been mixed with green color pigments and all other colors have been desaturated for improved visibility.

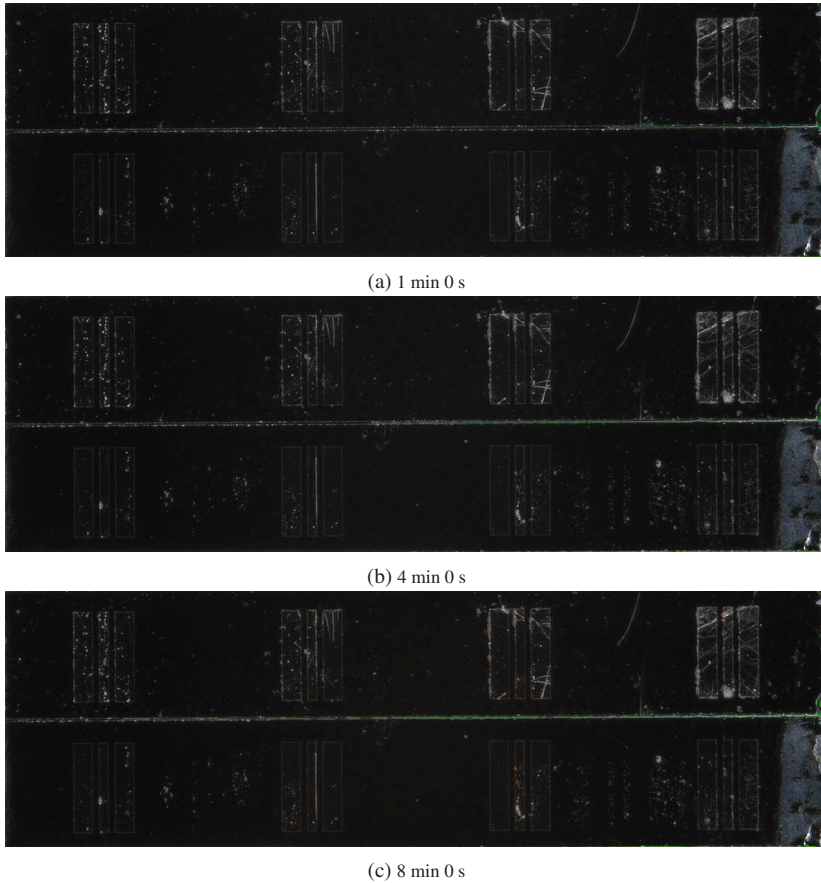


Figure 5.20: Temporal propagation of the technical adhesive NEA 123M in the 11 µm wide gap between two MMICs. The MMICs underwent a 3 min pretreatment in an oxygen plasma. The glue has been mixed with green color pigments and all other colors have been desaturated for improved visibility. Compared to the case with no pretreatment (see Fig 5.19), the glue spreads significantly faster.

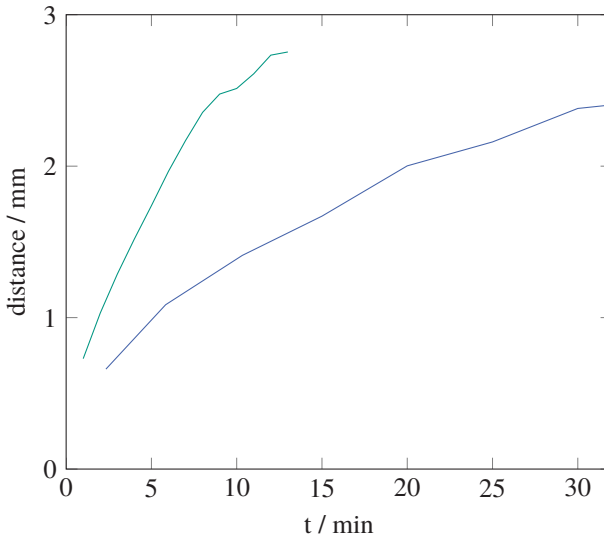


Figure 5.21: Propagation of glue in a $11\text{ }\mu\text{m}$ wide gap between two InP MMICs with and without oxygen plasma pretreatment. This plot corresponds to the images shown in Fig. 5.19 and 5.20. It can be seen that plasma pretreatment significantly reduces the required time to fill the $2754\text{ }\mu\text{m}$ long gap.

Planar interconnects require vertical alignment of the MMICs and PCBs to be connected. As discussed in chapter 3.1.2 this can either be achieved by placing everything on a precisely machined submount or by placing the MMIC in a cavity in the PCB. Both can be created either with CNC machining or by laser ablation. In this work, laser ablation with the ProtoLaser R4 by *LPKF* has been used for cavities (this chapter) and CNC machining for submounts (chapter 6).

The most important and most difficult challenge however is the filling of the gap between the two components. This gap with a filler is shown in Figures 3.2 and 3.3 in chapter 3.1. The smaller the gap, the shorter the interconnect will be and the lower the packaging losses will be. Therefore, it is desirable to keep the gap width in the range of tens of micrometers, preferably as small as $10\text{--}30\text{ }\mu\text{m}$ as we will see in chapters 5.3.4.2 and 5.3.5.2. The smallest standard dispenser needles have an inner diameter of $100\text{ }\mu\text{m}$ [Cor24], making them too large to dispense into the gaps. Utilizing specialized needles such as the $5\text{ }\mu\text{m}$ and $10\text{ }\mu\text{m}$

nozzles from XTPL could be a solution but would incur unreasonable expenses due to the high price for a single nozzle. Therefore, a different approach was developed within this work.

The novel approach suggested in this work is to utilize capillary action to fill the small gaps. If an adhesive with a sufficiently low viscosity is employed, and the contact angle between adhesive and MMIC is sufficiently low, a small droplet of glue can be dispensed to the end of the gap. It will then automatically be drawn into the gap by capillary action, see chapter 2.2.2. However, this process requires some attention: Fig. 5.19 shows two InP MMICs placed with a distance of 11 μm . A droplet of NEA 123M has been dispensed next to the gap. The glue has been mixed with green color pigments and all colors except green have been converted to grayscale in the images for better visibility of the adhesive. The figure shows a time series of the glue propagating into the gap. Even after 30 min, the 2754 μm long gap has not been filled completely. Therefore, it is desirable to speed up the propagation of the adhesive in the gap and ensure it propagates all the way through it. According to equation 2.77, the length of the gap filled can be increased by decreasing the contact angle, which in turn can be achieved by increasing the surface energy of the solid according to equation 2.76. Pretreatment in oxygen plasma increases the surface energy and is expected to increase the length through which the liquid propagates as well as the speed at which it does so. Fig. 5.20 shows the time series if the MMICs undergo an oxygen plasma pretreatment for 3 min prior to dispensing the adhesive. It can be seen that the adhesive spreads significantly faster. Fig 5.21 plots the length which the adhesive has propagated over time with and without pretreatment. It is clearly visible, that oxygen plasma pretreatment cuts the required time by more than a factor of two. It follows, that the filling of a gap between two MMICs or between an MMIC and a PCB by capillary action strongly benefits from oxygen plasma pretreatment.

5.3.2 Design

To investigate the performance of planar printed interconnects, a simplified assembly has been chosen. Instead of placing two components next to each other and filling the remaining gap, a single alumina substrate was structured to feature two CPW segments divided by a gap. This is possible because the

ProtoLaser R4 used to structure the metal layer can also structure the alumina substrate itself.

A 625 μm thick alumina substrate with a single side gold cladding of 4 μm thickness has been chosen for this assembly. The CPW lines have been designed for a characteristic impedance of 50 Ω . The minimum gap size that can be created with the ProtoLaser R4 is 20 μm . Therefore, 20 μm conductor spacing has been chosen which requires a center conductor width of 32 μm . The ground conductors are 80 μm wide. Each CPW segment is 1 mm long.

To be able to deembed the interconnect from the transmission lines and precisely determine its performance, a custom TRL calibration has been manufactured. The Thru standard is 2 mm long, which mathematically removes exactly the feeding lines to the printed interconnects from the measurements.

The smallest width of the gap is 20 μm in accordance with the limits of the laser system. Wider gaps have been manufactured as well to investigate how the gap width influences the interconnect performance.

The contents of this chapter 5.3.2 have previously been published in [16, 18]. This chapter borrows from those two publications.

5.3.3 Manufacturing

Since an alumina substrate with gold cladding has been used for the investigation of planar printed interconnects, special process for the substrate structuring are required. We used the *LPKF* ProtoLaser R4 to structure the substrate. Besides structuring gold with a single-digit μm precision, it can also be used to structure the alumina substrate itself. In consequence, the transmission lines and the gaps could be created in a single process, which eliminates misalignment errors.

The gaps have been filled with the two component epoxy adhesive Duralco 4460 glue purchased from Polytec. We have selected this specific glue for its high temperature stability. It is certain to withstand the high temperatures required for thermal sintering of the printed silver inks. To fill the gaps, capillary forces were employed as described in chapter 5.3.1. Prior to applying the adhesive, the substrates underwent a 3 min plasma pretreatment.

After filling the trenches with glue, a height dip of 3 μm remains. Its surface profile is curved and does not exhibit sharp edges. This is important to enable printing over it without risking cracks during sintering.

The contents of this chapter 5.3.3 have previously been published in [16, 18]. This chapter borrows from those two publications.

The following chapters 5.3.4 and 5.3.5 will elaborate on the manufacturing processes specific to AJ and UPD printed planar interconnects. They will also present and discuss the respective measurement results.

5.3.4 AJ Printed Planar Interconnects

This chapter presents the manufacturing process of the AJ printed planar interconnects. It also shows and discusses their measurement results.

5.3.4.1 Printing

The interconnects were fabricated using an AJ 5X aerosol jet printer by Optomec in a clean room environment. Since planar structures were to be printed, it has been used in the 3-axis setup. As for the ramp-based interconnects presented in chapter 5.2.2, we used JS-A221AE silver nanoparticle ink by Novacentrix, because it allows for fine features and low surface roughness. For more homogeneous surfaces and to limit the aspect ratio, 1 part ink was diluted with 2 parts deionized (DI) water by volume. An additional 5 % by volume of TGME was added to reduce drying. We loaded the ultrasonic atomizer with 3 mL of the modified ink. The bubbler was filled with DI water and no gas bypass was used. All other printing and design parameters are shown in table 5.8. Those parameters operate the printer at the limits of its capability in terms of precision. As discussed in chapter 4.1, the Divert/Boost shutter leads to an inconsistent material deposition rate after prolonged non-printing times. Since the printed structures were small, the print time was short and most of the print would have been performed in the inconsistent regime. Therefore, the divert/boost shutter was completely turned off and a mechanical shutter was used instead. To avoid material buildup caused by the extremely fast opening time of the mechanical shutter of around 3 ms and the acceleration of the printer,

we utilized the SOTF routine. The physical height of the mechanical shutter necessitated a standoff distance of 3 mm between nozzle and substrate. The settings utilized for printing the interconnects resulted in a silver thickness of 1.5 μm .

Figure 5.22 shows the printed interconnects connecting gold CPW lines. The very narrow trenches in combination with the slight curvature of the trench filler reduced the reflected light from the printed interconnect in this region. Therefore, it seems at first sight as if material was missing in the trench. Investigation with more light and higher magnification, as well as electrical measurements, reveal that the printed structure continues without any noticeable defects over the trench as shown in the magnified section in the Figure 5.22.

As discussed above, SOTF was utilized for the printing of the interconnects. This was, however, before the calculation subroutines were debugged as described in chapter 4.1.3. The result are the short lines visible in the top of every printed surface in Figure 5.22. Since those defects are placed on top of the conductors, they do not cause problems in this application.

Table 5.8: Aerosol jet printing parameters. Reprinted from [16].

Sheath	25 SCCM
Atomizer	8 SCCM
UA power	400 mA
UA temperature	26 °C
Platen temp.	30 °C
Printing speed	2.2 mm/s
Line width	14 μm
Line pitch	9 μm

The substrates were treated in an oxygen plasma for 3 min directly before printing to improve adhesion of the printed silver. The printed silver was sintered on a preheated hotplate at 250 °C for 10 min.

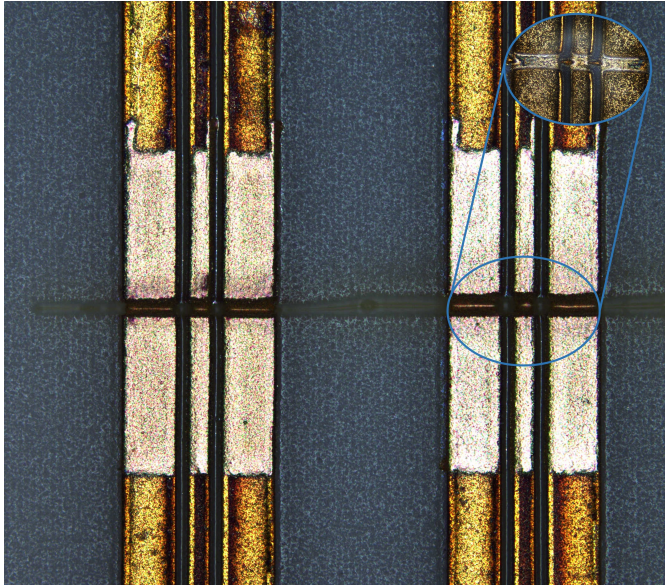


Figure 5.22: Printed interconnects. Left: trench width 20 μm , right: trench width 30 μm .

5.3.4.2 Results and Discussion

All RF measurements were done on a Keysight PNA-X with OML frequency extenders for 110 - 170 GHz and Model 170 picoprobes by GGB. A two-tier calibration was used to evaluate the interconnect performance: a first LRRM calibration on a CS-15 impedance standard substrate for on-wafer measurements and a successive TRL calibration [DJM02] on a custom calibration substrate. The launch length had been chosen as 1 mm, which matches the feed line length to the printed interconnects and hence allows de-embedding the entire feed. For the measurements, the impedance standard substrate, the TRL calibration substrate, and the device under test have been placed on an absorber.

The most important parameter for the performance of an interconnect is its insertion loss, followed by the return loss. The insertion loss of the measurement is shown in Figure 5.23 while the return loss is plotted in Figure 5.24. The measurements depicted as pale curves includes the probe contacts, two 1 mm

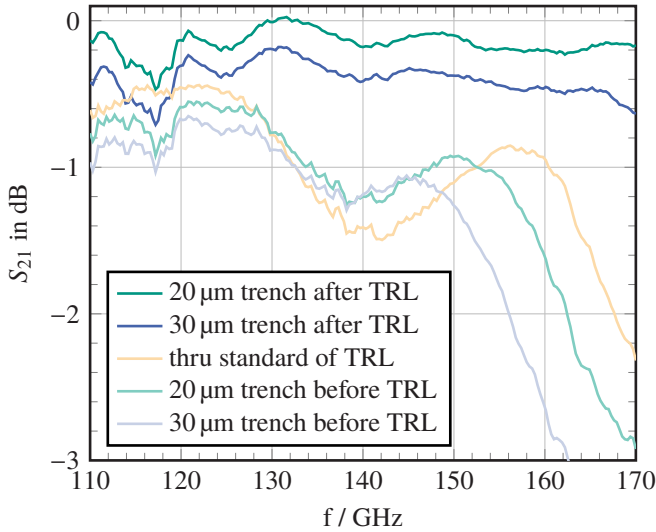


Figure 5.23: Insertion loss of AJ printed interconnects including before and after second tier TRL calibration.

long feeding lines and the interconnect. The losses drastically increase above 150 GHz. This behavior is inherent to the chosen transmission line, as shown by the measurement of the Thru standard. The only ways to improve this behavior are to reduce the dimensions of the CPW line, to select a substrate with a lower permittivity, to include a via fence or to choose a different transmission line type.

The losses introduced by the CPW line itself make it hard to estimate the performance of the printed interconnect. Therefore, a second tier calibration is used to mathematically remove the influence of the feeding lines and the probe contact from the measurement. This results in the S-Parameters of the interconnect alone. The TRL calibrated measurement is shown in Figure 5.23 and 5.24 as saturated curves. Evidently, most losses visible in the measurements before second tier calibration stem from the feeding lines, not from the printed interconnect.

The interconnect over a 20 μm wide trench, shows an insertion loss better than 0.23 dB from 119 - 170 GHz. The interconnect length plays a crucial role for

its performance. Increasing the length by $10\text{ }\mu\text{m}$ to a trench width of $30\text{ }\mu\text{m}$, increased the insertion loss by approximately 0.2 dB . Therefore, it is best to keep the printed interconnects as short as possible. If the utilized pick and place equipment is sufficiently precise to achieve a gap size of $20\text{ }\mu\text{m}$, the performance depicted by the saturated green curve in Figure 5.23 can be expected.

Figure 5.24 shows that the printed interconnects are well-matched in the entire D-Band, with the $20\text{ }\mu\text{m}$ long version exhibiting a return loss below 11 dB . As expected, this is a key advantage of printed interconnects over e.g. bond wires: The ability to shape them in such a way that they maintain the characteristic impedance of the transmission lines they are connecting, allows for good matching over a wide frequency range.

Comparing the pale and saturated curves in Figure 5.23 shows that the drop in performance above 150 GHz is only visible for the measurement including the feeding lines. This behavior is explained by the much shorter length of the interconnect compared to the feeding lines. It signifies however, that a careful system design is required for optimum performance: The interconnects themselves introduce very low losses. Keeping the transmission lines after the interconnects as short as possible, adding via fencing or switching to a different transmission line type, can yield systems with low losses. Therefore, printed interconnects can be seen as an enabler to very low-loss broadband systems operating in D-Band.

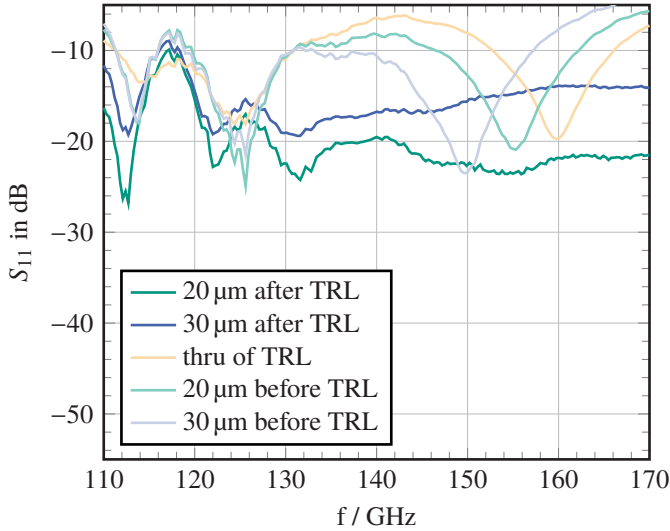


Figure 5.24: Reflection loss of AJ printed interconnects before and after second tier TRL calibration.

5.3.5 UPD Printed Planar Interconnects

This chapter presents the manufacturing process of the AJ printed planar interconnects. It also shows and discusses their measurement results.

5.3.5.1 Printing

The interconnects were fabricated using a UPD printing system in a cleanroom environment. As presented in chapter 2.3.2, the nozzle of the UPD printer is slightly flexible and can intrinsically compensate for minor variations in substrate height. However, this nozzle slack was not sufficient to compensate for the remaining dip in the filled gaps in this experiment. By the time of this experiment, our program presented in chapter 4.2.1 which projects printing paths onto a measured surface, had not been developed yet. Therefore, a different approach had to be chosen. The following elaborations on this approach clearly show how the projection program facilitates printing onto non-planar surfaces.

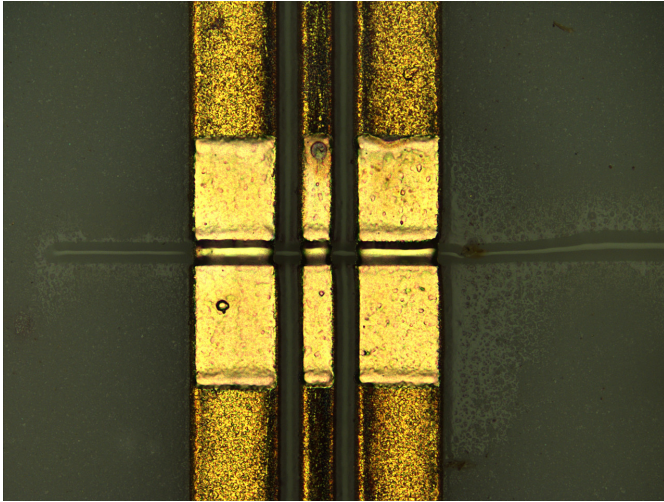


Figure 5.25: Printed interconnect with a trench width of 20 μm . Reprinted from [18]. © 2023 IEEE.

For this investigation, a custom printing script was programmed with the following working principle: The printer will follow a profile starting on the first CPW segment over the trench and onto the second CPW segment. The nozzle will then be lifted and moved back to the start point and repeat the same profile with a small offset and so on. Before printing, the user needs to manually teach the first line including x, y, and z coordinates. This is done by manually moving the nozzle along the desired profile and saving the positions. All further printing lines are then automatically computed by providing the desired center and ground conductor dimensions as well as the conductor spacing and the desired line pitch. The tedious and time-consuming work of manually teaching the first line can completely be omitted in future work, thanks to the projection program developed and presented in chapter 4.2.1.

A 5 μm nozzle has been used with a pressure of 8 bar and a printing speed of 0.05 mm/s. This yields a line width of 4 μm and a pitch of 3 μm was chosen. Directly before printing, the substrates underwent an oxygen plasma pretreatment for 3 min. Thermal sintering on a preheated hotplate at 250 °C for 10 min was used.

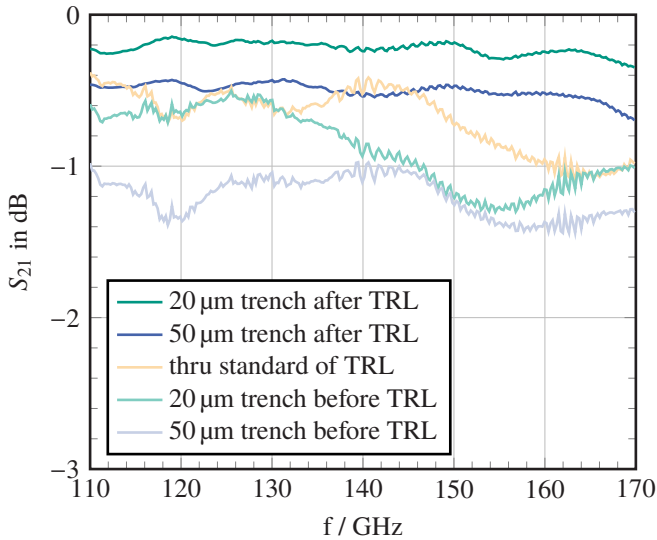


Figure 5.26: Insertion loss of UPD printed interconnects. Reprinted from [18]. © 2023 IEEE.

5.3.5.2 Results and Discussion

All RF measurements were done on a Keysight PNA-X with OML frequency extenders for 110 - 170 GHz and Model 170 picoprobes by GGB. A two-tier calibration was used to evaluate the interconnect performance: a first LRRM calibration on a CS-15 impedance standard substrate for on-wafer measurements and a successive TRL calibration [DJM02] on a custom calibration substrate. The launch length had been chosen as 1 mm, which matches the feed line length to the printed interconnects and hence allows de-embedding the entire feed. For the measurements, the impedance standard substrate, the TRL calibration substrate, and the device under test have been placed on an absorber.

The insertion loss of the measurement without second tier calibration is shown in Figure 5.26. This measurement includes the probe contacts, two 1 mm long feeding lines and the interconnect. The measurement of a 2 mm long thru is given as comparison. The proximity of the interconnect measurement to the

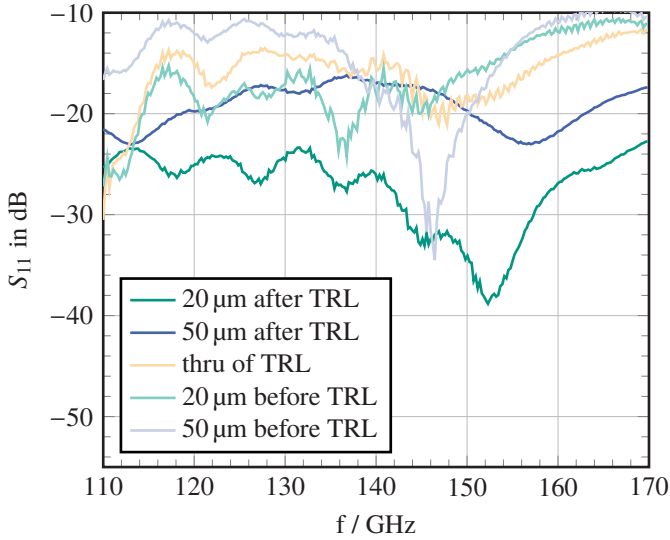


Figure 5.27: Reflection loss of printed interconnects after de-embedding the feeding lines with a custom TRL calibration. Reprinted from [18]. © 2023 IEEE.

thru measurement already shows that the largest part of the losses stems from the feeding lines and not from the interconnect.

The insertion loss of the interconnect after second tier calibration is shown in Figure 5.26 as solid color curves. The 20 μm long interconnect shows an insertion loss of 0.22 dB on average. It performs better than 0.35 dB from 110 - 170 GHz. Increasing the interconnect length to 50 μm increases the loss to an average of 0.5 dB while maintaining a loss below 0.7 dB in the entire D-Band.

Figure 5.27 shows the reflection loss of the UPD printed interconnects. The solid color curves represent the measurement with second tier calibration while the faded curves include the probe contacts and feeding lines. The 20 μm long version shows an average reflection loss of 27.5 dB after TRL calibration. It reaches a worst-case value of 23 dB in the entire D-Band. The longer interconnect shows slightly decreased matching with an average value of 20 dB while maintaining a reflection loss better than 17 dB from 110 - 170 GHz.

These values demonstrate that UPD printed mmW interconnects exhibit excellent input matching in the entire D-Band. They are broadband while exhibiting losses as low as 0.35 dB from 110 - 170 GHz.

5.3.6 Summary on AJ and UPD Printed Planar Interconnects

This chapter presented planar interconnects printed with an AJ and a UPD printer. They were printed over a polymer-filled gap connecting two CPW segments on an alumina substrate with gold metallization. For each of the printing processes, two interconnect lengths were manufactured, the shortest one being 20 μm .

A custom TRL calibration substrate was manufactured to remove the influence of the feeding lines from the measurements of the interconnects in a second tier calibration. This revealed a reflection loss better than 18 dB from 121 - 170 GHz for the AJ printed interconnect and better than 26 dB in the entire D-Band for the UPD printed interconnect. The AJ printed interconnect exhibited a higher reflection loss from 110 - 121 GHz which remained better than 11 dB, however.

Both printing technologies created interconnects with an excellent insertion loss: The AJ printed interconnect showed a loss of 0.2 dB from 119 - 170 GHz while the UPD printed interconnect exhibited a loss below 0.35 dB in the entire D-Band. The slightly higher losses of the UPD printed interconnect can be attributed to the lower print thickness. Increasing the printed metal thickness by printing a second layer could likely cut losses. Table 5.9 gives a comparison of AJ and UPD printing for planar interconnects in D-Band.

AJ printing comes with the additional advantage of a shorter printing time. It also can deal with uneven surfaces more easily. UPD printing however, does not suffer from overspray and can print smaller features. This becomes all the more important once the frequencies extend above D-Band, because they would require structure and gap sizes too small for AJ printing for optimum performance. This is the case in the next chapter, where a UPD printed interconnect is employed to connect a GaAs amplifier and an InP LWA operating from 270 - 330 GHz.

Table 5.9: Comparison of AJ and UPD printing for planar interconnects. The values in dB are the worst values measured for a 20 μm long interconnect in D-Band (110 - 170 GHz). The higher insertion loss of the UPD printed interconnect is likely caused by the lower print thickness and could be mitigated by a second printed layer.

* 121 – 170 GHz only

	AJ	UPD
Insertion loss	0.2 dB*	0.35 dB
Reflection loss	18 dB*	26 dB
Scalability to higher frequencies	-	+
Simplicity of manufacturing	+	-

6 Demonstrator: Active Leaky Wave Antenna with UPD Printed Interconnect in H-Band

The previous chapters presented an optimization of the printing systems as well as isolated printed mmW interconnects. This chapter makes the next step by presenting the introduction into a real-world system: a printed interconnect is used to create an active leaky wave antenna (LWA). It connects an amplifier and the antenna which both operate from 270 - 320 GHz. Since the amplifier is based on GaAs and the antenna is made in InP, this chapter also demonstrates heterogeneous integration with printed sub-THz interconnects.

The contents of chapter 6 were previously published in [4]. Text, structure, images, tables, presentation, and content can show modifications here. The conceptualization of this work was done by Georg Gramlich and Akanksha Bhutani. The design and manufacturing of the assembly were carried out by Georg Gramlich. Measurements were conducted by Elizabeth Bekker, Joel

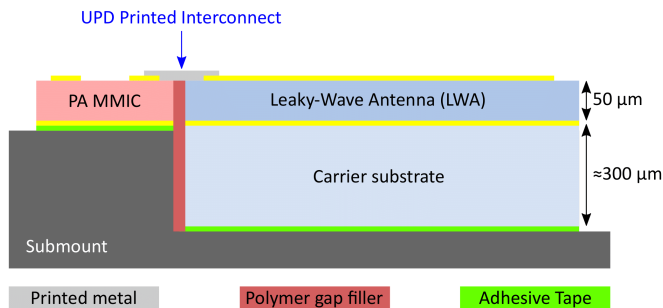


Figure 6.1: Schematic of a planar hybrid-integration assembly consisting of a PA MMIC and a LWA connected by a UPD printed interconnect. Reprinted from [4].

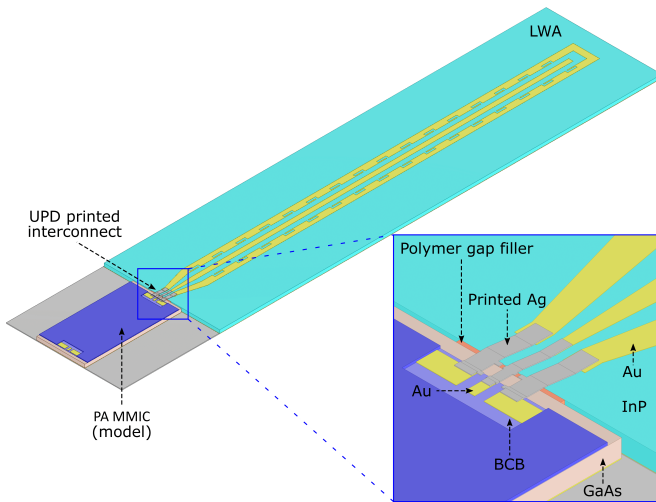


Figure 6.2: Simulation model of the PA MMIC (model with RF pads only) and the LWA with a UPD-printed interconnect. Reprinted from [4].

Dittmer, and Akanksha Bhutani. Martin Roemhild and Holger Baur contributed to the optimization of the printing and sintering processes under the supervision of Norbert Fruehauf. Fabian Thome, Axel Tessmann, and Michael Kuri designed, tested, and provided the PA-MMIC and the DC-PCB. Luca Valenziano manufactured the wirebond interconnects between the PA-MMIC and the DC-supply PCB. Tom Neerfeld manufactured the LWA based on a specialized InP process developed under the supervision of Andreas Stöhr. The paper was written by Georg Gramlich and Akanksha Bhutani. Sebastian Randel, Christian Koos, Thomas Zwick, and Akanksha Bhutani acquired funding for this project. Overall supervision and coordination of this work were provided by Akanksha Bhutani.

6.1 Assembly Overview and System Simulation

The investigations in chapter 5 showed that planar interconnects yield better performance than ramp-based ones in D-Band. Therefore, a planar interconnect

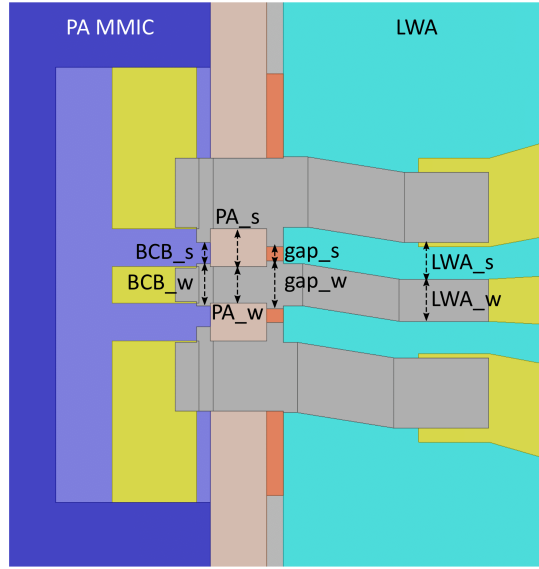


Figure 6.3: Dimensional parameters of the UPD-printed CPW interconnect between the PA MMIC and the LWA. Reprinted from [4].

has been chosen for the assembly presented in this chapter. In the comparison between AJ and UPD printing in chapter 5.3.6, we discussed that the latter technology is likely better suited for printed interconnects at higher frequencies than D-Band because of the smaller minimum feature sizes it supports. Since the active LWA presented in this chapter is operating in H-Band and requires a minimum gap and feature size of $10\text{ }\mu\text{m}$, it has been manufactured by UPD printing.

A key challenge in this work is the hybrid integration of the power amplifier (PA) MMIC and the LWA. They are fabricated using different technologies and therefore have different physical profiles. The PA MMIC is based on a 35 nm GaAs mHEMT process. Its dimensions are $1.5\text{ mm}\times 0.75\text{ mm}$. Its stackup consists of a $50\text{ }\mu\text{m}$ GaAs substrate with a $1.7\text{ }\mu\text{m}$ thick benzocyclobutene (BCB) layer on top in the area of the RF pads. Additionally, it has two frontside gold (Au) metal layers with a total thickness of $3.4\text{ }\mu\text{m}$ and one $2.7\text{ }\mu\text{m}$ thick

backside metal layer. This stackup results in a nominal MMIC thickness of 56 μm .

The LWA is based on a 50 μm InP substrate (dielectric constant, $\epsilon_r=12.4$, and dielectric loss $\tan \delta_e=0.009$ at 300 GHz) with 1 μm thick frontside and backside Au layers. The LWA has a total length of 6.8 mm which means that it is over 130 times as long as it is thick. To further complicate things, InP is a brittle material. Therefore, the InP wafer is bonded to a 300 μm thick silicon wafer (i.e., carrier substrate, as shown in Figure 6.1) by thermocompression bonding before the lithographic Au structures are applied. This provides mechanical stability to the LWA, decreasing the defects caused during processing and handling. A detailed process flow showing the fabrication of an InP LWA bonded to a silicon wafer is shown in [LHS⁺21]. The stackup of the LWA results in a total height of 352 μm .

The LWA consists of a cascade of 16 grounded CPW leaky-wave unit cells. Each unit cell has a length of 366 μm which is approximately one guided wavelength. The cells consist of two mirrored L-shaped slots in the lateral ground planes of the CPW. The measurement results of the LWA show that it operates from 220 GHz to 325 GHz, with a peak antenna gain of up to 13.5 dBi and a beam-steering range of -60° to 35° [BKD⁺]. The LWA substrate is 6.8 mm \times 1.8 mm in size.

Chapter 5.3 showed that the loss of a printed mmW interconnect depends heavily on its length. Therefore, the PA MMIC and the LWA should be placed as closely together as possible while also eliminating the difference in height. To this aim, they are placed on a metal submount with a small edge-to-edge gap of 11 μm . This gap is subsequently filled with a polymer (NEA 123M by Norland Products Inc.) with a stable $\epsilon_r \approx 3$ and $\tan \delta_e \approx 0.03$ in the target frequency range [19]. Furthermore, the submount features precisely milled steps, which compensate for the height difference between the two MMICs and ensures that the frontside Au layers of both the LWA and the PA MMIC are aligned at the same height.

Both MMICs have ground-signal-ground pads with a 50 Ω impedance. For minimal losses, the printed interconnect has been designed as a CPW transmission line with a characteristic impedance of 50 Ω along its entire length. It connects the output pad of the PA MMIC and the input pad of the LWA. On the PA MMIC, the interconnect is printed onto BCB covered GaAs close to the probe pads and directly onto GaAs close to the chip edge. It then continues

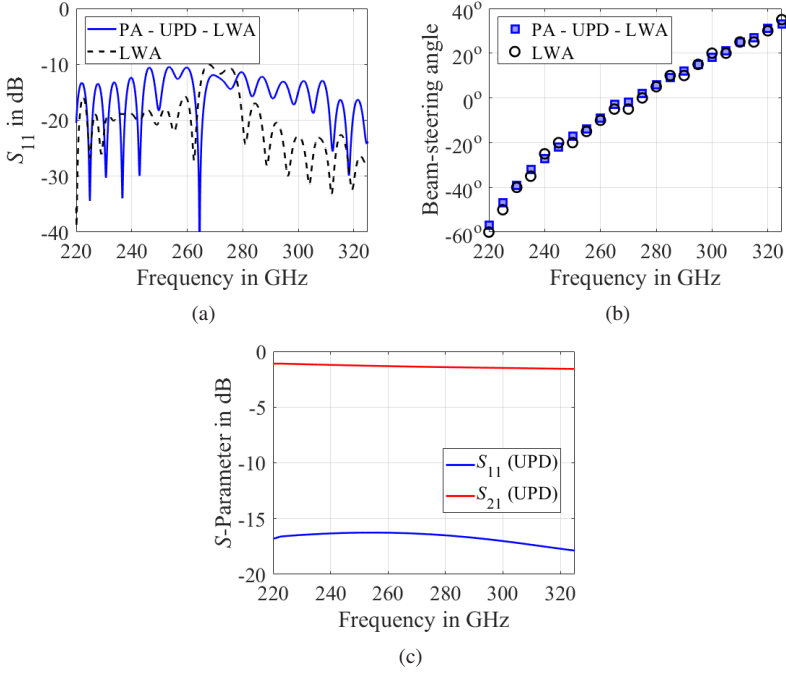


Figure 6.4: Simulation of the planar hybrid-integration assembly consisting of the PA MMIC (model with RF pads only), UPD-printed CPW interconnect, and the LWA, compared to the LWA alone with respect to the following: (a) Reflection coefficient (b) Beam-steering angle (c) Simulated S-parameter of the UPD-printed CPW interconnect using waveguide ports at the output RF pads of the PA MMIC and the input RF pads of the LWA. Reprinted from [4].

over the polymer gap filler and onto InP on the LWA. Since the materials onto which the interconnect is printed have drastically different permittivities, the dimensions of the interconnect have to vary accordingly to maintain a constant line impedance.

A simulation model of the PA MMIC and LWA with UPD printed interconnect is shown in Fig. 6.2. The silicon-based carrier substrate is not included in the model, as it only provides mechanical stability for placing the LWA on the submount. Furthermore, it is electromagnetically isolated by the back metal

ground plane of the LWA. The PA MMIC model includes only the RF pads. A zoomed view of the UPD printed interconnect, also shown in Fig. 6.2, presents the stepped structure of the interconnect in greater detail. In this assembly, the UPD printed CPW interconnect starts on the Au metal pads of the PA MMIC, crosses a thin BCB layer on GaAs, and then extends directly over the GaAs substrate until it reaches the edge of the PA MMIC. Thereafter, the UPD printed CPW interconnect continues over a polymer gap filler onto the InP substrate of the LWA. Since each of these dielectric materials has a different dielectric constant, the physical dimensions of the UPD printed CPW interconnect are adjusted depending on the dielectric constant of the substrate on which it is printed. Furthermore, the constraints of the UPD printing process, such as minimum feature sizes, gap sizes, and the pad layouts of the MMICs, are also considered to optimize the geometry of the interconnect. The dimensional parameters of the UPD printed CPW interconnect between the PA MMIC and the LWA are shown in Fig. 6.3 and their values are listed in Table 6.1.

Two different simulations are conducted using CST Microwave Studio software. In the first simulation, only one waveguide port is set up at the output RF pads of the PA MMIC. They are connected to the LWA via the UPD printed CPW interconnect. The reflection coefficient (S_{11}) and the beam-steering angle obtained from the hybrid assembly simulation (marked as 'PA - UPD - LWA') are compared with those of the LWA itself, as shown in Fig. 6.4(a) and Fig. 6.4(b), respectively. In the frequency range from 220 GHz to 325 GHz, the S_{11} of the hybrid assembly 'PA - UPD - LWA', similar to that of the LWA itself, is less than -10 dB, indicating good impedance matching between the RF pads of the PA MMIC, the UPD printed interconnect, and the LWA. Additionally, the beam-steering angle of the hybrid assembly 'PA - UPD - LWA' sweeps from -57° to 33° as the frequency increases from 220 GHz to 325 GHz. This is in good agreement with the LWA, whose beam-steering angle varies from -60° to 35° , as shown in Fig. 6.4(b). In the second simulation, two waveguide ports on either side of the UPD printed CPW interconnect are used. One port is at the edge of the output RF pads of the PA MMIC, and the other port is at the input RF pads of the LWA. The resulting reflection coefficient (S_{11}) and the transmission coefficient (S_{21}) are shown in Fig. 6.4(c). The dimensions of the realized interconnect have been measured and used in this simulation. In the frequency range of 220 GHz to 325 GHz, the simulated S_{11} is less than -16 dB, and the simulated S_{21} varies between -1.1 dB and -1.7 dB.

Table 6.1: Target and realized dimensions of the UPD-printed interconnect between the PA MMIC and LWA. Reprinted from [4].

Dim.	Target dim. / μm	Realized dim. / μm	Difference / μm
BCB_w	30	29	-1
BCB_s	15	16	+1
PA_w	26	22	-4
PA_s	27	31	+4
Gap_w	60	58	-2
Gap_s	10	12	+2
LWA_w	30	28	-2
LWA_s	26	27	+1

6.2 Manufacturing

As mentioned in section 6.1, a key objective of this work is to minimize the length of the UPD printed CPW interconnect to reduce the insertion loss. This requires precise alignment of the top surfaces of the PA MMIC and the LWA. To achieve this, the heights of both components are measured using a WLI, and the metal submount shown in Fig. 6.1 is designed based on these measurements. The submount is manufactured by CNC machining of a tungsten-copper (CuW) block. CuW is chosen for the submount due to its linear coefficient of thermal expansion (CTE less than $7.5 \times 10^{-6} \text{K}^{-1}$) [KG24b], which closely matches that of GaAs and InP [SSM]. The CuW submount functions as a mechanical support, leveling structure, and ground connection for the PA MMIC. It is electroplated with a $2 \mu\text{m}$ Au layer to ensure high conductivity and prevent oxidation. The PA MMIC and the LWA are attached to the stepped structure of the CuW submount using an electrically conductive die-attach film from Furukawa Electric [FEC24].

The PA MMIC and the LWA are placed on the CuW submount using the FINEPLACER[®] femto 2, an automatic bonder equipped with high-precision optical systems that enable die placement with sub-micrometer precision [KG24a]. As previously mentioned, the PA MMIC and the LWA are to be placed as close together as possible so a short UPD printed CPW interconnect can be printed

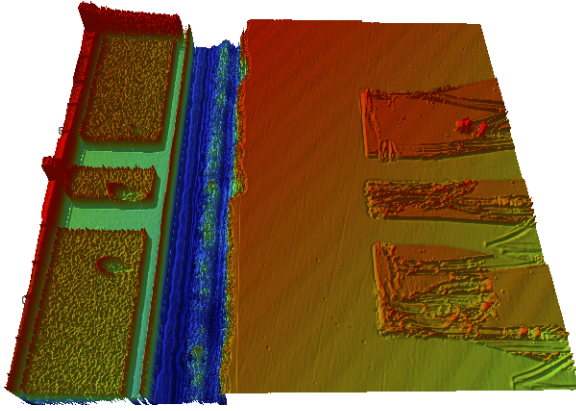


Figure 6.5: Surface topology of the PA MMIC and LWA assembly prior to printing, measured with a WLI. The Au pads of the PA MMIC are visible on the left (red-green), surrounded by BCB (green), followed by the bare die area and the polymer-filled gap (both blue), and finally the InP LWA with Au pads on the right (red-green). Scratch marks from previous RF measurements can be seen on the pads. Reprinted from [4].

for minimal insertion loss. A significant challenge in this task arises due to the $300\text{ }\mu\text{m}$ step in the submount at the edge of the PA MMIC, as shown in Fig. 6.1. The milling process results in a slightly non-vertical step of the submount, which complicates the alignment of the PA MMIC and the LWA.

While the FINEPLACER[®] femto 2 provides near-perfect accuracy in automatic mode, it is still sensitive to human error in manual mode. The operator has erroneously chosen a slightly off-center structure on the PA to perform the alignment. Consequently, a $10\text{ }\mu\text{m}$ misalignment is observed between the RF signal pads of the PA MMIC and the LWA. This shift is also modeled in the CST simulation of the UPD printed CPW interconnect shown in Fig. 6.3. It should be noted that in processes like flip-chip bonding, such an error could render the entire assembly unusable. However, the printing paths for the interconnects can easily be adapted to compensate for this misalignment without compromising RF performance.

Although the submount is designed to compensate for the height difference between the PA MMIC and the LWA, ensuring that their top surfaces are at the same height, it is impossible to avoid steps of a few μm in the surface

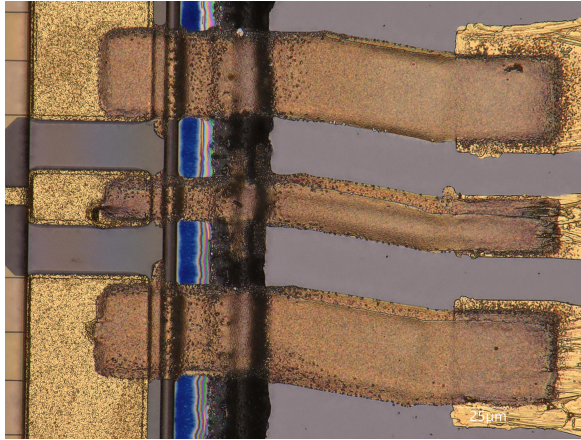


Figure 6.6: UPD printed CPW interconnect between the PA MMIC and the LWA. Reprinted from [4].

topology. These steps occur between the Au metal pads and the surrounding area of the PA MMIC, as well as between the BCB-covered sections and the bare die areas of the PA MMIC. Additionally, the polymer-filled gap between the PA MMIC and the LWA introduces a minor change in surface height. A WLI measurement of the assembly surface is shown in Fig. 6.5. Since UPD is a direct-write printing process, continuous contact between the printing nozzle and the substrate is required. This necessitates 3D printing movements to accommodate the surface topology, a feature that the printer does not inherently provide. The manufacturer optimized the system for mostly planar surfaces or manually taught profiles, making it unsuitable for the complex topology of this assembly. This shortcoming of the UPD printing system is resolved by a novel process developed in this work and presented in chapter 4.2.1. The surface to be printed on is measured with a WLI and the printing paths are projected onto it. The resulting 3D printing paths are then exported into the custom programming language of the UPD printer. To achieve optimal precision, the 2D printing paths have been manually adjusted in this project.

Printing is performed at a pressure of 9.5 bar and a speed of 0.025 mms^{-1} using a $5 \mu\text{m}$ nozzle, resulting in a line width of $9 \mu\text{m}$. A line pitch of $3 \mu\text{m}$ is used to fill all surfaces. To ensure high uniformity in line segments, a custom, 3D-

capable version of the "veclineramp" command (see chapter 4.2.7) is used for all printing movements. A 10 μm ramp-up and a 30 μm ramp-down distance, with a 20 ms start delay, are chosen. These short ramp distances were achievable due to the exceptionally high viscosity of the CL85 silver nanoparticle ink batch used, which allowed for a 5 bar non-printing pressure between consecutive line segments. The reduced pressure difference minimized adaptation time and, consequently, shortened the ramping distances. For segments shorter than the combined ramp-up and ramp-down distance, the printing pressure is reduced to 6 bar to prevent bulging in the printed lines.

When using the 3D projection method, precise leveling and alignment are essential to ensure that the printing start point matches the zero point in the projected printing paths as discussed in chapter 4.2.4. In this instance, both the printer and the WLI are leveled using a reference surface, and any digital leveling steps for the measured data are omitted. This approach ensures that all tilts and steps in the measurement data correspond accurately to the actual surface topology in the printer. Rotational alignment is achieved using features on the LWA. The corner of the LWA signal pad is chosen as the start point for printing, as it is clearly visible in both the printer and the measurement data, allowing for correct alignment.

Two layers of silver are printed, with a sintering step on a preheated hotplate at 250 °C for 10 min between and after the layers. This process achieves a thickness of 1 μm for the printed layers, which is also reflected in the CST simulation of UPD printed CPW interconnects shown in section 6.1. Fig. 6.6 shows the UPD printed CPW interconnect with both layers after sintering. The alignment accuracy is better than 3 μm between the printed structures, the PA MMIC, the LWA, and the two printed layers. The interconnect is printed with excellent dimensional accuracy. The realized dimensions of the different CPW segments are measured and compared with the target dimensions. The values of target and realized dimensions are shown in Table 6.1, and the corresponding designators are illustrated in Fig. 6.3. The average deviation between the target and realized dimensions is 2.2 μm , and the worst-case deviation is 4 μm .

The final step of the assembly is adding the DC connections for the power supply of the PA MMIC. This is accomplished using standard wirebond technology. The direct current (DC) voltages are routed using a quartz chip, and die caps are used to prevent the amplifier from oscillating. The DC-supply PCB, the quartz

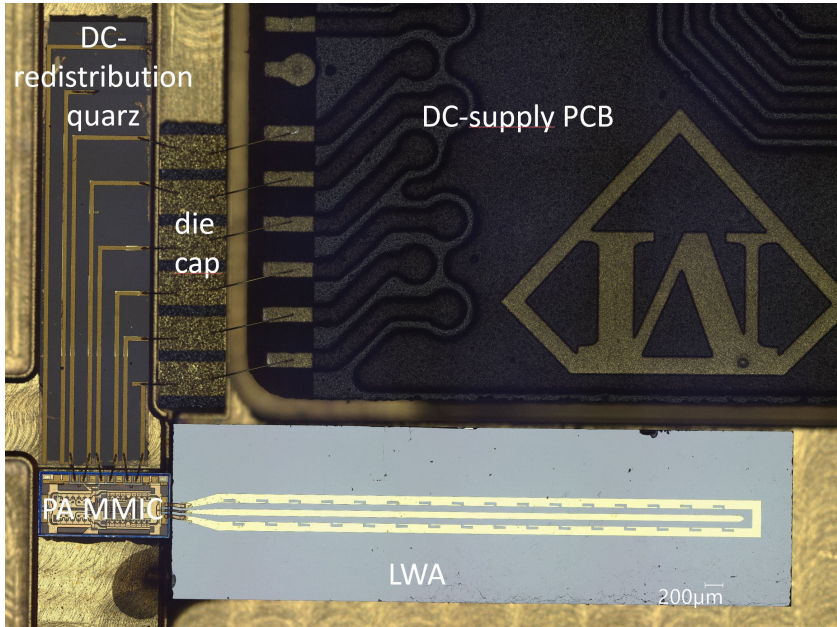


Figure 6.7: A photograph of the planar hybrid-integration assembly consisting of the PA MMIC and the LWA connected by UPD printed CPW interconnect. A part of the DC-supply PCB (top right), DC redistribution quartz chip (top left), and the die caps (top center) are also visible in the photo. Reprinted from [4].

chip, and the die caps are attached to the same CuW submount as the PA MMIC and the LWA. A photograph of the assembly after bonding is shown in Fig. 6.7.

6.3 Measurement Results and Analysis

The planar hybrid-integration assembly of the PA MMIC and the LWA with the UPD printed CPW interconnect (i.e., Hybrid Assembly under Test, Hybrid antenna under test (AUT)) is measured using a waveguide probe (Model: I325-T-GSG-100-BT) with a GSG configuration and a 100 μm pitch that operates in the WR3.4 frequency band of 220 GHz to 325 GHz. The probe-based setup used for measuring the characteristics of the hybrid AUT is shown in Fig. 6.8. A detailed

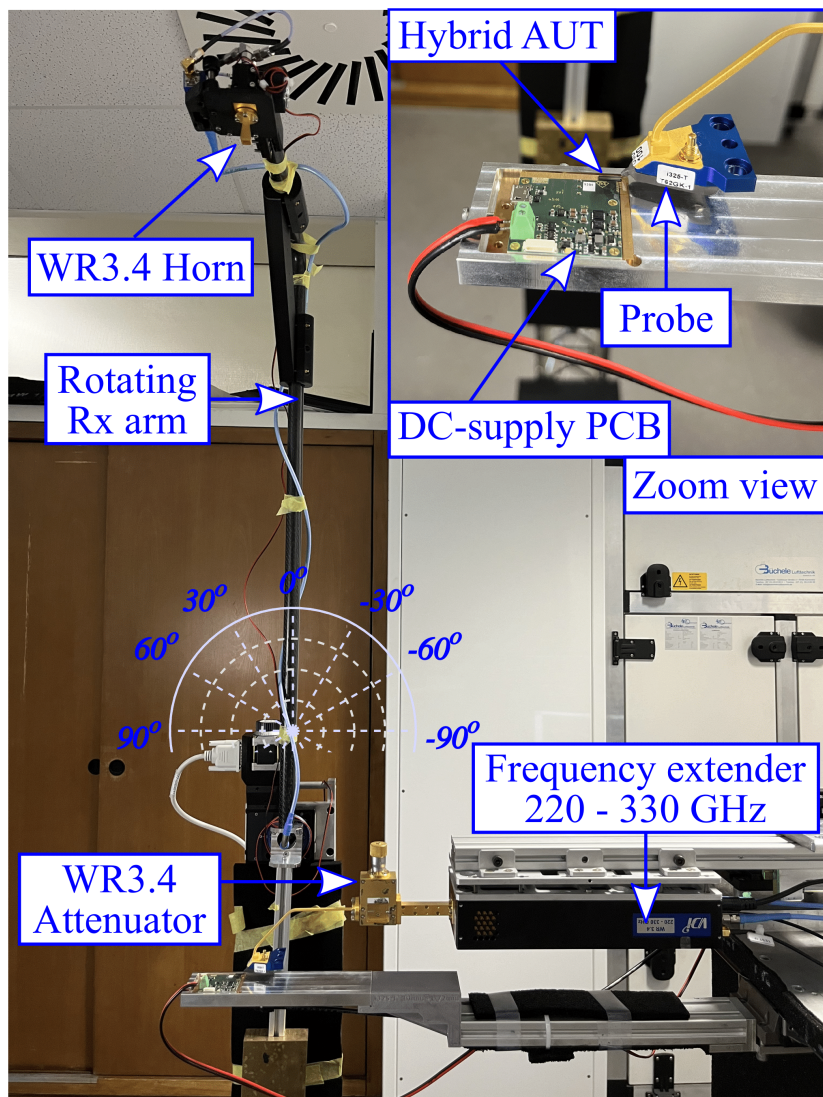


Figure 6.8: Probe-based measurement setup for the planar hybrid-integration assembly. Reprinted from [4].

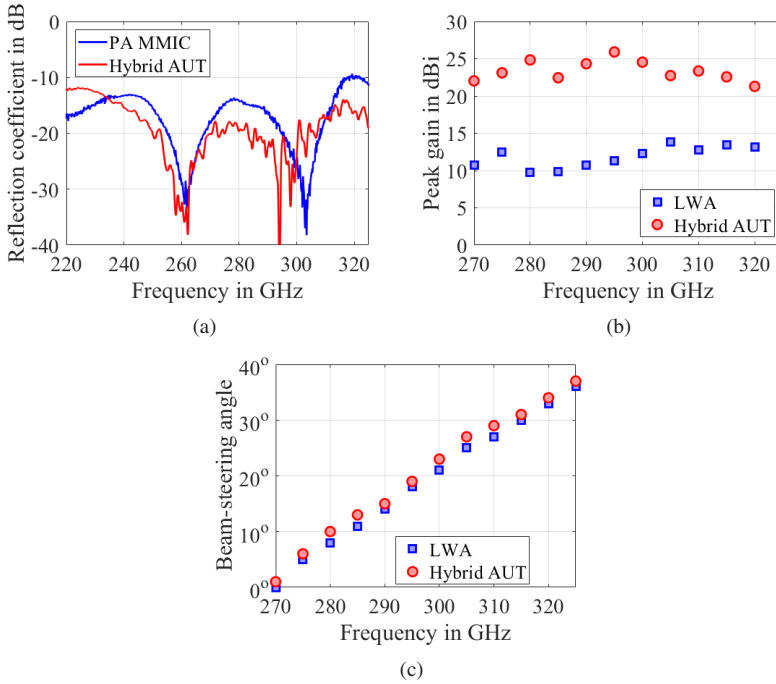


Figure 6.9: Measurement results of the planar hybrid-integration assembly (i.e., hybrid AUT) (a) Measured reflection coefficient of the hybrid AUT is compared with that of the PA MMIC alone. (b) Measured peak gain of the hybrid AUT is compared with that of the LWA alone. (c) Measured beam-steering angle of the hybrid AUT is compared to that of the LWA alone. Reprinted from [4].

description of this measurement setup and its working principle is provided in [GBD⁺13, BZ10]. In this setup, the transmitter (Tx) signal is generated by a two-port vector network analyzer (VNA) (Keysight PNA-X Network Analyzer N5242B) combined with a millimeter-wave head controller (Keysight N5261A). The Tx signal generated by the VNA is fed to a frequency extender (VDI WR3.4-VNAX) that provides a frequency coverage from 220 GHz to 330 GHz and a typical test port power of 1 dBm [VD24]. The test port of the frequency extender WR3.4-VNAX is connected to a WR3.4 waveguide attenuator, which in turn is connected to the probe. The waveguide attenuator provides an attenuation of approximately 6 dB and the typical insertion loss of the waveguide probe is

5.2 dB [For24b]. Consequently, the Tx signal has a power level of approximately -10 dBm at the probe tip. The probe contacts the hybrid AUT (i.e., the input RF pads of the PA MMIC placed at the feed end of the hybrid AUT). Therefore, the hybrid AUT serves as a Tx module in the probe-based measurement setup (see the zoom view in the inset of Fig. 6.8).

The receiver (Rx) module consists of a WR3.4 horn with a standard gain of 25 dBi and linear polarization, as specified by the manufacturer. The WR3.4 horn is connected to a WR3.4 down-conversion mixer, which is in turn connected to the second port of the VNA. The Rx module is mounted on a motorized rotational arm and is separated by a distance of 70 cm from the hybrid AUT, thus ensuring a far-field distance while measuring the radiation pattern of the hybrid AUT across the target frequency range. The hybrid AUT is precisely placed at the rotational center, and the Rx module arm is rotated around the hybrid AUT in the beam-steering plane (i.e., the plane parallel to the probe) to measure its two-dimensional far-field radiation pattern. As shown in section 6.1, the hybrid AUT includes an LWA whose beam steers from -57° to 33° as the frequency sweeps from 220 GHz to 325 GHz (see Fig. 6.4(b)). The far-field radiation pattern of the hybrid AUT is measured only in the forward quadrant (i.e., from 0° to 33°), corresponding to a frequency range of 270 GHz to 325 GHz. In this quadrant, the Rx module arm can be rotated in the cross-sectional plane parallel to the probe, with the hybrid AUT in its line of sight. On the other hand, the AUT radiation pattern in the backward quadrant (i.e., from -57° to 0°), corresponding to a frequency range of 220 GHz to almost 270 GHz, is not measured. In this quadrant, the Rx arm is shadowed by the measurement setup itself (i.e., probe, attenuator, and frequency extender) and a measurement is not possible.

The probe-based measurement setup is calibrated before measuring the characteristics of the hybrid AUT. The calibration process begins with a one-port waveguide calibration performed at the output of the waveguide attenuator using a standard rectangular waveguide WR3.4 calibration kit. The calibration standards consist of a waveguide short, a quarter-wave delay waveguide short, and a waveguide load. The calibration is performed from 220 GHz to 325 GHz with 801 frequency points and an IF bandwidth of 100 Hz. Subsequently, a gain calibration is performed by connecting a second standard-gain WR3.4 horn (25 dBi gain, linear polarization) to the waveguide attenuator. For the gain calibration, the Tx and Rx standard-gain WR3.4 horns are aligned with each other

in two orthogonal cross-sectional planes, ensuring a perfect polarization match between the Tx and Rx WR3.4 horns. The forward transmission coefficient is measured to deduce the losses of the measurement setup, which are then used to calibrate the measured peak gain of the hybrid AUT. Finally, the Tx horn is removed from the measurement setup again and an RF probe is connected instead. The probe tip is planarized, and a one-port calibration is performed using short, open, and load standards from standardized calibration substrate (Model: P/N: 138-357) [For24a].

After calibrating the measurement setup, the reference plane is positioned at the probe tip. The hybrid AUT is then contacted with the probe, providing it with an RF input signal at a typical power level of -10 dBm (as described above). The reflection loss of the hybrid AUT is measured in the target frequency range of 220 GHz to 325 GHz and compared with the measured insertion loss of the PA MMIC itself. The latter stems from the on-wafer measurements performed during the production of the PA MMIC and has been taken on the same chip utilized in the hybrid AUT assembly. The measured reflection coefficients of both the hybrid AUT and the PA MMIC show good agreement in the target frequency range, as seen in Fig. 6.9(a). This is expected because, as shown in Fig. 6.4(a), the RF output pads of the PA MMIC, the UPD printed CPW interconnect, and the LWA exhibit good impedance matching in the target frequency range, and the measured reverse isolation of the PA MMIC is as high as 30 dB to 40 dB in this range.

Subsequently, the far-field radiation pattern of the hybrid AUT is measured from 270 GHz to 325 GHz in steps of 5 GHz. As explained above, measuring the far-field radiation pattern in the lower frequency range of 220 GHz to 270 GHz is not possible due to restrictions imposed by the measurement setup. These far-field radiation pattern measurements are used to determine the peak gain and the beam-steering angle of the hybrid AUT. The measured peak gain and beam-steering angle of the hybrid AUT are compared with those of a standalone LWA, as shown in Fig. 6.9(b) and Fig. 6.9(c), respectively. The measured beam-steering angle of the hybrid AUT matches that of the standalone LWA, demonstrating that the beam-steering functionality of the LWA is not distorted by the hybrid integration of the PA MMIC with the UPD printed CPW interconnect.

By comparing the measured peak gain of the hybrid AUT and the LWA, it is can be calculated that the hybrid AUT shows a peak gain increase of up to

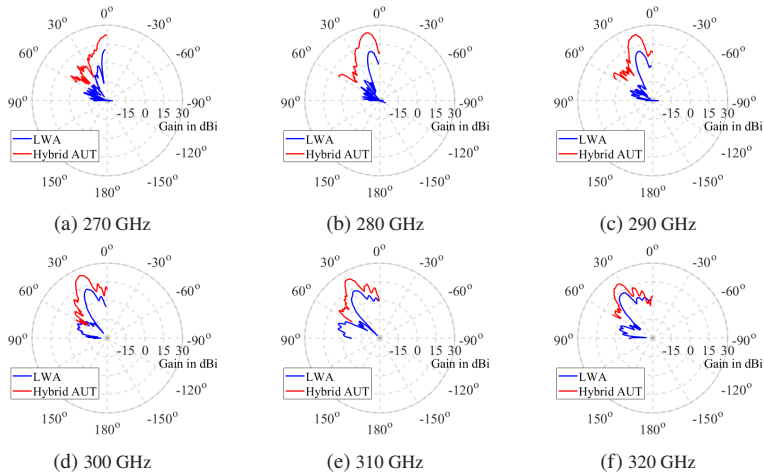


Figure 6.10: Measured far-field radiation patterns of the hybrid AUT are compared with those of the LWA alone in the beam-steering plane at frequencies (a) 270 GHz, (b) 280 GHz, (c) 290 GHz, (d) 300 GHz, (e) 310 GHz, and (f) 320 GHz. Reprinted from [4].

15 dB in the frequency range of 270 GHz to 325 GHz relative to the LWA. The on-wafer measurements of the PA MMIC show variation in the measured gain depending on the RF input power. Compared to the maximum possible gain for the PA MMIC, the on-wafer measurements corresponding to -15 dBm and -10 dBm input power show a reduction in the measured gain from 23 dB to 20 dB at 270 GHz [TL24]. Due to the typical input RF power of -10 dBm in the measurement setup of the hybrid AUT, a similar behavior is expected at higher frequencies; therefore, the gain of the PA MMIC is around 17 dB from 270 GHz to 325 GHz.

Additionally, in contrast to the on-wafer measurement of the PA MMIC, where the DC bias is directly provided using a multi-contact DC probe, in the hybrid AUT, the DC bias is supplied by connecting the PA MMIC to a DC-supply PCB through a DC redistribution quartz chip, capacitors, and wire bonds. This leads to slightly reduced biasing voltages and currents at the PA MMIC. The consequence is a further gain reduction of approximately 1 dB, which was verified through S-parameter measurements of a stand alone PA MMIC. For this verification, a standalone PA MMIC is mounted on a submount and connected

to the DC-supply PCB, DC redistribution quartz chip, and die caps with wire bonds. In other words, the standalone PA MMIC assembly is the same as the hybrid AUT assembly, except that the UPD printed CPW interconnect and the LWA are not present. The standalone PA MMIC is measured on a probe station with I325-T-GSG-100-BT waveguide probes with 100 μm pitch. In this case, two-port S-parameters of the PA MMIC are measured, and the S-parameter measurement is preceded by a two-port LRRM calibration on an ISS.

Finally, the simulated insertion loss of the UPD printed CPW interconnect is up to 1.7 dB, as shown in Fig. 6.4(c). Taking the input RF power, the biasing, and the anticipated interconnect loss into consideration, the measured peak gain of up to 26 dBi achieved by the hybrid AUT is found to be justified. The far-field radiation patterns measured in the beam-steering plane of the hybrid AUT and the standalone LWA at frequencies of 270 GHz, 280 GHz, 290 GHz, 300 GHz, 310 GHz and 320 GHz are shown in Fig. 6.10. As seen in these polar plots, the hybrid AUT exhibits the same beam-steering range, and the gain increased significantly by up to 15 dB compared to the LWA.

A comparison with prior works on planar hybrid-integration assemblies operating in the 220 GHz to 325 GHz range is shown in Table 6.2. The hybrid AUT presented in this chapter exhibits a lower assembly loss over a broad sub-THz range compared to previous works. Moreover, the hybrid AUT also achieves a very high peak gain and a low side lobe level (SLL) while maintaining a compact hybrid-integration assembly (i.e., without using a lens).

6.4 Summary on the Active LWA Demonstrator

This chapter presented a demonstrator putting the technologies developed in chapters 4 and 5 to use: The first planar hybrid-integration assembly of a PA MMIC and a beam-steering LWA using a UPD printed CPW interconnect, operating in the broadband sub-THz range of 220 GHz to 325 GHz has been shown. In this hybrid-integration assembly, a 35 nm GaAs mHEMT PA with a saturated output power of up to 14.5 dBm and an InP process-based LWA with a peak antenna gain of up to 13.5 dBi and a beam-steering range from -60° to 35° are combined. The PA MMIC and the LWA are mounted on a CuW submount with a precisely milled stepped structure that compensates for the height difference of approximately 300 μm between the PA MMIC and the LWA.

Table 6.2: Comparison with prior works on planar hybrid-integration assemblies operating in the 220 GHz to 325 GHz range. Reprinted from [4].

Ref.	Hybrid AUT	MMIC	Antenna	Frequency / GHz	Integration technique	Assembly loss / dB	Peak gain / dBi	SL / dB
This work	MMIC-Antenna	InGaAs PA	InP LW/A	220 - 325	UPD-printed CPW	1.1 - 1.7	26	-13.5
[DRT ⁺ 19]	MMIC-Antenna	GaAs x36 Multiplier	Quartz stacked patch + Lens	280 - 310	Single wirebond	3 - 4	5 (w/o lens), 23 (w. lens)	-9
[HSEZ24]	MMIC-Antenna	SiGe BiCMOS BPSK Tx	PCB antenna	230 – 255	Differential wirebond	<6	6	-
[ACHW ⁺ 21]	MMIC-Antenna	GaAs Balun	Quartz-cavity LW feed + Lens	220 - 320	Air-bridge differential interconnect	2.1 - 2.7 ^a	≈15 (w/o lens), 25 (w. lens)	-
[MKH ⁺ 24]	MMIC-Antenna	THz Amplifier ^b	Elevated slot antenna	274 ^c	Printed CPW via multi-photon laser lithography	<2	5.5	-
[ASH ⁺ 24]	MMIC-MMIC	InP and Si MMICs	n/a	up to 300	CPW based on wafer-level packaging	<4	n/a	n/a

^a For 730 μm long feed line, excluding the loss of lens and polarization mismatch.

^b The amplifier MMIC is not connected to the antenna, during the antenna measurement.

^c Antenna bandwidth not given in the paper.

Using the FINEPLACER[®] femto 2, a system equipped with high-precision optical systems enabling sub-micrometer die placement, the PA MMIC and the LWA are positioned at an edge-to-edge distance of merely 11 μm . This small gap is filled with a polymer, NEA 123M, with a well-known dielectric constant in the target sub-THz range.

The UPD printing technique is employed to print a CPW interconnect between the RF output pads of the PA MMIC and the input pads of the LWA. Since the CPW interconnect is printed on various dielectric materials, including BCB, GaAs, polymer gap filler, and InP, which have different dielectric constants and thicknesses, the geometry of the interconnect is optimized to ensure a consistent characteristic impedance of 50 Ω across its length, thus guaranteeing good impedance matching over the broadband sub-THz range. A WLI is used to measure the surface of the assembly, onto which the UPD printing paths are then projected to create 3D printing paths.

Furthermore, the UPD printed interconnect also compensates for slight misalignments between the signal pads of the PA MMIC and the LWA. The realized dimensions of the UPD printed CPW interconnect are measured and compared with the target dimensions and a worst-case deviation of 4 μm is observed. The small but various tolerances of the realized interconnect, including the thickness of the printed metal, the slight center-to-center misalignment between the PA MMIC and LWA pads, and the measured dimensions, are incorporated into the simulation model of the UPD printed CPW interconnect. The simulated S-parameters of the UPD printed CPW interconnect show an insertion loss of up to 1.7 dB in the target sub-THz range. A DC-supply PCB, DC redistribution chip, and capacitors are also mounted on the submount and connected to the PA MMIC using standard wire bonds.

A probe-based setup is utilized to measure the characteristics of the planar hybrid-integration assembly. The measured reflection coefficient of the hybrid AUT is better than -10 dB from 220 GHz to 325 GHz and closely matches the measured reflection coefficient of the standalone PA MMIC. The peak gain and beam-steering angle of the hybrid AUT are measured from 270 GHz to 325 GHz, as measurements at lower frequencies are restricted by the measurement setup. From 270 GHz to 325 GHz, the hybrid AUT achieves a measured peak gain of up to 26 dBi, demonstrating a gain enhancement of up to 15 dB compared to the LWA. Furthermore, the measured SLL of the hybrid AUT is 13.5 dB less than the peak gain and the simulated radiation efficiency is around 65% at 295 GHz.

The factors influencing the gain enhancement achieved by the hybrid AUT are carefully analyzed. This includes an examination of the RF input power at the probe tip, the DC-supply PCB and routing, as well as the anticipated insertion loss of the UPD printed CPW interconnect.

The measured beam-steering angle of the hybrid AUT varies from 0° to 37° as the frequency sweeps from 270 GHz to 325 GHz, closely matching the measured beam-steering range of the LWA itself. The experimental validation of the planar hybrid-integration assembly of the PA MMIC and LWA demonstrates that it can be used in a sub-THz Tx frontend to provide high EIRP and beam-steering functionality, suitable for a high data rate wireless communication link.

7 Conclusion

The goal of this thesis was to develop a manufacturing process for printed mmW interconnects above 100 GHz. First, two potential topographies—ramp-based and planar—were investigated. Both require distinct manufacturing processes to create the ramp and fill remaining gaps, which were carefully developed and optimized. Subsequently, an analysis of the required minimum feature size dependent on the target frequency was performed. With the topographies and minimum feature size determined, two printing processes were selected: Aerosol Jet and UPD printing. Both offer the required precision, conformal printing capability, and low ink-to-substrate interaction. Next, the printing processes were analyzed and extended.

For AJ printing, the maximum printing speed not causing path deformations for a given structure size was determined. The resulting slow printing speed can lead to thick deposited layers which are prone to crack formation. Two mitigation strategies were suggested based on the physical process behind crack formation. A new and significantly improved version of the shutter on the fly (SOTF) printing mode was developed, enabling highly precise and uniform printed structures.

The UPD printer intrinsically offers the required precision for mmW applications. However, it previously suffered from a labor-intensive workflow for conformal printing. This issue was effectively addressed through the development of a program that projects 2D print paths onto a measured surface. This advancement enables semi-automatic conformal printing and allows for printing onto more complex surface topographies than previously possible. The importance of alignment for conformal printing was mathematically demonstrated, and methods to enhance line uniformity were presented. Additionally, the phenomenon of nozzle drift in long-duration print jobs was identified and systematically analyzed.

Having the printing processes optimized and their performance qualified, multiple isolated component demonstrators were fabricated. These include an AJ-printed transmission line, as well as AJ and UPD printed ramp-based PCB-to-PCB or PCB-to-MMIC interconnects. Furthermore, AJ and UPD printed planar interconnects were manufactured using identical assemblies for direct comparability. AJ printing achieved slightly better performance in D-Band (110 - 170 GHz) and offered easier manufacturability. However, UPD printing promised superior scalability for frequencies beyond D-Band.

Finally, a UPD printed interconnect was used to assemble an active beam-steering antenna for 6G communication applications, operating in the 220 - 325 GHz range. It is made of a power amplifier based on GaAs and an InP LWA. The assembled system achieved a measured peak gain of 26 dBi, demonstrating a gain enhancement of up to 15 dB compared to the standalone LWA. This result confirms that printed interconnects enable mmW systems with a very large bandwidth and excellent performance. Additionally, printed interconnects facilitate rapid prototyping and heterogeneous integration of multiple semiconductor technologies.

Future work should focus on conducting stability analyses of printed interconnects, including thermal cycling and vibration testing. Once these tests are completed, the processes developed in this thesis can be scaled to small- and medium-batch manufacturing, allowing for a comprehensive yield analysis. Ultimately, printed mmW interconnects can be deployed in their first industrial applications.

Declarations

The author declares that the findings reported in this manuscript are the result of his original research. The manuscript's clarity and language have been enhanced with the assistance of AI-based tools, including generative AI.

A Appendix

A.1 AJ Shutter On The Fly Code

This sections detailes the modified portion of the motion controller code for the AJ5X printer by Optomec. The code has been modified to enable precise shutter on the fly timing as detailed in Section 4.1.3.

Listing A.1: Example main program using shutter on the fly

```
1  REAL XSON,YSON  ! The calculated postion in which
2  ! the shutter action should start
3  REAL STOPEN      ! The amount of time that the
4  ! shutter needs for opening
5  REAL XFP,YFP      ! The first point of the
6  ! movement; non-printing
7  REAL XFPP,YFPP    ! The first point of a PRINTED line
8  REAL XSPP,YSPP    ! The second point of a PRINTED line
9  ! — used to calculate the angle of
10 ! the line
11
12 STOPEN=0.003      ! Time to OPEN shutter in seconds
13
14
15 XFPP=0.0; YFPP=0.0; XSPP=0.0; YSPP=1.0
16 Call LEAD_CALC
17 PTP/E (X,Y),XFP,YFP
18 XSEG(X,Y),XFP,YFP
19 LINE (X,Y),XSON,YSON
20 LINE/O (X,Y),XFPP,YFPP,
21 SetOutputsVal ,OUT,0 ,OutputsMask
22 LINE (X,Y),XSOFF,YSOFF
23 LINE/O (X,Y),XLPP,YLPP,
24 ResetOutputsVal ,OUT,0 ,OutputsMask
25 LINE (X,Y),XLP,YLP
26 ENDS (X,Y)
27 TILL (^X_AST.#MOVE) & (^Y_AST.#MOVE)
28
29 STOP
```


Listing A.2: Shutter on the fly lead in calculations

```

1  !!!!!!!!!!!!!!!!!!!!!!!!!!!!!!!!!!!!!!!!!!!!!!!!!!!!!!!!!!!!!!!
2  !! Begin Shutter On The Fly Lead In Calculations !!
3  !!!!!!!!!!!!!!!!!!!!!!!!!!!!!!!!!!!!!!!!!!!!!!!!!!!!!!!!!!!!!!!
4
5  GLOBAL REAL LIN_DIST
6
7  LEAD_CALC:
8      ! Calculate lead in distance
9      LIN_DIST = 1/2 * ACC(X) * VEL(X) / JERK(X)
10     + 1/2 * POW(VEL(X),2) / ACC(X)
11
12     SON_DIST = VEL(X) * STOPEN
13
14     IF LIN_DIST < 0.300
15         LIN_DIST = 0.300
16
17     END
18
19     ! Calculate the angle of the lead in vector
20     THETA = ATAN2((YSPP - YFPP), (XSPP - XFPP))
21
22     ! Set the lead in start positions
23     XFP = XFPP - (LIN_DIST + SON_DIST) * COS(THETA)
24     YFP = YFPP - (LIN_DIST + SON_DIST) * SIN(THETA)
25
26     ! Set the shutter on positions
27     XSON = XFPP - SON_DIST * COS(THETA)
28     YSON = YFPP - SON_DIST * SIN(THETA)
29
30     RET

```


References

- [ACHW⁺21] Arias Campo, M.; Holc, K.; Weber, R.; De Martino, C.; Spirito, M.; Leuther, A.; Bruni, S.; Llombart, N.: H-Band Quartz-Silicon Leaky-Wave Lens With Air-Bridge Interconnect to GaAs Front-End. In: *IEEE Transactions on Terahertz Science and Technology* 11 (2021), Nr. 3, S. 297–309. <http://dx.doi.org/10.1109/TTHZ.2021.3049640>. – DOI 10.1109/TTHZ.2021.3049640
- [AFS18] Ahmed, F.; Furqan, M.; Stelzer, A.: 120-GHz and 240-GHz Broadband Bow-Tie Antennas in eWLB Package for High Resolution Radar Applications. In: *2018 48th European Microwave Conference (EuMC)*, 2018, S. 1109–1112
- [ASH⁺24] Araki, Y.; Shiratori, Y.; Hamada, H.; Muto, M.; Abdo, I.; Jyo, T.; Nakajima, F.: A Low-Loss DC-to-300 GHz InP/Si Interconnection Based on Wafer Level Packaging Using Chip-first/Facedown Process. In: *2024 IEEE/MTT-S International Microwave Symposium - IMS 2024*, 2024, S. 816–819
- [Bat00] Batchelor, G. K.: *An Introduction to Fluid Dynamics*. Cambridge University Press, 2000 (Cambridge Mathematical Library)
- [BKD⁺] Bhutani, A.; Kretschmann, M.; Dittmer, J.; Lu, P.; Stöhr, A.; Zwick, T.: A 220 GHz to 325 GHz Grounded Coplanar Waveguide Based Periodic Leaky-Wave Beam-Steering Antenna in Indium Phosphide Process. 12, Nr. 16. <http://dx.doi.org/10.3390/electronics12163482>. – DOI 10.3390/electronics12163482. – ISSN 2079–9292
- [BRSP21] Bajic, B.; Rikalovic, A.; Suzic, N.; Piuri, V.: Industry 4.0 Implementation Challenges and Opportunities: A Managerial Perspective. In: *IEEE Systems Journal* 15 (2021), Nr. 1, S. 546–559. <http://dx.doi.org/10.1109/JSYST.2020.3023041>. – DOI 10.1109/JSYST.2020.3023041
- [Buc] Buchanan, R. A.: *history of technology*. <https://www.britanica.com/technology/history-of-technology>

- [BWC13] Bauer, W.; Weber, M.; Chanbai, S.: *White Light Interferometry*. Springer US, 2013. – 4115–4127 S.
- [BZ10] Beer, S.; Zwick, T.: Probe based radiation pattern measurements for highly integrated millimeter-wave antennas. In: *Proceedings of the Fourth European Conference on Antennas and Propagation*, 2010, S. 1–5
- [CACP21] Craton, M. T.; Albrecht, J. D.; Chahal, P.; Papapolymerou, J.: Additive Manufacturing of a Wideband Capable W -Band Packaging Strategy. In: *IEEE Microwave and Wireless Components Letters* 31 (2021), Nr. 6, S. 697–700. <http://dx.doi.org/10.1109/LMWC.2021.3061614>. – DOI 10.1109/LMWC.2021.3061614. – ISSN 1531–1309
- [CCW⁺14a] Cai, F.; Chang, Y.-h.; Wang, K.; Khan, W. T.; Pavlidis, S.; Papapolymerou, J.: High resolution aerosol jet printing of D- band printed transmission lines on flexible LCP substrate. In: *2014 IEEE MTT-S International Microwave Symposium (IMS2014)*, 2014, S. 1–3
- [CCW⁺14b] Cai, F.; Chang, Y.-h.; Wang, K.; Khan, W. T.; Pavlidis, S.; Papapolymerou, J.: High Resolution Aerosol Jet Printing of D-Band Printed Transmission Lines on Flexible LCP Substrate. (2014)
- [CCW⁺16] Cai, F.; Chang, Y.-h.; Wang, K.; Zhang, C.; Wang, B.; Papapolymerou, J.: Low-Loss 3-D Multilayer Transmission Lines and Interconnects Fabricated by Additive Manufacturing Technologies. In: *IEEE Transactions on Microwave Theory and Techniques* 64 (2016), Nr. 10, S. 3208–3216. <http://dx.doi.org/10.1109/TMTT.2016.2601907>. – DOI 10.1109/TMTT.2016.2601907. – ISSN 0018–9480
- [Cha05] Chang, K.: *Encyclopedia of RF and Microwave Engineering, Volume 1 - 6*. John Wiley & Sons, 2005. ISSN 978–0–471–27053–9
- [CJW⁺13] Cheng, B.; Jiang, G.; Wang, C.; Yang, C.; Cai, Y.; Chen, Q.; Huang, X.; Zeng, G.; Jiang, J.; Deng, X.; Zhang, J.: Real-Time Imaging With a 140 GHz Inverse Synthetic Aperture Radar. In: *IEEE Transactions on Terahertz Science and Technology* 3

- (2013), Nr. 5, S. 594–605. <http://dx.doi.org/10.1109/TTHZ.2013.2268317>. – DOI 10.1109/TTHZ.2013.2268317
- [CKA⁺20] Craton, M. T.; Konstantinou, X.; Albrecht, J. D.; Chahal, P.; Papapolymerou, J.: A Chip-First Microwave Package Using Multimaterial Aerosol Jet Printing. In: *IEEE Transactions on Microwave Theory and Techniques* (2020), S. 1. <http://dx.doi.org/10.1109/TMTT.2020.2992074>. – DOI 10.1109/TMTT.2020.2992074. – ISSN 0018–9480
- [Cor24] Corp., N.: *Optimum Disposable Reservoir Systems*. <https://nc-p-001.sitecorecontenthub.cloud/api/public/content/763d342ed9b24b6380265648d916dab1?v=a8bca496>. Version: 2024
- [CSP⁺18] Craton, M. T.; Sorocki, J.; Piekarz, I.; Gruszczynski, S.; Wincza, K.; Papapolymerou, J.: *Realization of Fully 3D Printed W-band Bandpass Filters using Aerosol Jet Printing Technology*. Piscataway, NJ : IEEE, 2018 <http://ieeexplore.ieee.org/servlet/opac?punumber=8528202>. – ISBN 9781538652855
- [DGH⁺19] Dalal, N.; Gu, Y.; Hines, D. R.; Dasgupta, A.; Das, S.: Cracks in the 3D-printed conductive traces of silver nanoparticle ink. In: *Journal of Micromechanics and Microengineering* 29 (2019), Nr. 9, S. 097001. <http://dx.doi.org/10.1088/1361-6439/ab2f25>. – DOI 10.1088/1361-6439/ab2f25. – ISSN 0960–1317
- [DJM02] DeGroot, D. C.; Jargon, J. A.; Marks, R. B.: Multiline TRL revealed. In: *60th ARFTG Conference Digest, Fall 2002*, IEEE, 5-6 Dec. 2002. – ISBN 0–7803–8124–6, S. 131–155
- [DRT⁺19] Dyck, A.; Rösch, M.; Tessmann, A.; Leuther, A.; Kuri, M.; Wagner, S.; Gashi, B.; Schäfer, J.; Ambacher, O.: A Transmitter System-in-Package at 300 GHz With an Off-Chip Antenna and GaAs-Based MMICs. In: *IEEE Transactions on Terahertz Science and Technology* 9 (2019), Nr. 3, S. 335–344. <http://dx.doi.org/10.1109/TTHZ.2019.2910511>. – DOI 10.1109/TTHZ.2019.2910511
- [Eri21] *Ericsson Mobility Report*. 2021
- [FEC24] Furukawa Electric Co., L.: *Electrically/thermally conductive Dicing die attach film*. 2024. – <https://www.furukawa.co.jp/uvtape/en/technology/cdaf.html> [Accessed: (17.10.2024)]

- [For24a] Formfactor, I.: *Cascade Impedance Standard Substrate Map*. 2024. – <https://www.formfactor.com/download/iss-map-138-357/?wpdmdl=3179> [Accessed: (17.10.2024)]
- [For24b] Formfactor, I.: *Probe Selection Guide*. 2024. – <https://www.formfactor.com/download/probe-selection-guide/?wpdmdl=2561&refresh=67175034296b31729581108> [Accessed: (17.10.2024)]
- [FRR21] Feng, J.; Ramm, A.; Renn, M.: A quantitative analysis of overspray in Aerosol Jet® printing. In: *Flexible and Printed Electronics* 6 (2021), 10. <http://dx.doi.org/10.1088/2058-8585/ac3019>. – DOI 10.1088/2058-8585/ac3019
- [GBD+13] Gulan, H.; Beer, S.; Diebold, S.; Rusch, C.; Leuther, A.; Kallfass, I.; Zwick, T.: Probe based antenna measurements up to 325 GHz for upcoming millimeter-wave applications. In: *2013 International Workshop on Antenna Technology (iWAT)*, 2013, S. 228–231
- [GGB79] Gupta, K. C.; Garg, R.; Bahl, I. J.: *Microstrip lines and slotlines*. Dedham, Mass. : Artech, 1979. – ISBN 0-89006-074-6
- [GGF+20] Geiger, M.; Grüner, P.; Fischer, M.; Dürr, A.; Chaloun, T.; Waldschmidt, C.: A Multimodal Dielectric Waveguide-Based Monopulse Radar at 160 GHz. In: *IEEE Transactions on Microwave Theory and Techniques* 68 (2020), Nr. 11, S. 4825–4834. <http://dx.doi.org/10.1109/TMTT.2020.3006530>. – DOI 10.1109/TMTT.2020.3006530
- [GH15] Gold, G.; Helmreich, K.: Surface impedance concept for modeling conductor roughness. In: *2015 IEEE MTT-S International Microwave Symposium*, IEEE, 17.05.2015 - 22.05.2015. – ISBN 978-1-4799-8275-2, S. 1–4
- [HSEZ24] Hebel, J.; Steinweg, L.; Ellinger, F.; Zwick, T.: Performance Evaluation of Ultra-Wideband 246-GHz BPSK Transmitters on an Organic Substrate With External Chip and Substrate Antenna. In: *IEEE Transactions on Microwave Theory and Techniques* 72 (2024), Nr. 10, S. 6153–6163. <http://dx.doi.org/10.1109/TMTT.2024.3390055>. – DOI 10.1109/TMTT.2024.3390055
- [HSZ22] Hebel, J.; Steinweg, L.; Zwick, T.: Differential bondwire interface for chip-to-chip and chip-to-antenna interconnect above

- 200 GHz. In: *2022 52nd European Microwave Conference (EuMC)*, 2022, S. 306–309
- [HVG⁺17] Hassona, A.; Vassilev, V.; He, Z. S.; Mariotti, C.; Dielacher, F.; Zirath, H.: Silicon Taper Based *D*-Band Chip to Waveguide Interconnect for Millimeter-Wave Systems. In: *IEEE Microwave and Wireless Components Letters* 27 (2017), Nr. 12, S. 1092–1094. <http://dx.doi.org/10.1109/LMWC.2017.2763118>. – DOI 10.1109/LMWC.2017.2763118
- [INA21] Ilchenko, M.; Narytnyk, T.; Avdeyenko, G.: Wireless Communication Systems of Terahertz Frequency Range. In: Vorobiyenko, P. (Hrsg.); Ilchenko, M. (Hrsg.); Strelkovska, I. (Hrsg.): *Current Trends in Communication and Information Technologies*. Cham : Springer International Publishing, 2021. – ISBN 978–3–030–76343–5, S. 189–222
- [IR22] ITU-R: *Future technology trends of terrestrial International Mobile Telecommunications systems towards 2030 and beyond*. <https://www.itu.int/pub/R-REP-M.2516>, 2022. – Accessed: Oct. 02, 2024
- [IZZB18] Ihle, M.; Ziesche, S.; Zech, C.; Baumann, B.: Compact LTCC Packaging and Printing Technologies for Sub-THz Modules. (2018)
- [IZZB19] Ihle, M.; Ziesche, S.; Zech, C.; Baumann, B.: Functional Printing of MMIC-Interconnects on LTCC Packages for sub-THz applications. In: *2019 22nd European Microelectronics and Packaging Conference & Exhibition (EMPC)*, 2019, S. 1–4
- [KC12] Kwak, J. B.; Chung, S.: The effects of underfill on the thermal fatigue reliability of solder joints in newly developed flip chip on module. In: *13th InterSociety Conference on Thermal and Thermomechanical Phenomena in Electronic Systems*, 2012, S. 628–631
- [KG24a] KG, F. G. . C.: *Advanced Automatic Sub-Micron Bonder*. 2024. – <https://finetech.de/products/fineplacer-femto-2/> [Accessed: (17.10.2024)]
- [KG24b] KG, W. S. G. . C.: *Data Sheet Tungsten-Copper (WCu) [also: Copper-Tungsten CuW]*. 2024. – <https://www.whs-sond>

- ermetalle.de/images/pdf/WCu-Tungsten-Copper.pdf
[Accessed: (17.10.2024)]
- [KHBS13] Köhler, M.; Hasch, J.; Blöcher, H. L.; Schmidt, L.-P.: Feasibility of automotive radar at frequencies beyond 100 GHz. In: *International Journal of Microwave and Wireless Technologies* 5 (2013), Nr. 1, S. 49–54. <http://dx.doi.org/10.1017/S175907871200075X>. – DOI 10.1017/S175907871200075X. – ISSN 1759–0787
- [KHRC⁺] Konstantinou, X.; Herrera-Rodriguez, C. J.; Craton, M. T.; Hardy, A.; Crump, C.; Albrecht, J. D.; Fan, Q. H.; Grotjohn, T.; Papapolymerou, J.: A Monolithic Wilkinson Power Divider on Diamond via a Combination of Additive Manufacturing and Thin-Film Process.
- [KUP13] Khan, W. T.; Ulusoy, A. C.; Papapolymerou, J.: D-Band characterization of co-planar wave guide and microstrip transmission lines on liquid crystal polymer. In: *2013 IEEE 63rd Electronic Components and Technology Conference*, 2013, S. 2304–2309
- [KUSP14] Khan, W. T.; Ulusoy, A. C.; Schmid, R. L.; Papapolymerou, J.: Characterization of a low-loss and wide-band (DC to 170 GHz) flip-chip interconnect on an organic substrate. In: *2014 IEEE MTT-S International Microwave Symposium (IMS2014)*, 2014, S. 1–4
- [LHS⁺21] Lu, P.; Haddad, T.; Sievert, B.; Khani, B.; Makhlof, S.; Dülme, S.; Estévez, J. F.; Rennings, A.; Erni, D.; Pfeiffer, U.; Stöhr, A.: InP-Based THz Beam Steering Leaky-Wave Antenna. In: *IEEE Transactions on Terahertz Science and Technology* 11 (2021), Nr. 2, S. 218–230. <http://dx.doi.org/10.1109/TTHZ.2020.3039460>. – DOI 10.1109/TTHZ.2020.3039460
- [LWW17] Li, Z.; Wang, Y.; Wang, K.-S.: Intelligent predictive maintenance for fault diagnosis and prognosis in machine centers: Industry 4.0 scenario. In: *Advances in Manufacturing* 5 (2017), 12, S. 1–11. <http://dx.doi.org/10.1007/s40436-017-0203-8>. – DOI 10.1007/s40436-017-0203-8
- [ŁWW⁺22] Łysień, M.; Witczak, Ł.; Wiatrowska, A.; Fiączyk, K.; Gadzalińska, J.; Schneider, L.; Stręk, W.; Karpiński, M.; Kosior, Ł.; Granek, F.; Kowalczewski, P.: High-resolution deposition

- of conductive and insulating materials at micrometer scale on complex substrates. In: *Scientific reports* 12 (2022), Nr. 1, S. 9327. <http://dx.doi.org/10.1038/s41598-022-13352-5>. – DOI 10.1038/s41598-022-13352-5
- [Max65] Maxwell, J. C.: VIII. A dynamical theory of the electromagnetic field. In: *Philosophical Transactions of the Royal Society of London* 155 (1865), 459-512. <http://dx.doi.org/10.1098/rstl.1865.0008>. – DOI 10.1098/rstl.1865.0008
- [Max73] Maxwell, J. C.: *A Treatise on Electricity and Magnetism*. Oxford University Press, 1873
- [MFF13] Mahajan, A.; Frisbie, C. D.; Francis, L. F.: Optimization of aerosol jet printing for high-resolution, high-aspect ratio silver lines. In: *ACS applied materials & interfaces* 5 (2013), Nr. 11, S. 4856–4864. <http://dx.doi.org/10.1021/am400606y>. – DOI 10.1021/am400606y
- [MG92] Meinke, H. H.; Gundlach, F. W.: *Taschenbuch der Hochfrequenztechnik: Band 1: Grundlagen*. Springer, 1992. ISSN 978–3–540–54714–3
- [MKH⁺24] Maier, P.; Kotz, A.; Hebel, J.; Zhang, Q.; Benz, C.; Quint, A.; Kretschmann, M.; Harter, T.; Randel, S.; Lemmer, U.; Freude, W.; Zwick, T.; Koos, C.: *Freeform terahertz structures fabricated by multi-photon lithography and metal coating*. <https://arxiv.org/abs/2401.03316>. Version: 2024
- [MOB⁺08] Meyer, T.; Ofner, G.; Bradl, S.; Brunnbauer, M.; Hagen, R.: Embedded Wafer Level Ball Grid Array (eWLB). In: *2008 10th Electronics Packaging Technology Conference*, 2008, S. 994–998
- [msc] *MSCI World Index (USD)*. <https://www.msci.com/documents/10199/178e6643-6ae6-47b9-82be-e1fc565ededb>
- [MSW⁺15] Monayakul, S.; Sinha, S.; Wang, C.-T.; Weimann, N.; Schmueckle, F. J.; Hrobak, M.; Krozer, V.; John, W.; Weixelbaum, L.; Wolter, P.; Krueger, O.; Heinrich, W.: Flip-Chip Interconnects for 250 GHz Modules. In: *IEEE Microwave and Wireless Components Letters* 25 (2015), Nr. 6, S. 358–360. <http://dx.doi.org/10.1109/LMWC.2015.2424294>. – DOI 10.1109/LMWC.2015.2424294

- [MTK⁺20] Morishita, Y.; Teraoka, T.; Kashino, Y.; Asano, H.; Sakamoto, T.; Shirakata, N.; Takinami, K.; Takahashi, K.: 300-GHz-Band Self-Heterodyne Wireless System for Real-Time Video Transmission Toward 6G. In: *2020 IEEE International Symposium on Radio-Frequency Integration Technology (RFIT)*, 2020, S. 151–153
- [MYL⁺15] Mei, X.; Yoshida, W.; Lange, M.; Lee, J.; Zhou, J.; Liu, P.-H.; Leong, K.; Zamora, A.; Padilla, J.; Sarkozy, S.; Lai, R.; Deal, W. R.: First Demonstration of Amplification at 1 THz Using 25-nm InP High Electron Mobility Transistor Process. In: *IEEE Electron Device Letters* 36 (2015), Nr. 4, S. 327–329. <http://dx.doi.org/10.1109/LED.2015.2407193>. – DOI 10.1109/LED.2015.2407193
- [OAPC19] Oakley, C.; Albrecht, J. D.; Papapolymerou, J.; Chahal, P.: Low-Loss Aerosol-Jet Printed Wideband Interconnects for Embedded Devices. In: *IEEE Transactions on Components, Packaging and Manufacturing Technology* 9 (2019), Nr. 11, S. 2305–2313. <http://dx.doi.org/10.1109/TCPMT.2019.2933792>. – DOI 10.1109/TCPMT.2019.2933792. – ISSN 2156–3950
- [OT16] Oesterreich, T. D.; Teuteberg, F.: Understanding the implications of digitisation and automation in the context of Industry 4.0: A triangulation approach and elements of a research agenda for the construction industry. In: *Computers in Industry* 83 (2016), 121–139. <http://dx.doi.org/https://doi.org/10.1016/j.compind.2016.09.006>. – DOI <https://doi.org/10.1016/j.compind.2016.09.006>. – ISSN 0166–3615
- [PKH20] Petrov, V.; Kurner, T.; Hosako, I.: IEEE 802.15.3d: First Standardization Efforts for Sub-Terahertz Band Communications toward 6G. In: *IEEE Communications Magazine* 58 (2020), Nr. 11, S. 28–33. <http://dx.doi.org/10.1109/MCOM.001.2000273>. – DOI 10.1109/MCOM.001.2000273
- [Poz12] Pozar, D. M.: *Microwave engineering*. 4. ed. Hoboken, NJ : Wiley, 2012 <http://swbplus.bsz-bw.de/bsz350987262cov.htm>. – ISBN 978–0–470–63155–3
- [PSB⁺24] Pfahler, T.; Scheder, A.; Bridier, A.; Schür, J.; Vossiek, M.: A Low-Loss Bond-Wire Interconnect Design With More Than

- 130 GHz Bandwidth Enabling an Ultra-Broadband Heterogeneous System Design. In: *IEEE Transactions on Microwave Theory and Techniques* 72 (2024), Nr. 1, S. 505–515. <http://dx.doi.org/10.1109/TMTT.2023.3314113>. – DOI 10.1109/TMTT.2023.3314113
- [PSC⁺19] Piekarz, I.; Sorocki, J.; Craton, M. T.; Wincza, K.; Gruszczynski, S.; Papapolymerou, J.: Application of Aerosol Jet 3-D Printing With Conductive and Nonconductive Inks for Manufacturing mm-Wave Circuits. In: *IEEE Transactions on Components, Packaging and Manufacturing Technology* 9 (2019), Nr. 3, S. 586–595. <http://dx.doi.org/10.1109/TCPMT.2018.2889698>. – DOI 10.1109/TCPMT.2018.2889698. – ISSN 2156–3950
- [RJB⁺18] Röhl, F. X.; Jakob, J.; Bogner, W.; Weigel, R.; Zorn, S.: *Bare Die Connections via Aerosol Jet Technology for Millimeter Wave Applications*. Piscataway, NJ : IEEE, 2018 <http://ieeexplore.ieee.org/servlet/opac?punumber=8528202>. – ISBN 9781538652855
- [RXK⁺19] Rappaport, T. S.; Xing, Y.; Kanhere, O.; Ju, S.; Madanayake, A.; Mandal, S.; Alkhateeb, A.; Trichopoulos, G. C.: Wireless Communications and Applications Above 100 GHz: Opportunities and Challenges for 6G and Beyond. In: *IEEE Access* 7 (2019), S. 78729–78757. <http://dx.doi.org/10.1109/ACCESS.2019.2921522>. – DOI 10.1109/ACCESS.2019.2921522
- [Ryd23] Rydning, J.: *Worldwide IDC Global Data Sphere Forecast 2023-2027: It's a Distributed Diverse and Dynamic (3D) DataSphere*. 04 2023
- [San21] Santos, J. L.: Optical Sensors for Industry 4.0. In: *IEEE Journal of Selected Topics in Quantum Electronics* 27 (2021), Nr. 6, S. 1–11. <http://dx.doi.org/10.1109/JSTQE.2021.3078126>. – DOI 10.1109/JSTQE.2021.3078126
- [SDC⁺21] Spain, W.; Darpinian, Z.; Crump, C.; Papapolymerou, J.; Chahal, P.; Albrecht, J. D.: Fully Aerosol Jet Printed Interconnects and Fill Materials for Millimeter Wave Circuits. In: *2021 IEEE International Conference on Microwaves, Antennas, Communications and Electronic Systems (COMCAS)*, 2021, S. 107–110

- [SDS⁺17] Sinha, S.; Doerner, R.; Schmueckle, F.-J.; Monayakul, S.; Hrobak, M.; Weimann, N. G.; Krozer, V.; Heinrich, W.: Flip-Chip Approach for 500 GHz Broadband Interconnects. In: *IEEE Transactions on Microwave Theory and Techniques* 65 (2017), Nr. 4, S. 1215–1225. <http://dx.doi.org/10.1109/TMTT.2016.2638429>. – DOI 10.1109/TMTT.2016.2638429
- [Sec18] Secor, E. B.: Principles of aerosol jet printing. In: *Flexible and Printed Electronics* 3 (2018), Nr. 3, S. 035002. <http://dx.doi.org/10.1088/2058-8585/aace28>. – DOI 10.1088/2058-8585/aace28. – ISSN 0894-0630
- [Son17] Song, H.-J.: Packages for Terahertz Electronics. In: *Proceedings of the IEEE* 105 (2017), Nr. 6, S. 1121–1138. <http://dx.doi.org/10.1109/JPROC.2016.2633547>. – DOI 10.1109/JPROC.2016.2633547
- [SSM] Soma, T.; Satoh, J.; Matsuo, H.: Thermal expansion coefficient of GaAs and InP. 42, Nr. 12, 889-892. [http://dx.doi.org/https://doi.org/10.1016/0038-1098\(82\)90233-2](http://dx.doi.org/https://doi.org/10.1016/0038-1098(82)90233-2). – DOI [https://doi.org/10.1016/0038-1098\(82\)90233-2](https://doi.org/10.1016/0038-1098(82)90233-2). – ISSN 0038-1098
- [ST07] Singh, K. B.; Tirumkudulu, M. S.: Cracking in drying colloidal films. In: *Physical review letters* 98 (2007), Nr. 21, S. 218302. <http://dx.doi.org/10.1103/PhysRevLett.98.218302>. – DOI 10.1103/PhysRevLett.98.218302. – ISSN 0031-9007
- [STH03] Schnieder, F.; Tischler, T.; Heinrich, W.: Modeling dispersion and radiation characteristics of conductor-backed CPW with finite ground width. In: *IEEE Transactions on Microwave Theory and Techniques* 51 (2003), Nr. 1, S. 137–143. <http://dx.doi.org/10.1109/TMTT.2002.806926>. – DOI 10.1109/TMTT.2002.806926
- [TL24] Thome, F.; Leuther, A.: Low-Noise Power-Amplifier MMICs for the WR4.3 and WR3.4 Bands in a 35-nm Gate-Length InGaAs mHEMT Technology. In: *IEEE Microwave and Wireless Technology Letters* 34 (2024), Nr. 6, S. 749–752. <http://dx.doi.org/10.1109/LMWT.2024.3388320>. – DOI 10.1109/LMWT.2024.3388320

- [TR05] Tirumkudulu, M. S.; Russel, W. B.: Cracking in drying latex films. In: *Langmuir : the ACS journal of surfaces and colloids* 21 (2005), Nr. 11, S. 4938–4948. <http://dx.doi.org/10.1021/la048298k>. – DOI 10.1021/la048298k. – ISSN 0743–7463
- [van08] van Oss, C. J.: Chapter Two - The Apolar and Polar Properties of Liquid Water and Other Condensed-Phase Materials. Version: 2008. [http://dx.doi.org/https://doi.org/10.1016/S1573-4285\(08\)00202-0](http://dx.doi.org/https://doi.org/10.1016/S1573-4285(08)00202-0). In: van Oss, C. J. (Hrsg.): *The Properties of Water and their Role in Colloidal and Biological Systems* Bd. 16. Elsevier, 2008. – DOI [https://doi.org/10.1016/S1573-4285\(08\)00202-0](https://doi.org/10.1016/S1573-4285(08)00202-0). – ISSN 1573–4285, 13-30
- [VD24] Virginia Diodes, I.: *VNA Extender - VDI Model: WR3.4-VNAX*. 2024. – <https://www.vadiodes.com/en/wr3-4vnax> [Accessed: (17.10.2024)]
- [WHM21] Waldschmidt, C.; Hasch, J.; Menzel, W.: Automotive Radar — From First Efforts to Future Systems. In: *IEEE Journal of Microwaves* 1 (2021), Nr. 1, S. 135–148. <http://dx.doi.org/10.1109/JMW.2020.3033616>. – DOI 10.1109/JMW.2020.3033616
- [WKF⁺21] Wiatrowska, A.; Kowalczewski, P.; Fiaczyk, K.; Witczak, L.; Gadzalinska, J.; Lysien, M.; Schneider, L.; Kosior, L.; Granek, F.: 59-3: Ultra-Precise Printing of Micrometer-Size Interconnectors for High-Resolution MicroLED Displays. In: *SID Symposium Digest of Technical Papers* 52 (2021), Nr. 1, 833-836. <http://dx.doi.org/https://doi.org/10.1002/sdtp.14812>. – DOI <https://doi.org/10.1002/sdtp.14812>
- [WMD91] Williams, D. F.; Marks, R. B.; Davidson, A.: Comparison of On-Wafer Calibrations. In: *38th ARFTG Conference Digest*, IEEE, 05.12.1991 - 06.12.1991. – ISBN 0-7803-5686-1, S. 68–81
- [WSKH19] Wilkinson, N. J.; Smith, M. A. A.; Kay, R. W.; Harris, R. A.: A review of aerosol jet printing—a non-traditional hybrid process for micro-manufacturing. In: *The International Journal of Advanced Manufacturing Technology* 105 (2019), Nr. 11, S. 4599–4619. <http://dx.doi.org/10.1007/s00170-019-03438-2>. – DOI 10.1007/s00170-019-03438-2. – ISSN 0268–3768

- [ZH06] Zhang, J.; Hsiang, T.: Dispersion Characteristics of Coplanar Waveguides at Subterahertz Frequencies. In: *Piers Online* 2 (2006), 01, S. 232–235. <http://dx.doi.org/10.2529/PIERS051104233126>. – DOI 10.2529/PIERS051104233126

Own Publications

Journal Papers

- [1] Bekker, E.; **Gramlich, G.**; Valenziano, L.; Oliveira, L. G.; Antes, T.; Zwick, T.; Bhutani, A.: Broadband packaging solution in embedded wafer level ball grid array technology for D-band PMCW radar. In: *International Journal of Microwave and Wireless Technologies* (2024), S. 1–12. <http://dx.doi.org/10.1017/S1759078724000266>. – DOI 10.1017/S1759078724000266
- [2] Boes, F.; **Gramlich, G.**; Kretschmann, M.; Marahrens, S.; Zwick, T.: Ultrabroadband Diplexers for Next-Generation High-Frequency Measurement Applications. In: *IEEE Transactions on Microwave Theory and Techniques* 68 (2020), Nr. 6, S. 2161–2167. <http://dx.doi.org/10.1109/TMTT.2020.2977289>. – DOI 10.1109/TMTT.2020.2977289
- [3] Mescher, H.; Schackmar, F.; Huber, R.; Eggers, H.; Zuber, M.; Hamann, E.; **Gramlich, G.**; Dangelmaier, J.; Zhang, Q.; Roesch, A. G.; Zwick, T.; Hernandez-Sosa, G.; Paetzold, U. W.; Lemmer, U.: Origami-inspired perovskite X-ray detector by printing and folding. In: *npj Flexible Electronics* 7 (2023), feb, Nr. 9. <http://dx.doi.org/10.1038/s41528-023-00240-9>. – DOI 10.1038/s41528-023-00240-9
- [4] **Gramlich, G.**; Bekker, E.; Valenziano, L.; Dittmer, J.; Roemhild, M.; Baur, H.; Thome, F.; Tessmann, A.; Kuri, M.; Neerfeld, T.; Stöhr, A.; Randel, S.; Koos, C.; Fruehauf, N.; Zwick, T.; Bhutani, A.: Hybrid Integration of a Beam-Steering Leaky-Wave Antenna and Power Amplifier MMIC Using UPD Printing in 220 to 325 GHz Range. In: *IEEE Open Journal of Antennas and Propagation* 6 (2025), Nr. 3, S. 837–853. <http://dx.doi.org/10.1109/OJAP.2025.3551350>. – DOI 10.1109/OJAP.2025.3551350. – This work is licensed under the Creative Commons Attribution 4.0 International License. To view a copy of this license, visit <http://creativecommons.org/licenses/by/4.0/>.

- [5] **Gramlich, G.**; Huber, R.; Haeslich, F.; Bhutani, A.; Lemmer, U.; Zwick, T.: Process considerations for Aerosol-Jet printing of ultra fine features. In: *Flexible and Printed Electronics* 8 (2023), jul, Nr. 3, 035002. <http://dx.doi.org/10.1088/2058-8585/ace3d8>. – DOI 10.1088/2058-8585/ace3d8. – This work is licensed under the Creative Commons Attribution 4.0 International License. To view a copy of this license, visit <http://creativecommons.org/licenses/by/4.0/>.
- [6] **Gramlich, G.**; Roemhild, M.; Wendel, J.; Weiss, L.; Baur, H.; Lemmer, U.; Fruehauf, N.; Zwick, T.; Bhutani, A.: Semi-automatic conformal micro-scale printing with the ultra-precise dispensing (UPD) system. In: *Flexible and Printed Electronics* 10 (2025), sep, Nr. 3, 035015. <http://dx.doi.org/10.1088/2058-8585/ae004b>. – DOI 10.1088/2058-8585/ae004b. – This work is licensed under the Creative Commons Attribution 4.0 International License. To view a copy of this license, visit <http://creativecommons.org/licenses/by/4.0/>.
- [7] Valenziano, L.; Hebel, J.; **Gramlich, G.**; Quint, A.; Zwick, T.; Bhutani, A.: Advanced Bond-Wire Interconnect Solution for Ultra-Broadband Applications Covering DC to 210 GHz. In: *IEEE Transactions on Components, Packaging and Manufacturing Technology* (2024), S. 1–1. <http://dx.doi.org/10.1109/TCPMT.2024.3465608>. – DOI 10.1109/TCPMT.2024.3465608
- [8] Valenziano, L.; **Gramlich, G.**; Quint, A.; Zwick, T.; Bhutani, A.: Ultrabroadband DC-Blocking Capacitors Using 3-D-Printed Interdigitated Finger Structures. In: *IEEE Transactions on Microwave Theory and Techniques* 73 (2025), Nr. 9, S. 6010–6016. <http://dx.doi.org/10.1109/TMTT.2025.3541853>. – DOI 10.1109/TMTT.2025.3541853

Conference Papers

- [9] Bekker, E.; Quint, A.; **Gramlich, G.**; Valenziano, L.; Zwick, T.; Bhutani, A.: 110 to 170 GHz High-Gain Antenna with Embedded Surface Mount Short Horn and Baseband PCB Horn Antenna. In: *2024 18th European Conference on Antennas and Propagation (EuCAP)*, 2024, S. 01–05
- [10] Bekker, E.; **Gramlich, G.**; Oliveira, L. G.; Bhutani, A.; Zwick, T.: Wideband, High Gain Dielectric Resonator Antenna in Embedded Surface

- Mount Short Horn in D-band. In: *2023 53rd European Microwave Conference (EuMC)*, 2023, S. 86–89
- [11] Bekker, E.; **Gramlich, G.**; Quint, A.; Valenziano, L.; Oliveira, L. G.; Bhutani, A.; Zwick, T.: Broadband, Via-less Grounded Coplanar Waveguide-to-Microstrip Transition in D-band. In: *2023 53rd European Microwave Conference (EuMC)*, 2023, S. 114–117
- [12] Boes, F.; Weißer, J.; Kretschmann, M.; **Gramlich, G.**; Marahrens, S.; Zwick, T.: Design and Tolerance Analysis of Cascaded Broadband Contiguous Microwave Diplexers. In: *2020 German Microwave Conference (GeMiC)*, 2020, S. 168–171
- [13] Roemhild, M.; **Gramlich, G.**; Baur, H.; Zwick, T.; Fruehauf, N.: Ultraprecise Printing of D-Band Transmission Lines. In: *IEEE Microwave and Wireless Technology Letters* 33 (2023), Nr. 10, S. 1419–1422. <http://dx.doi.org/10.1109/LMWT.2023.3300569>. – DOI 10.1109/LMWT.2023.3300569
- [14] Roemhild, M.; **Gramlich, G.**; Wendel, J.; Baur, H.; Zwick, T.; Fruehauf, N.: Ultraprecise Printing of D-Band Interconnects Using Dielectric Ramps. In: *2024 15th German Microwave Conference (GeMiC)*, 2024, S. 57–60
- [15] **Gramlich, G.**; Hebel, J.; Bohn, C.; Lemmer, U.; Zwick, T.: Aerosol Jet Printed Microstrip Lines on Polyimide for D-Band. In: *2021 51st European Microwave Conference (EuMC)*, 2022, S. 551–554. – © 2021 European Microwave Association, EuMA
- [16] **Gramlich, G.**; Huber, R.; Lemmer, U.; Zwick, T.: Aerosol Jet Printed Millimeter Wave Interconnects in D-Band. In: *2022 52nd European Microwave Conference (EuMC)*, 2022, S. 298–301. – © 2022 European Microwave Association, EuMA
- [17] **Gramlich, G.**; Lemmer, U.; Zwick, T.; Bhutani, A.: Aerosol-Jet-Printed Ramp-Based Interconnects from DC to D-Band. In: *2025 16th German Microwave Conference (GeMiC)*, 2025, S. 21–24
- [18] **Gramlich, G.**; Römhild, M.; Baur, H.; Bhutani, A.; Lemmer, U.; Fruehauf, N.; Zwick, T.: Ultra-Precise Deposition (UPD) Printing for Millimeter Wave Interconnects in D-Band. In: *2023 Asia-Pacific Microwave Conference (APMC)*, 2023, S. 1–3. – © 2023 IEEE. Reprinted, with permission, from Gramlich, Georg and Römhild, Martin and Baur, Holger and Bhutani, Akanksha and Lemmer, Uli and Fruehauf,

- Norbert and Zwick, Thomas, Ultra-Precise Deposition (UPD) Printing for Millimeter Wave Interconnects in D-Band, 12/2023
- [19] **Gramlich, G.**; Speder, K.; Roernhild, M.; Baur, H.; Fruehauf, N.; Zwick, T.; Bhutani, A.: Dielectric Characterization of Adhesives for THz Packaging in WR6.5, WR3.4 and WR2.2 Bands. In: *2024 18th European Conference on Antennas and Propagation (EuCAP)*, 2024, S. 1–5
 - [20] **Gramlich, G.**; Weiss, L.; Valenziano, L.; Roemhild, M.; Baur, H.; Schwarzenberger, A.; Eschenbaum, C.; Koos, C.; Fruehauf, N.; Zwick, T.; Bhutani, A.: An Ultra-Precise Dispensing (UPD) Printed, Ultra-Broadband PCB to MMIC Interconnect. In: *2025 IEEE Radio and Wireless Symposium (RWS)*, 2025, S. 81–84. – © 2025 IEEE. Reprinted, with permission, from Gramlich, Georg and Weiss, Lilli and Valenziano, Luca and Roemhild, Martin and Baur, Holger and Schwarzenberger, Adrian and Eschenbaum, Carsten and Koos, Christian and Fruehauf, Norbert and Zwick, Thomas and Bhutani, Akanksha, An Ultra-Precise Dispensing (UPD) Printed, Ultra-Broadband PCB to MMIC Interconnect, 01.2025
 - [21] Valenziano, L.; Bekker, E.; **Gramlich, Georg**; Zwick, T.; Bhutani, A.: UPD Printed 140 GHz Split Ring Resonator Antenna for Device-to-Device Communication. In: *2025 16th German Microwave Conference (GeMiC)*, 2025, S. 92–95
 - [22] Valenziano, L.; **Gramlich, G.**; Quint, A.; Zwick, T.; Bhutani, A.: 3D Printing of Interdigitated Finger Capacitors Using Ultra-Precise Deposition Technology. In: *2024 25th International Microwave and Radar Conference (MIKON)*, 2024, S. 26–30
 - [23] Valenziano, L.; Zeh, F.; **Gramlich, G.**; Zwick, T.; Bhutani, A.: Ultra-Precise Deposition – XTPL Technology for 3D Printed Broadband Spiral Inductors. In: *2024 15th German Microwave Conference (GeMiC)*, 2024, S. 53–56